Vortex Wakes and the Mechanics of Membrane Wings—Problems Inspired by Bat Flight

by

Rye M. Waldman

B.S., University Illinois Urbana-Champaign, 2007

Dissertation

Submitted in partial fulfillment of the requirements for the degree of Doctor of Philosophy in the School of Engineering at Brown University

PROVIDENCE, RHODE ISLAND

MAY 2014

AUTHORIZATION TO LEND AND REPRODUCE THE THESIS

As the sole author of this thesis, I authorize Brown University to lend it to other institutions or individuals for the purpose of scholarly research.

Date: _____ _____

Rye M. Waldman

I further authorize Brown University to reproduce this thesis by photocopying or other means, in total or in part, at the request of other institutions or individuals for the purpose of scholarly research.

Date: _____ _____

Rye M. Waldman

This dissertation by Rye M. Waldman is accepted in its present form by the School of Engineering as satisfying the dissertation requirement for the degree of Doctor of Philosophy.

Date: _____ _____

Dr. Kenneth S. Breuer, Advisor

Recommended to the Graduate Council

Date: _____ _____

Dr. Shreyas Mandre, Reader

Date: _____ _____

Dr. Sharon M. Swartz, Reader

Approved by the Graduate Council

Date: _____ _____

Dr. Peter M. Weber, Dean of the Graduate School

Abstract

Abstract of "Vortex Wakes and the Mechanics of Membrane Wings—Problems Inspired by Bat Flight," by Rye M. Waldman, Ph.D., Brown University, May 2014

We present experimental investigations on two classes of problems that are inspired by bat flight—vortex wakes and compliant membrane wings. Aerodynamic experiments with flapping animals (such as bats and small birds) receive considerable attention because the unique approaches to low Reynolds number flight ($Re < 200,000$) that animals employ may offer clues to engineers designing small autonomous aircraft that operate under similar flight conditions. Previous particle image velocimetry (PIV) measurements of bat and bird wakes have revealed complex vortex structures; however, these studies have struggled to draw quantitative conclusions about the aerodynamic forces generated in flight. Necessary compromises in the experimental designs may lead to unsatisfactory dynamic range in the velocity measurements, which in turn lead to reduced accuracy of the results. We performed a detailed analysis of PIV wake measurements, determined the criteria for making accurate measurements, and implemented a dual-plane PIV technique that satisfies these criteria and improves the dynamic range of wind tunnel wake measurements. The increased dynamic range of dual-plane PIV permits accurate aerodynamic force predictions from PIV measurements in the wake of Seba's short-tailed bats (*Carollia perspicillata*) and allows the direct calculation of the aerodynamic cost of flight from the kinetic energy observed in the wake.

One of the interesting features of bat morphology that allows bats extraordinary flight capabilities is their membraneous wing skin—a feature that is unique among extant flying animals. With compliant membrane wings that are initially tension-free at rest, there are two issues to consider: (a) the static relationship between the net aerodynamic forces and the bulk wing deformation, and (b) the interaction between the membrane dynamics and unsteady flow structures. We developed a simple model

of the finite deformation and natural frequency of an initially tension-free membrane wing, which depends only on an aeroelastic parameter and shows good agreement with experiments on low aspect ratio membrane wings with different support structures and thicknesses, over a broad range of flight parameters. Coupled membrane shape, aerodynamic force, and PIV wake measurements indicate that membrane deformation affects the membrane vibration modes, which in turn affects the coupling between the membrane and vortex shedding. Wings with different wing tip support but similar stiffness show similar static behavior but exhibit markedly different dynamic behavior. Low wing aspect ratio is a common feature utilized by biological fliers, where the influence of wing tip vortices affect the flow over the entire wingspan; however, membrane wings may strongly interact with and affect the vortices at the wing tips. The details of the membrane support play an important role in the fluid-structure interaction. Our experiments show that freely fluttering wing tips disrupt the structure of the tip vortices, leading to a diffuse, erratic vortex structure and reduced aerodynamic performance at high angle of attack compared to the tip vortices formed on rigidly supported membrane wings.

Curriculum Vitæ

Rye M. Waldman was born in Birmingham, Alabama, on February 23, 1985, and lived in Aurora, Illinois, until he graduated from Waubonsie Valley High School in 2003. He attended the University of Illinois at Urbana-Champaign, where he graduated with a B.S. in Engineering Mechanics in 2007. While in Champaign, he worked for Caterpillar, Inc. as a student stress analyst at the Champaign Simulation Center. He joined the Fluid, Thermal, and Chemical Processes group in the School of Engineering at Brown University in Providence, Rhode Island to work towards a Doctor of Philosophy in Engineering under the guidance of Dr. Kenneth S. Breuer. There, Mr. Waldman developed experimental techniques and investigated problems related to the aerodynamics of membrane wings, inspired by bat flight.

Acknowledgments

I am very fortunate to have been surrounded by many excellent people throughout the course of my graduate studies, without whom none of this work would have been possible.

First and foremost, I would like to thank my advisor, Professor Kenneth S. Breuer, whose mentorship has allowed me to grow as a researcher. His encouragement and guidance have helped me develop my skills as an experimentalist, scientific writer, public speaker, and professional. I have certainly had an easier time learning some skills rather than others, and, therefore, I am deeply indebted to the patience and persistence that Professor Breuer has afforded me during my times of challenge. In the end, he has taught me to think critically about my experiments and results, to keep the big-picture questions in sight, and to have an oscilloscope with me, *always*!

The close collaboration of the Breuer and Swartz labs formed my "academic family," so I am also deeply indebted to Professor Sharon M. Swartz, who introduced me to the world of bats and bat flight, who played an important role in the formulation of my research questions, and who provided valuable feedback and insight on this thesis.

I would also like to thank Professor Shreyas Mandre for reading this thesis and providing valuable suggestions. I am grateful for the discussions I have had with Professor Mandre, and for the times I have spent with him in his lab—every time, I learned something new from his scientific insight and experimental experience.

The staff at Brown University has helped me significantly during the course of my study and research. I would especially like to recognize Brian Corkum, Jeff Brown, Erika Giblin, Benjamin Lyons, Charles Vickers, and Chantee Weah.

I have had the privilege to work with many talented researchers during my time at Brown University. The discussions, help, and long hours spent inside and outside of the lab with these individuals have had a hugely positive impact on my research

and my life in Providence: Dr. Tatjana Hubel, Dr. Dan Riskin, Dr. Arnold Song, Dr. Charles Peguero, Dr. Joseph Bahlman, Jorn Cheney, Shawn Kitchner, Cosima Schunk, Rick He, John DiBenedetto, David Gagnon, Alex Carrere, Ian Brownstein, Ben Strom, Marco Gulino, Dr. Attila Bergou, Dr. Tony Yu, Dr. Bin Liu, Dr. Jennifer Franck, Dr. Nicolai Konow, and Professor Oscar Curet. I need to give a special thanks to Arnold and Jorn, who have played a critical role helping me keep my sanity throughout my time at Brown.

My housemates from Benefit St. have contributed a great deal to the success of my research. They are an incredible—and incredibly smart—group of friends whose conversations varied from technical discussions on "Determining the onset of dislocation creep from the energy landscape using numerical schemes" to "An analogy of microprocessor architecture using cats" to "The plausibility of Bier as a lasing medium" to "Bacon." They were always there to help (or to distract) me when I needed it: Scott Hoffmann, Dr. Gerard Paul-Leyson, Dr. Sean Teller, Dr. Elizabeth Normand, Bradley Campbell, and the furry critters Brini*, Ralphie, Zeva, and Neil.

My undergraduate study in the department of Theoretical and Applied Mechanics* at the University of Illinois provided a solid academic foundation for my research career, and I consider myself incredibly fortunate to have had the opportunity be a part of the close-knit mechanics community. I received wonderful training and advice from Professor James W. Phillips, Professor Richard L. Weaver, Professor Nancy R. Sotos, Professor Gustavo Gioia, Professor Pinaki Chakraborty, and Dr. Richard D. Keane.

I must thank my family for their continued love, support, and patience. My father sparked my interest in math, physics, and engineering through his own enthusiasm for structural design and engineering fundamentals; he opened my eyes to the wonders of physical phenomena. My mother taught me to use a semicolon correctly (which, I am fairly certain, is somehow sufficient to prove the Goldbach conjecture). In all seriousness, however, I owe the entirety of my ability to form words into sentences

to her lifelong writing tutorship, and if I had half of the writing prowess that she has, I would have finished this thesis years ago. During the time it has taken me to complete this thesis, Cassy and Trey have both grown into two fine young adults, and I am very thankful that they have supported me throughout this process, despite how infrequently I have visited home. A 'thank you' goes to Dewey and Truman for being very furry and scratchable.

Most of all, I must thank my amazing fiancée, Rhea, who has been my source of hope and strength. Only with her love and support was this work possible. Thank you!

For my mother, Lynn, and my father, Mark.

Table of Contents

List of Tables

List of Figures

CHAPTER 1. Introduction

The myth of Icarus and Daedalus exemplifies how mankind's fascination with animal flight dates as far back as the ancient Greeks, yet only in the past century have we developed the capability of sustained flight. Furthermore, despite the millennia of inspiration from animal flight, the engines that power man-made flying craft are rotating motors, which is in contrast to the linear actuation of the muscles that power flapping wings for all biological fliers.

Passenger aircraft were the original focus of the pioneering aircraft designs, and since the Wright brothers' first flight, advances in technology and aerodynamic theory have led to mature aircraft designs with lighter airframes, more efficient propulsion, and superior aerodynamics. More recent advances in technology now allow small and lightweight electronics, smart materials, and miniature sensors, which make possible the design of small autonomous aircraft. Of particular interest are Micro Air Vehicles (MAVs), which are small and maneuverable aircraft with wingspans less than 15 cm and flying below 20 m/s [1]. At these small length and speed scales, the potential-flow-based design principles that have been developed for large aircraft begin to break down, and the details of viscous phenomena like flow separation, the transition to turbulence, and reattachment become of increasing importance as Reynolds numbers descend to the order of 10^5 [2]. Despite these challenges, small maneuverable fliers

Figure 1.1: *Pteropus vampyrus* is a large fruit bat. The folded wing is very compact yet can extend out for flight thanks to an articulated wing skeleton and a highly compliant skin membrane. Chordwise muscles embedded in the wing skin—plagiopatagiales—can be seen in the outstretched wing. (Photo courtesy of Jorn Cheney)

offer many potential benefits for applications where direct human access would be impossible, inconvenient, or hazardous. Such missions might include search-and-rescue missions in complex environments, routine maintenance inspections in dangerous environments, or military surveillance.

Nature has addressed the challenges of low Reynolds number flight ($Re < 200,000$) over millions of years of evolution. Three extant animal groups—insects, birds, and bats—have independently evolved the ability for self-sustained flight. Among them are specialists with the efficiency to migrate thousands of miles, hawkers with the agility to catch prey on the wing, and nectar feeders with the ability to hover. Furthermore, the different taxa accomplish these varied performance criteria with different morphologies: insect wings are hinged, thin cuticle plates; bird wings are feathered, jointed arms; and bats wings are composed of a highly compliant membraneous skin supported by highly articulated forelimbs and hindlimbs [3]. Bat wing morphology is the most complex, and their many-jointed wings offer the greatest potential for actuation and flight control. Additionally, bat wing skin also features embedded muscles, which may allow for additional control of the wing membrane (Fig. 1.1).

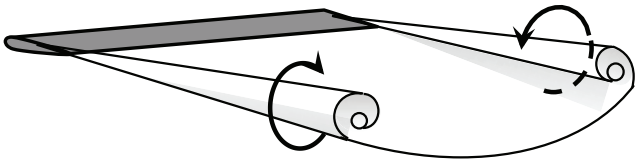

Figure 1.2: Finite-span lifting wings form tip vortices at the wing tips. Traditional lifting-line theory envisions a vortex sheet emanating from the wing, which is simplified as a bound vortex—the "lifting line"—located at quarter-chord, whose local strength is proportional to the local spanwise change in strength of the bound vortex. This vortex sheet rolls up around each end of the vortex sheet into the two characteristic tip vortices.

Like the ancient Greeks, we derive inspiration from fliers in the natural world. The work in this dissertation is inspired by problems related to bat flight, and the topics addressed herein are two-fold: namely, (a) the development and application of experimental techniques for the accurate measurement of the vortex wakes behind low speed fliers, and (b) theoretical and experimental investigations of the aeromechanics of highly compliant membrane wings.

1.1 Wind Tunnel Measurements of Small Fliers

Vertebrate fliers cannot be directly tethered to a force balance for aerodynamic load testing, for reasons including animal safety and behavioral tolerance. Thus, the aerodynamic forces must be inferred indirectly from wake measurements. The principles for studying the aerodynamic forces on both free-flying animals and engineering models in wind tunnels are based on Kutta-Joukowski lift and finite-span aerodynamics. The classic Kutta-Joukowski formula for the lift on a wing section is

$$l = \rho U_\infty \Gamma, \tag{1.1}$$

where l is the lift per unit span, ρ is the density of air, U_∞ is the forward flight speed (or conversely, the freestream velocity if the frame of reference is fixed on the flier), and Γ is the bound circulation. For real fliers (as opposed to the hypothetical,

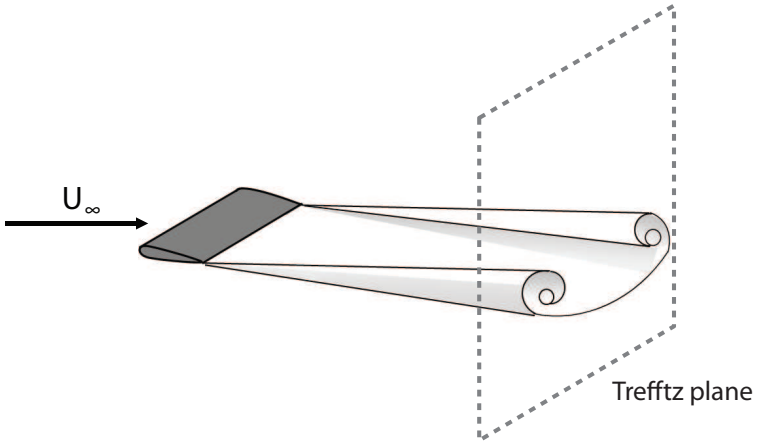

Figure 1.3: The Trefftz plane intersecting the wake behind a lifting wing.

two-dimensional fliers often studied in textbooks), the finite extent of the span will introduce three-dimensional effects (Fig. 1.2). By application of Helmholtz's vortex theorems [4], the vortex lines in a flow cannot terminate within the fluid; rather, they must either form closed loops or terminate at a solid boundary. In the case of steady, level flight, the complete vortex system on a finite wing consists of the wing-bound vortex connected to an initial starting vortex created at the onset of flight by the wing tip trailing vortices. When the flier has reached steady-state flight, it is common to assume that the starting vortex is infinitely far away and to picture a vortex system consisting of the bound vorticity and two trailing vortices extending to $-\infty$. Because the vortex lines from the bound circulation extend to $-\infty$ via each of the trailing vortices, the wing circulation can be determined by measuring the circulation of the trailing vortex in the flow-transverse plane behind the flier, i.e., the Trefftz plane (Fig. 1.3).

In reality, the vortex systems of real wings are not quite as simple: the wing-bound circulation varies with spanwise position, and as the strength of the wing-bound circulation changes, vortex lines are shed into the wake, and the result is a vortex system that is the superposition of many closed vortex loops. The total lift

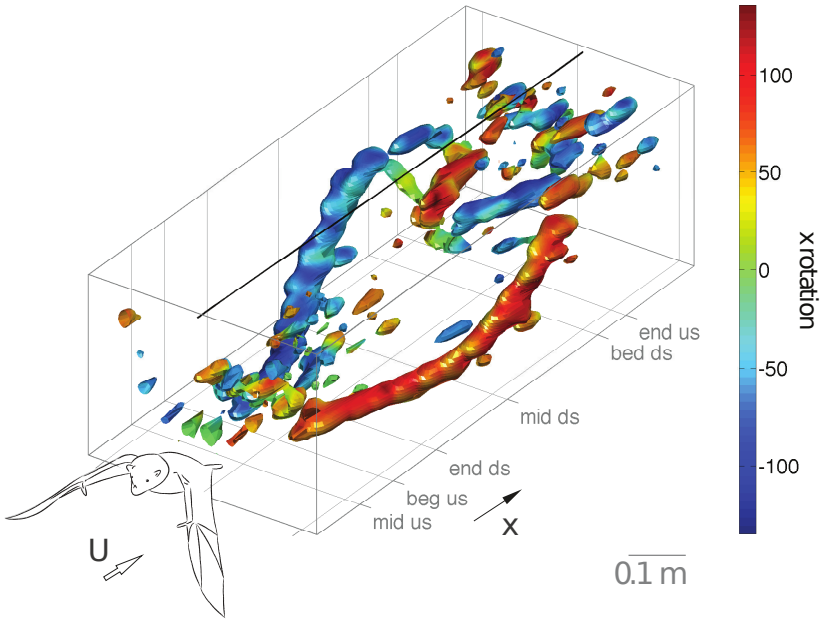

Figure 1.4: The wake structures behind a bat.

requires integrating the sectional lift coefficient over the span of the wing,

$$L = \int_{\text{span}} \rho U_\infty \Gamma(y) \mathrm{d}y, \tag{1.2}$$

where L is the total lift. The lift distribution on the wing is related to the distribution of vorticity in the wake [5]. Furthermore, the changing geometry of flapping fliers leads to complex vortex wake topologies. Fig. 1.4 shows the wake structures behind a flying bat: a network of vortex rings. This wake represents the aerodynamic footprint of the flier and contains information regarding the time-space distribution of the aerodynamic force production.

Multiple studies have been performed on various insect, avian, and mammalian fliers and have illustrated inter- and intraspecific differences in wake structures [e.g., 6–17]. Fig. 1.5 shows the typical configuration of an animal flight Trefftz plane PIV measurement. These measurements push the limits of the capabilities of the PIV systems, and some limitations in resolving the quantitative strength of the vortex systems have been recognized. Several authors [11, 12, 15] have noted that their

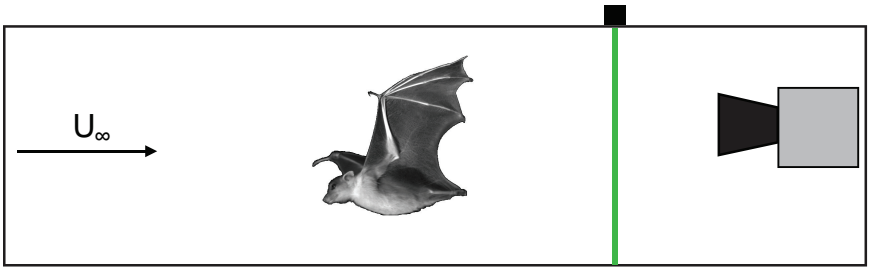

Figure 1.5: The typical configuration of an animal flight PIV measurement.

quantitative analyses of the strength of the measured vortex structures fail to explain weight support of the free-flying animals. Thus, improving the quantitative measurement accuracy of the PIV techniques used for measuring the wake structures typical of animal flight experiments is essential.

Like aerodynamic force, the power expenditure of free-flying animals is difficult to measure because of various obstacles in instrumenting the animal. However, understanding the energy cost of flight is important, both in an ecological context and for the design of flying vehicles. The majority of literature on aerodynamic cost of flight depends on simple models derived from traditional fixed-wing aerodynamic principles [e.g., 18, 19]. The only previous attempt to directly measure the aerodynamic power expenditure of a free-flying animal was conducted using helium bubble tracking by Spedding et al. [20]. Current state-of-the-art PIV measurement techniques present the opportunity for improved accuracy in the direct measurement of the aerodynamic power cost of flight.

1.2 Compliant Wings

Traditionally, aeroelasticity has a negative connotation with respect to aircraft because the elastic deformation of lifting structures can lead to divergent deformations or cause the aerodynamic response of control surfaces to deviate from the design performance. Furthermore, aeroelastic instabilities can lead to dangerous and unexpected limit cycle oscillations that cause catastrophic mechanical failures. However,

in contrast to the rigid wing designs of traditional man-made aircraft, wing flexibility is a common feature throughout biological flier morphologies. Insect wings can be modeled as flexible plates subject to bending and torsion that allow passive wing pitching [21], bird feathers can passively deform and may serve as flow control mechanisms [22], and bats feature highly compliant wing skin supported by a flexible wing skeleton [3, 23].

Bats are particulary interesting because of their unique wing morphology. Their highly compliant skin membrane and wing skeleton permit highly complex wing motion and control over many wing-shape degrees of freedom [24]. With their wings, bats exhibit extraordinary flight capabilities with the agility to reverse flight direction in a few wingbeats, hover in place, and flip upside-down with a single wing motion to land on the ceiling. To separate the contribution that the wing membrane has on the overall flight performance of bats, previous studies have examined membrane wing models, both computationally [25–29], and experimentally [26, 30–36]. Membrane wings exhibit aerodynamically advantageous features such as self-cambering, soft stall, and enhanced performance at large angles of incidence, and the membrane dynamics may interact with the flow and delay separation. Fig. 1.6 shows a model membrane wing in a wind tunnel experiment in an unloaded and a loaded state. The unloaded wing has a planar rectangular planform (Fig. 1.6a); however, after the wind tunnel is turned on (Fig. 1.6b), the wing adopts a cambered mean line and exhibits fluttering motion about its mean shape. Despite the growing body of experimental and computational work on membrane wings, a simple, self-contained theoretical description that can make a priori predictions of a membrane wing's response to a given set of aerodynamic conditions is missing from the literature. Furthermore, it is unclear how the membrane interacts with the flow to select the mode of membrane vibration.

Because membranes are thin, deformable structures with zero bending rigidity,

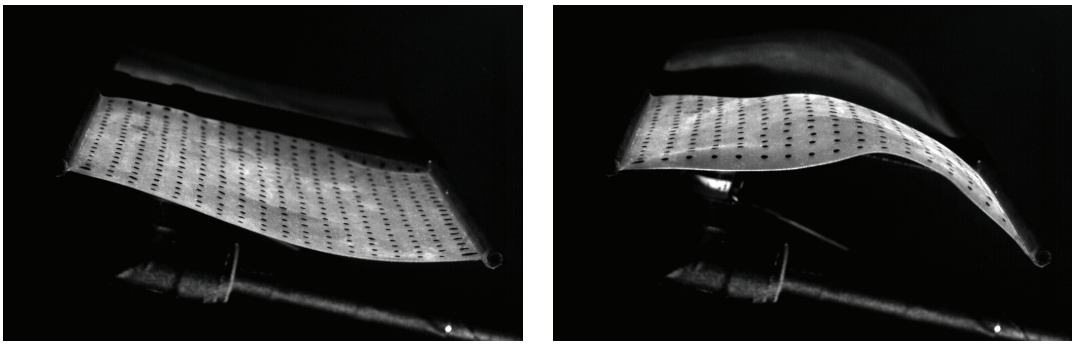

(a) Wind off **(b)** Wind on

Figure 1.6: A membrane wing mounted in a wind tunnel before (Fig. 1.6a) and after (Fig. 1.6b) aerodynamic loading.

they require support structures to maintain a force-bearing wing shape, and the detail of the support structure distribution is a critical component in determining the overall stiffness of the membrane wings. Throughout the studies in the literature, various membrane wing planforms and membrane support have been investigated, with wing geometries varying from two-dimensional membranes with supported leading and trailing edges [25, 27, 28, 32, 33], two-dimensional membranes with flexible leading- and trailing-edges [35], finite aspect ratio wings with distributed chordwise battens and unsupported trailing edges [26, 31, 36], finite aspect ratio wings with supported wing tips [29, 34], and finite aspect ratio wings with unsupported wing tips [30]. In addition to the structural importance of the wing shape and support distribution to the mechanical characteristics of the membrane wings, the wing planform design has direct impact on the nature of the aerodynamic flow. Finite span wings will experience the influence of a tip vortex at the ends of the wing, and the relative importance of this three-dimensional flow feature will become of increasing importance as the aspect ratio of the wings becomes small.

Although tip vortices are often associated with induced drag in traditional aerodynamic design, low aspect ratio wings may interact favorably with the tip vortices to suppress stall and enhance lift at high angles of attack [37, 38]. In fact, delta wings are designed specifically to form strong vortices from the leading edge that have low

pressure centers above the wing surface that contribute vortex lift [39]. Vortex breakdown over the wing can lead to the loss of vortex lift and increased flow unsteadiness. Biological fliers and MAVs can take advantage of both wing flexibility and low aspect ratio; however, wing configurations with both low aspect ratio and wing flexibility have received limited attention in the literature [26, 29, 30], and more work is needed to understand the general interaction of low aspect ratio phenomena and compliant wing mechanics.

1.3 Outline of Dissertation

The focus of this dissertation is on two topics related to bat flight: (a) wind tunnel measurements of vortex wakes, and (b) membrane wing mechanics. An experimental technique for accurate measurement of vortex wakes is developed and applied to wake measurements of bat flight in Chapters 2 and 3. Chapters 4 and 5 contain experimental, theoretical, and computational investigations of the fluid-structure interactions of compliant membrane wings. The content and relevant contributions are as follows:

Chapter 1. Introduction. An introduction to low Reynolds number flight, the application of wind tunnel experiments, and the importance of wing compliance in both man-made and biological fliers.

Chapter 2. "Accurate measurement of streamwise vortices using dual-plane PIV" by Rye M. Waldman and Kenneth S. Breuer. *Experiments in Fluids*, Vol. 53, pp. 1487–1500, 2012. This study was performed in response to a growing trend in the animal flight literature, where PIV wake studies failed to quantitatively explain the weight support of free-flying animals in wind tunnels. The dynamic range of the measurement is limited by the configuration of the experiments. We implemented a dual-plane technique for improved measurement dynamic range that allows high-accuracy measurements of streamwise vorticity. The experiments were conceived and summarized by R. M. Waldman and K. S. Breuer. The execution of the experiments and the analysis of the data was performed by R. M. Waldman.

Chapter 3. "The aerodynamic cost of flight in bats—comparing theory with measurement" by Rhea von Busse, Rye M. Waldman, Sharon M. Swartz, Christian C. Voigt, and Kenneth S. Breuer. *Journal of the Royal Society Interface*, in review, 2013. The preexisting studies of flapping flight energetics rely primarily on measurements of indirect metrics (such as metabolism) or on aerodynamic theories derived from fixed wing aircraft. Direct measurements of aerodynamic power require accurate

realizations of the structure and strength of the wake vorticity. We used dual-plane PIV to make the first direct measurement of the aerodynamic power cost of flight in bats using PIV, and we compared the results with metabolic measurements from the same individuals and with the aerodynamic theories. R. von Busse, R. M. Waldman, S. M. Swartz, C. C. Voigt, and K. S. Breuer conceived the experiments; R. von Busse performed the experiments; R. M. Waldman and R. von Busse analyzed the data; and the results were summarized by R. von Busse, R. M. Waldman, S. M. Swartz, and K. S. Breuer. R. M. Waldman was responsible for implementing the dual-plane PIV measurement system and developed the data analyis methods.

Chapter 4. "Shape, lift, and vibrations of highly compliant membrane wings" by Rye M. Waldman and Kenneth S. Breuer. In *43rd AIAA Fluid Dynamics Conference*, 2013. Bats feature highly compliant membrane wings supported by a highly articulated skeletal structure. The mechanics of the membrane wings depends on both the membrane properties and the details of the supporting structure. We developed a simple theory for a priori predictions of membrane wing behavior, and compare theory with calculations and wind tunnel experiments. The theoretical analysis, execution of the experiments, and data analysis was performed by R. M. Waldman. Experiments and simulations were conceived and summarized by R. M. Waldman and K. S. Breuer.

Chapter 5. "Vortex-Wing Interactions on Low Aspect Ratio Membrane Wings" by Rye M. Waldman and Kenneth S. Breuer. In preparation. Low aspect ratio membrane wings interact with vortices from the leading and trailing edges and wing tips. We examine the wing dynamics and the wake structure of low aspect ratio membrane wings with different wing tip support. The support structure of the wing can have an important impact on the aerodynamic performance of the wing. The execution of the experiments and the analysis of the data was performed by R. M. Waldman. Experiments were conceived and summarized by R. M. Waldman and

K. S. Breuer.

Chapter 6. Conclusion. Concluding remarks on low Reynolds number flight, wind tunnel experiments, and membrane wings, and recommendations for future work.

CHAPTER 2. Accurate Measurement of Streamwise Vortices Using Dual-Plane PIV

Abstract *Low Reynolds number aerodynamic experiments with flapping animals (such as bats and small birds) are of particular interest due to their application to micro air vehicles (MAVs) which operate in a similar parameter space. Previous PIV wake measurements described the structures left by bats and birds and provided insight to the time history of their aerodynamic force generation; however, these studies have faced difficulty drawing quantitative conclusions based on said measurements. The highly three-dimensional and unsteady nature of the flows associated with flapping flight are major challenges for accurate measurements. The challenge of animal flight measurements is finding small flow features in a large field of view at high speed with limited laser energy and camera resolution. Cross-stream measurement is further complicated by the predominately out-of-plane flow that requires thick laser sheets and short interframe times, which increase noise and measurement uncertainty. Choosing appropriate experimental parameters requires compromise between the spatial and temporal resolution and the dynamic range of the measurement. To explore these challenges, we do a case study on the wake of a fixed wing. The fixed model simplifies*

the experiment and allows direct measurements of the aerodynamic forces via load cell. We present a detailed analysis of the wake measurements, discuss the criteria for making accurate measurements, and present a solution for making quantitative aerodynamic load measurements behind free fliers.

2.1 Introduction

As aircraft scale down in size, the effectiveness of the traditional aerodynamic tools founded upon potential flow analysis give way as the Reynolds number decreases. The details of moderate Reynolds number ($< 200,000$) effects, such as boundary layer separation, transition, and reattachment, play an increasingly important role in determining aerodynamic performance [2]. The drive to design Micro Air Vehicles (MAVs) has motivated the study of low Reynolds number aerodynamics, where effects traditionally considered non-ideal—such as sharp leading edge, low aspect ratio, and compliance—have been demonstrated to boost aerodynamic performance [30, 38, 40]. MAV design can be inspired by flapping animal flight; fliers that operate in a similar parameter space and demonstrate a variety of approaches for low Reynolds number flight. Studies have focused across the wide spectrum of animal fliers: insect [41], mammalian, and avian [42].

Several aspects make live animal flight experiments uniquely challenging. For example, vertebrate animal testing protocols require that aerodynamic forces be measured non-intrusively to the animal for both safety and behavioral reasons. Because the animal cannot be instrumented directly, aerodynamic forces must be inferred from the animal's wake. As a flier generates aerodynamic forces, it imparts momentum into the air, and the structure and the strength of the resulting wake contains the time-history of the wing loading. Conversely, a detailed knowledge about the strength and structure of the wake is requisite to understanding the history of the wing loading.

Fig. 2.1 depicts a classical wake roll-up behind a lifting body. In steady flight,

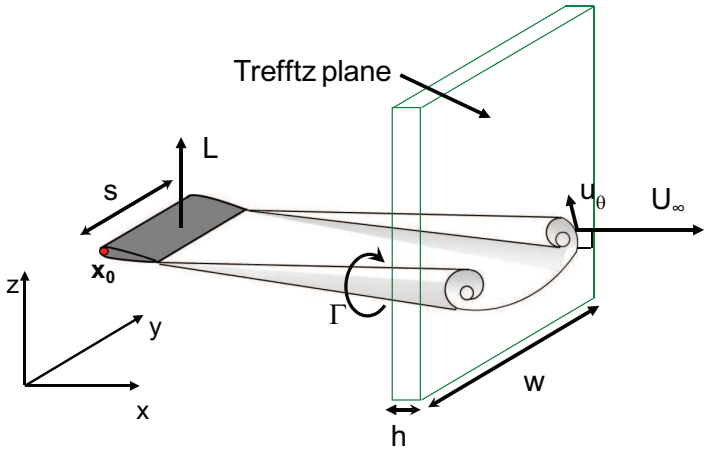

Figure 2.1: The wake roll up into trailing vortices behind a flier and the Trefftz plane. The flier has span s and generates lift L. The wake vorticity rolls up into a trailing vortex of strength Γ. The laser sheet illuminating the Trefftz plane has a thickness h and a width w. Under typical configurations, the component of velocity in the Trefftz plane u_θ is an order of magnitude smaller than the freestream U_∞. The red marker at the leading edge wing tip marks the origin.

the wake is dominated by the tip vortices. Unsteady fliers (e.g., animals or flapping micro air vehicles) can shed much more complex wake structures in which the tip vortices shift and change in strength, and in which there might be spanwise vortex structures as well as other discrete vortices. The vortex wake is advected with the local velocity and may be measured downstream of the flier either in a streamwise plane, or in a transverse ("Trefftz") plane. The Trefftz plane is the streamwise normal plane in the wake behind a flier ((y, z) plane in Fig. 2.1). Lift can be estimated from a measurement of the streamwise circulation in the Trefftz plane and application of the Kutta-Joukowski formula, $L = \rho U_\infty \Gamma s$. Here L is the lift, ρ is the air density, U_∞ is the freestream velocity, Γ is the circulation, and s is the span.

Spedding et al. [43, 44] conducted PIV experiments in a vertically-oriented streamwise plane behind a thrush nightingale. They measured the spanwise vorticity in the wake, and by applying Helmholtz's theorem, inferred the complete topology of the

vorticity distribution in the wake. From their experiments, Spedding et al. concluded that for slow flight speeds, the wake consists of closed vortex loops formed during each wing beat; whereas, for fast flight speeds, trailing vortices from each wing tip are intermittently joined by alternating positive and negative vortical "rungs" in a ladder-like topology.

Measurements in the Trefftz plane hold considerable appeal since, unlike the streamwise plane, the entire wake structure can be determined from the measurement. Hot wire measurements in the Trefftz plane were reported by Devenport and Rife [45]. They investigated the roll-up of the tip vortex behind a fixed NACA 0012 wing ($Re = 530,000$) and developed a theory to correct for vortex wander. They found that the shape of the roll-up spiral was approximately self-similar, growing as the square root of downstream distance. They also concluded that the vortex core was laminar. Gerontakos and Lee [46] used a seven-hole pressure probe to investigate the near wake of sweptback and rectangular planform wings fixed in a wind tunnel. At the location investigated behind the rectangular wing, they found that the tip vortex contained only 70% of the wing-bound circulation. Furthermore, they found that the vortex core contained only 75% of the tip vortex's circulation. Karakus et al. [47] used Trefftz plane PIV to study the development of the tip vortex on-wing and in the near wake a fixed NACA 0012 wing mounted in a water channel at $Re = 32,000$). The found that tangential velocity in the vortex reached a maximum at the trailing edge, and decreased with downstream distance. For angles of attack $\alpha = 4$–12° the maximum velocities were 15–40% of the freestream. Kaplan et al. [38] investigated the structure of vorticity behind several low aspect ratio fixed-wings at low Reynolds number using Trefftz plane PIV and dye visualization. They noted that the force measurements were in good agreement with the measured circulation despite differences in vortex structure and vortex dynamics between different planforms.

Within the biological flight community, the Trefftz plane approach has also been

popular for studying unsteady wakes. Time-resolved PIV measurements in the Trefftz plane behind several species of bats and birds have been reported in recent years [6–15]. These experiments have coupled measurements of the animals' kinematics with PIV wake measurements in the Trefftz plane, and have shown that these animals shed complex wake systems with multiple vortex structures whose strength and time-evolution vary, illustrating differences between birds and bats as well as between different species of the same order.

However, despite their appeal, Trefftz plane measurements in unsteady flows push the limits of PIV instrumentation, and there have been some concerns regarding the measured strength of the vortex structures. The intensity of the wake structures are relatively weak compared to the freestream velocity; therefore, adequately measuring the structures using PIV is challenging. The challenge arises because the PIV tracer particles are carried out of the interrogation volume by the freestream before their in-plane displacements are sufficiently large enough to be resolved.

To illustrate this, suppose in Fig. 2.1 that the azimuthal velocity associated with the streamwise vortex is $u_\theta/U_\infty = 0.1$. We consider a "typical" PIV configuration defined by a field of view measuring $w \times w$, where w might be 10 cm. In the time it takes a tracer particle to travel $0.005w = 0.5$ mm in the (y, z) plane, the particle's x-displacement is $0.05w = 5$ mm. To resolve this would require a laser sheet thickness, h of at least 5 mm, which is considered to be thick. Furthermore, the small oil particles typically used to seed air flows ($\approx$ 1–10 μm) are difficult to illuminate. Achieving large illumination volumes with sufficient image contrast is beyond the capabilities of typical PIV lasers.

These limitations in resolving the vortex strength have been recognized, and several authors [11, 12, 15] have noted that their quantitative analyses of the strength of the measured vortex structures fail to explain weight support of the free-flying animals. Hubel et al. [11] hypothesize that lift is under-predicted because they under-

measured the trailing vortex circulation. Henningsson et al. [12] instead argue that Crow instability distorts the wake, leading to under-prediction of lift. One might question the validity of any analysis based on experiments that fail to resolve the strength and structure of the topic features.

In this paper we explore and quantify the challenges associated with PIV-based wake measurements in the Trefftz plane behind low-speed fliers. We first develop a simple model and use this to estimate the velocities in the Trefftz plane for a low-speed flier with a given weight and aspect ratio. From this estimate, we demonstrate that a traditional PIV measurement cannot hope to accurately capture the Trefftz plane measurements with any desirable signal-to-noise ratio. In order to resolve this problem, we demonstrate a dual-plane PIV system that enables accurate measurements in these aerodynamic systems. Our predictions are validated using both single-plane and dual-plane PIV configurations in a model flow in the wake of a simple finite wing at a fixed angle of attack. Although this does not exhibit any of the complexities of a flapping wing wake (ladder structures, etc...), the simplification serves our objective to demonstrate an accurate technique for streamwise vortex measurements.

2.2 Wake Measurements in Wind Tunnels Using PIV

2.2.1 Estimating wake behavior

An important consideration for Trefftz plane PIV measurements is the relative magnitude of the in-plane velocity to the through-plane (freestream) velocity. We seek an estimate for the Trefftz plane velocities behind a flier supporting a weight W. We want a simple model to estimate the velocities that need to be resolved to accurately measure the wake vortex strength, and to estimate the area in which these velocities exist. We are not calculating the detailed vortex roll-up—for this, a sophisticated mathematical model is required [see 5, 48, 49]. Our goal is to calculate a characteristic wake size, r_0, within which most of the root circulation is contained, and the

characteristic velocity, $u_\theta(r_0)$, which represents the typical velocity which must be resolved to measure the total circulation.

We assume the wake rolls up into a pair of axisymmetric trailing vortices. The lift must exactly balance the weight in steady flight, therefore $L = W$. The parameters that describe the flier and wake are the freestream, U_∞, the air density, ρ, the chord length, c, the span, s, the lift, L, the root circulation, Γ_0, and the vortex size, r_0.

To complete our analysis we require models for the lift distribution on the wing and the structure of the vortices. For simplicity, we assume an elliptic lift distribution

$$\Gamma(y) = \Gamma_0 \sqrt{1 - \left(\frac{y}{s/2}\right)^2}, \tag{2.1}$$

and assume the Lamb-Oseen model for the spatial structure of the trailing vortex

$$u_\theta(r) = \frac{\Gamma_0}{2\pi r}\left(1 - \exp\left(-\left(\frac{r}{r_0}\right)^2\right)\right). \tag{2.2}$$

Using the freestream velocity, U_∞, air density, ρ, and chord length, c, to normalize, the resulting parameters are aspect ratio, $\mathcal{AR} = s/c$, normalized lift, $L^* = L/\rho U_\infty^2 c^2$, normalized circulation, $\Gamma^* = \Gamma/U_\infty c$, and normalized vortex size, $r_0^* = r_0/c$. It is worth noting that our normalized lift is not the traditional lift coefficient $C_L = 2L/\rho U_\infty^2 sc$, but rather $L^* = C_L \cdot \mathcal{AR}/2$. This choice of definitions allows us to vary the weight of the flier, L^*, and its geometry, $\mathcal{AR}$, independently.

The lift force is related to the wing root circulation by the Kutta-Joukowski formula for an elliptically loaded wing, as given by Kundu and Cohen [50]

$$L = \frac{\pi}{4}\rho U_\infty \Gamma_0 s. \tag{2.3}$$

In normalized form, Eqn. 2.3 simply becomes $L^* = \frac{\pi}{4}\mathcal{AR} \cdot \Gamma^*$. To determine the size of the vortex, we use the Betz circulation invariant in which the second moment of

vorticity remains invariant in a wake [5]. Given a Lamb-Oseen vortex with strength Γ_0, the second moment of vorticity of is uniquely defined by the characteristic size r_0. Following Donaldson et al. [49], we equate the second moment of the Lamb-Oseen vortex to the second moment of vorticity behind an elliptically loaded wing and solve for the vortex size, r_0, yielding

$$r_0^* = 0.1116 \cdot \text{Æ}. \tag{2.4}$$

Combining these results, we can write the expected wake structure solely as a function of the shape, Æ, and weight, L^*, of the flier:

$$\frac{u_\theta}{U_\infty}(r/c) = \frac{2L^*}{\pi^2 \text{Æ} \cdot r/c}\left(1 - \exp\left(-\left(\frac{r/c}{0.1116 \cdot \text{Æ}}\right)^2\right)\right). \tag{2.5}$$

Fig. 2.2a shows the behavior of Eqn. 2.5 for $L^* = 1$ at different aspect ratios. Although derived from assumptions about the lift and wake behavior, Fig. 2.2 demonstrates that typical velocities in the wake are quite small compared to the freestream. Fig. 2.2b demonstrates that velocities in the wake vary as Æ^{-2} because the increase in span reduces the wing loading and because the larger span increases the expected vortex size. Table 2.1 outlines the flight parameters of four different fliers: a Boeing 747 aircraft, an albatross, a common gull, and the model wing used for these experiments with dimensions inspired by bats.

2.2.2 PIV measurements

We now consider a Trefftz plane PIV measurement behind a flier in a wind tunnel and seek the required experimental parameters to accurately measure the flow. We consider a flier with span, s, which generates a lift, L, in a freestream, U_∞, and use the model developed in Sec. 2.2.1 to estimate the relevant properties of the wake. We also suppose a camera system with an $N \times N$ pixel^2 sensor. The typical experiment

Table 2.1: Comparison of estimated vortex properties from different fliers. The estimated properties assume elliptical wing loading. The maximum in-plane velocity corresponds to the maximum velocity of a Lamb-Oseen vortex with the given core radius. Boeing numbers adapted from Gerz et al. [51]. Albatross and gull numbers adapted from Shyy et al. [52]

	Lift, L [N]	Speed, U_∞ [m/s]	Chord, c [m]	Span, s [m]	Circulation, Γ_0 [m^2/s]	Est. vortex size, r_0 [m]	Max in-plane velocity, u_θ/U_∞ [-]
Boeing 747	$2.68 \cdot 10^6$	240	9.2	64.4	630	7.2	0.037
Albatross	87	19.2	0.20	3.05	1.58	0.34	0.025
Common Gull	3.7	9.2	0.10	1.15	0.371	0.13	0.032
Bat	$1.41 \cdot 10^{-1}$	5.0	0.083	0.303	0.104	0.034	0.063

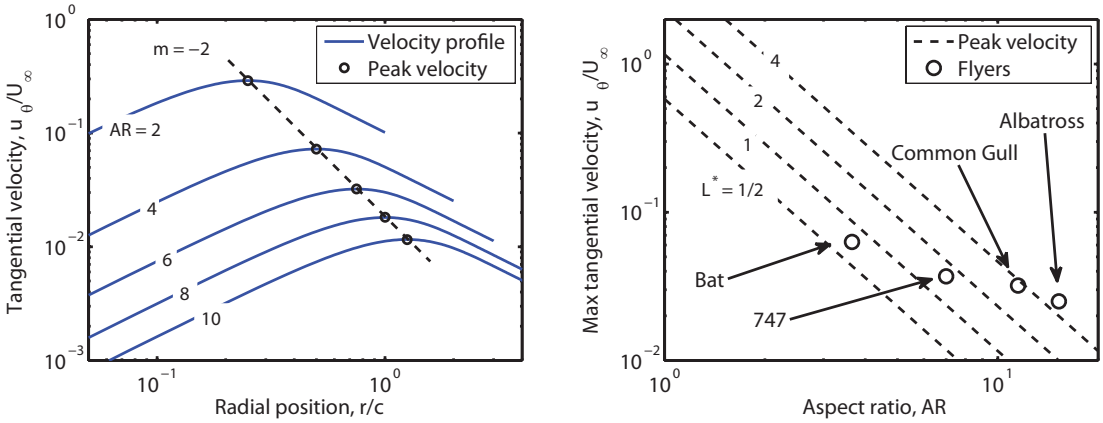

Figure 2.2: Fig. 2.2a shows how the trailing velocities can be expected to change with aspect ratio for a flier supporting a weight $W/\rho U^2 c^2 = 1$. The dashed line denotes the location and magnitude of the maximum velocity as aspect ratio varies. The slope, $m = -2$, indicates that the $u_{\theta,max} \propto \mathcal{R}^{-2}$. Fig. 2.2b shows the maximum velocity in the expected vortex profile as a function of aspect ratio $\mathcal{R}$ and lift L^*. Lower aspect ratio wings support lift over a shorter span leading to smaller, more intense wake vortices. The estimated example fliers from Table 2.1 are shown in Fig. 2.2b.

configuration is shown in Fig. 2.1.

We first determine the interrogation region size required to capture the rolled-up wake. The Lamb-Oseen vortex, given in Eqn. 2.2, contains 98% of the circulation within $2 \cdot r_0$ of the vortex center. For a PIV camera with a $w \times w$ field of view, we require $w = 4 \cdot r_0$. The size of the wake after roll-up is given by Eqn. 2.4; namely, $r_0 \approx 0.1116 \cdot s$. For simplicity, w is given by:

$$\begin{aligned} w &= 4 \cdot r_0 = 4 \cdot 0.1116 \cdot s \\ &\approx \frac{s}{2}. \end{aligned} \tag{2.6}$$

We now consider the particle image displacements, $\Delta\zeta$, on the camera sensor. The one-quarter rule [53] specifies that the maximum permissible image displacement is 25% of the interrogation window; for example, with the commonly used $32 \times 32\,\text{pixel}^2$,

interrogation window the displacements should be $\Delta\zeta < 8\,\text{pixel}$. For this exercise, we take $\Delta\zeta = 4\,\text{pixel}$ as the maximum pixel displacement of the particle images on the camera sensor. A pixel displacement of $\Delta\zeta$ on an $N \times N\,\text{pixel}^2$ sensor will correspond to the particle's physical displacement, Δz, given by

$$\Delta z = \frac{\Delta\zeta}{N} w. \tag{2.7}$$

The interframe time between PIV images (Δt) required to achieve the displacement given by Eqn. 2.7 is determined by the in-plane velocities and the camera field of view. Eqn. 2.5 gives the expected velocity distribution as a function of the span and lift of the flier. Consider the maximum in-plane velocity in the wake, $\upsilon \equiv u_{\theta,max}/U_\infty$, then the maximum particle displacement will be $\Delta z = \Delta t \cdot U_\infty \cdot \upsilon$. Rearranging for Δt and using Eqns. 2.6 and 2.7 yields the requisite interframe time:

$$\Delta t = \frac{\Delta\zeta}{N} \cdot \frac{s}{2 \cdot U_\infty \cdot \upsilon}. \tag{2.8}$$

The strong out-of-plane velocity (streamwise) limits interframe time delay to times less than the seeding particles' residence time in the interrogation volume. Consider the laser sheet thickness h as shown in Fig. 2.1. The flow will displace a distance $\Delta x = U_\infty \cdot \Delta t$ between the image exposures. To ensure a good correlation requires that a large percentage of the imaged seed particles are present in both images, namely $\Delta x \ll h$. Furthermore, as the freestream carries the particles out of the interrogation volume between images, it introduces into the interrogation volume new particles that increase the measurement noise via false correlation [54]. The strength of the correlation depends on retaining the same seed particles in both PIV images. We call

the percentage of particles present in both images the volume retention V_R:

$$\begin{aligned} V_R &= \frac{h - U_\infty \cdot \Delta t}{h + U_\infty \cdot \Delta t} \\ &\approx 1 - 2\frac{U_\infty \cdot \Delta t}{h}. \end{aligned} \tag{2.9}$$

Best results are achieved when V_R is close to unity—this condition is satisfied by choosing a sufficiently thick laser sheet. Combining Eqn. 2.8 and 2.9 yields the expression for the required laser sheet thickness:

$$h = \frac{1}{1 - V_R} \cdot \frac{\Delta\zeta \cdot s}{N \cdot \upsilon}. \tag{2.10}$$

Typical experimental parameters are given in Table 2.2. A 1 megapixel camera is assumed for imaging the wakes of the fliers presented in Table 2.1. Eqns. 2.8 and 2.10 are used to calculate the parameters for Trefftz plane PIV measurement.

It is evident that the computed laser sheet thicknesses are impossibly large and that the ideal conditions of 4 pixel displacements and 90% volume retention are unreasonable using a fixed, thick laser sheet. Disturbingly, however, even when the criteria for pixel displacement and volume retention are relaxed to very modest values ($\Delta\zeta = 1$ pixel and $V_R = 75\%$), the required laser sheet thickness is still prohibitively thick. One must choose between measurement dynamic range and image contrast when choosing an appropriate laser sheet thickness h and interframe time Δt. Alternatively, the field of view, w, can be reduced at the expense of capturing the full wake structure, or the volume retention, V_R, can be relaxed at the expense of valid-peak detection and measurement noise.

Animal flight experiments are subject to further experimental restrictions. For example, the wing beat frequencies for bats are on the order of $5 - 10$ Hz; therefore, high-speed PIV systems are employed to resolve the flow structures throughout the wing beat cycle [8, 11]. Additionally, large areas are swept by the wing throughout the

Table 2.2: Hypothetical experimental parameters for a single plane Trefftz plane PIV measurement. We assume the wake behaves according to Table 2.2. A 1 megapixel camera is assumed ($N = 1024$). The required field of view, w, is given for each flier. The desired interframe time, Δt, and laser sheet thickness, h, are calculated for the specified $\Delta\zeta$ and V_R. The downstream displacement of the tracer particles $\Delta\zeta$ is shown for each flier-Δt combination

		$\Delta\zeta = 4$ pixel $V_R = 90\%$			$\Delta\zeta = 1$ pixel $V_R = 75\%$		
	w [m]	Δt [μs]	Δx [mm]	h [mm]	Δt [μs]	Δx [mm]	h [mm]
Boeing 747	32.2	14000	4400	$6.8 \cdot 10^4$	3500	850	$6.8 \cdot 10^3$
Albatross	1.52	12400	240	$4.8 \cdot 10^3$	3100	60	$4.8 \cdot 10^2$
Common Gull	0.58	7600	70	$1.4 \cdot 10^3$	1900	17.5	$1.4 \cdot 10^2$
Bat	0.152	1900	9.4	190	470	2.3	19

flapping cycle, requiring fairly large interrogation areas to capture the entire wake. High-speed systems are limited in camera resolution and laser energy and require a compromise between measurement area and dynamic range. For example, Hubel et al. [11] required a 200 Hz PIV system to study a bat wake. In contrast, Willert et al. [55] studied the wake of a wing using a low-repetition, high-power PIV system with a traverse mounted camera to scan the wake region. The high-power laser plus the ability to scan permitted a thicker laser sheet and much higher spatial resolution.

Table 2.2 shows that prohibitively large h is a result of the requirement for $\Delta x \ll h$. The compromise on the laser sheet thickness and interframe delay can be greatly relaxed by displacing laser sheet by Δx between images; however, moving the laser sheet is an old concept. Several techniques have been previously employed to scan a laser sheet to obtain velocity data throughout a volume [56]. These systems employed motor driven scanners or rotating mirrored cylinders to move the laser sheet. Gharib et al. [57] demonstrated three-component velocity measurements using a single camera and image triplets (as opposed to standard image pairs), where the third image was captured in a plane displaced in the out-of-plane direction of the laser sheet. This system utilized a scanning mirror to displace the laser sheet for the third image. In

the context of high-speed Trefftz plane measurements, an opto-mechanical system for shifting the laser sheet would need to be capable of operating at the speed of the PIV system, in this case 200 Hz. Another approach to laser sheet displacement is to purposely misalign the beam-combining optics in a dual-cavity laser [38]. This method allows a displacement comparable to the thickness of the laser sheet; however, a drawback is that the misalignment is susceptible to drift and requires constant re-tuning.

An interesting suggestion was made by Landreth and Adrian [58] for image shifting with regard to issue of ambiguity removal for single-image, double-exposure PIV. They propose an electro-optical method of modulating the optical path to the camera, which has the benefits of being independent of mechanical motions, increasing the repeatability and accuracy of the image shift. This electro-optical approach can be applied for repeatable high-speed switching between two optical paths, and we chose this approach for moving the PIV laser sheet.

2.3 Experimental Methods

We have selected a model experimental configuration on which to assess the limitations of single-plane PIV and the advantages of dual-plane PIV. The model is a fixed wing, with dimensions typical of moderately-sized animals and Micro Air Vehicles, immersed in a free stream typical of these applications. All experiments were conducted using the same wing model. The wing had a rectangular planform and NACA 0015 cross-section. The rectangular planform was selected so as to provide a well-defined wing tip for rapid tip vortex formation. The wing chord was 8.3 cm, and the full span was 30.3 cm. The wing was mounted at the quarter-chord and at mid-span. A matte black paint doped with florescent dye (Rhodamine-B) was used to minimize glare from the wing during PIV experiments.

2.3.1 Wind tunnel

The experiments were conducted in the Brown University low-speed wind tunnel. The facility is a closed-return tunnel with a $60 \times 82\,\mathrm{cm}^2$ test section. The experiments were conducted at freestream velocities of 5–7.5 m/s, which correspond to chord Reynolds numbers of $Re = 27,000$–$42,000$. Freestream turbulence levels are $< 0.1\,\%$. The tunnel ceiling allows angular adjustment to compensate for wall boundary layer growth; pitot tube measurements confirm (to within measurement accuracy of 1 % freestream) that the freestream velocity is uniform along the length of the test section and uniform across the central 90 % of the section width.

The test section is fitted with a 2 m linear rail on the tunnel floor to allow precise placement of the model within the test section. The rail's alignment with each other and with the axis of the wind tunnel was within 0.1°, corresponding to an absolute position uncertainty between the far ends of the rail of less than 3.5 mm. The wing was sting-mounted on a rail sled, which allowed the wing model to be moved to any position along the linear rail. A 6-axis force/torque transducer (ATI nano17) was fixed between the sting and the wing for direct force measurement. The force was monitored at 2 kHz for 30 seconds during each trial.

The environmental conditions in the tunnel were monitored simultaneously with the experiment. The freestream velocity was monitored with a pitot tube and differential pressure transducer (Setra Model 239), while the atmospheric pressure was monitored by an absolute pressure transducer (Setra Model 270). A thermistor probe and digital controller (Omega DP25-TH) monitored the temperature. All signals were sampled at 2 kHz for 30 seconds during each trial.

2.3.2 Single-plane PIV

The single-plane PIV setup was a conventional PIV system running commercial PIV software (DaVis v7). The configuration was the same setup used by Hubel et al.

[9, 11] except that only a single camera was required. The camera (Photron FASTCAM1024) was fitted with a 532 nm line-pass filter and Nikon Nikkor 105 mm/2.8 D lens. The camera was mounted inside the test section behind the wing tip. The camera was calibrated using a LaVision Type 31 calibration target and the software's single camera calibration routine. The imaged region measured $12.5 \times 12.5\,\mathrm{cm}^2$, corresponding to $R = 8.1\,\mathrm{pixel/\,mm}$, which was twice the linear spatial resolution used by Hubel et al. [9, 11] for bat-flight experiments. The higher magnification was possible because the location of the wake behind a fixed-wing is more predictable than behind a flapping-wing. Furthermore, because the increased spatial resolution provides larger pixel displacements, $\Delta\zeta$, for a given physical displacement, Δz, as defined above (Eqn. 2.7).

The laser used was a 200 Hz dual-oscillator frequency-doubled pulsed Nd:YAG (Litron LPY-700). The measured energy per pulse was at least 45 mJ. The laser was synchronized via trigger signals provided by a computer-programmed timing unit. The laser output was guided to the test section with an articulated laser arm with a focusable output optic and sheet forming optic (cylindrical lens, $f = -20\,\mathrm{mm}$). The arm/lens system was affixed to the top of the test section via a positioning mechanism that allowed precise control of the laser sheet position and orientation. The laser sheet normal was aligned with respect to the axis of the test section to 0.1°, aligned with the wing's trailing edge, and centered at the wing tip. The optics were focused at a point far beyond the floor of the test section, such that the laser sheet thickness was 2 mm at the location of the wing tip. The change in the laser sheet thickness varied less than 0.5 mm throughout the imaged region. To meet the volume retention condition (Eqn. 2.9), Δt was chosen such that $V_R \approx 70\%$.

The flow was seeded with Di(2-ethylhexyl)sebacate oil droplets that were atomized with a Laskin nozzle producing 1 μm droplets. The camera lens was slightly defocused to make the particle image size a few pixels in diameter; however, this was at the

expense of decreasing the overall image contrast.

Experiments were conducted with the wing located several distances upstream from the laser sheet (3, 4, 5, 10, 15, and 20 chords). A sequence of 750 image pairs were captured at each location. The images were processed with a two-pass cross-correlation algorithm. The first pass used a $64 \times 64\,\text{pixel}^2$ window, and the final pass used a $32 \times 32\,\text{pixel}^2$ window with 50% overlap, corresponding to a vector spacing of 2 mm. The vector fields were imported into MATLAB for analysis. The vorticity was calculated using a first-order differencing operator, and circulation was calculated from the area integral of vorticity. The average vortex location was identified in each trial from the location of maximum vorticity of the time-series average and was calculated to sub-grid accuracy using a three-point Gaussian fit about the peak value. The instantaneous vortex position was found by cross-correlating each vorticity field with the time-averaged field to find the relative displacement from the average position. These displacements were then used to recalculate the averages with all vortex centers aligned.

2.3.3 Dual-plane PIV

The dual-plane PIV experiment was configured to move the laser sheet with the freestream and is illustrated in Fig. 2.3. A Pockels cell (Linos LM8 99) was used to modulate the polarization vector between laser pulses, switching between laser sheet locations using a lateral displacement calcite crystal. The first laser pulse is passed unmodulated and reaches the calcite polarized in the crystal's ordinary axis; the beam passes straight through as depicted by path (a). The half-wave voltage is applied to the Pockels cell during the second laser pulse; the laser pulse reaches the calcite polarized in the extraordinary axis and is displaced laterally as depicted by path (b). The total displacement distance is only a function of the crystal length.

The Pockels cell was driven by a high-voltage pulse amplifier (Analog Modules

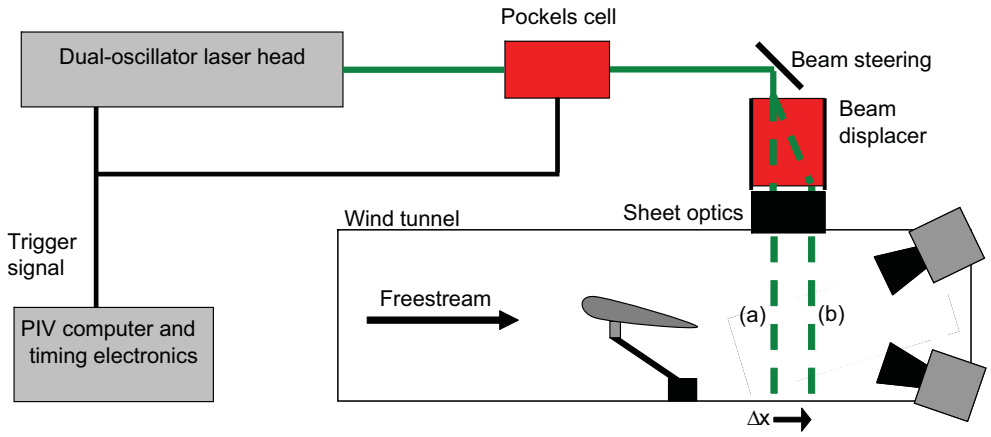

Figure 2.3: The setup for the dual-plane PIV experiment is configured in the same way as a typical stereo PIV experiment with the addition of a Pockels cell and a calcite beam displacer (shown in red). The first image is captured at location (a). The Pockels cell rotates the polarization of the second laser pulse, causing the beam to be displaced by the calcite in the direction of the flow for the second image at location (b).

8261A). A half-wave plate was mounted after the beam steering optics to orient the polarization states to the axis of the beam displacement crystal (Thorlabs BD27). The total beam displacement was 2.7 mm.

Synchronization between the PIV system and the beam-displacement system was achieved by synchronizing a delay-generator with the second laser's flashlamp trigger signal. The delay-generator produced a delayed TTL pulse that was amplified by the pulse amplifier to drive the Pockels cell. The required interframe delay time depended on the time required for particles moving in the freestream to displace by $\Delta x = 2.7\,\text{mm}$, namely $\Delta t = \Delta x / U_\infty$. The volume retention, V_R, of the displaced laser sheet system is unity (to first-order—out-of-plane particle losses may still be present due to velocity deficit or surplus in the wing wake). The laser sheet thickness can be reduced so that higher contrast images can be captured. The laser sheet waist was 0.5 mm.

A stereo PIV configuration was employed to accurately account for the very large out-of-plane component of the particles' motion. Dual cameras (Photron FASTCAM1024) captured the images. The cameras were mounted outside the test section

and fitted with 50 mm Nikon lenses on Scheimpflug adapters to align the image planes with the laser sheet plane. The angle between each camera axis and the laser plane was about 43°. Following initial camera calibration, the stereo auto-calibration routine was utilized to account for any misalignment of the calibration target with the image plane. Five-hundred image pairs were captured for each downstream location. The interrogation region was $24.5 \times 24.5\,\mathrm{cm}^2$, twice that of the single-plane PIV experiments. The large field of view is a practical limitation of the camera arrangement outside of the test section. This field of view yields a resolution of $R = 3.5\,\mathrm{pixel/mm}$, which is similar to that used by Hubel et al. [11]; therefore, it is a good demonstration of this technique's performance for animal flight studies. The images were processed with a two-pass cross-correlation algorithm. Both passes used a $32 \times 32\,\mathrm{pixel}^2$ window with 75% overlap, corresponding to a vector spacing of 2.3 mm. The vector fields were imported into MATLAB, and the analysis described in Sec. 2.3.2 was repeated. The PIV configurations are summarized in Table 2.3.

2.3.4 Uncertainty analysis

The two experiments described above were conducted with different magnification factors, which will result in a difference between the pixel displacement uncertainties of each experiment. Furthermore, the 3-component (3C) analysis of the stereo measurement may reduce the measurement uncertainty in the dual-plane experiment compared to the 2-component (2C) analysis of the single-plane experiment. We consider these factors and compare the uncertainty in the measurement of the physical displacement of the tracer particles in each experiment. Consider the uncertainty in pixel-displacement measurement of the single-camera cross-correlation to be σ (typically, $\sigma \approx 0.1\,\mathrm{pixel}$ [59]). Following the analysis of Lawson and Wu [60] and Doorne and Westerweel [61], for cameras with off-plane angles of $\theta \approx 45°$, the pixel-displacement uncertainty is σ in the out-of-plane direction and $\sigma/\sqrt{2}$ in the in-

plane direction. Let the uncertainty of the physical particle displacements be δ. The 2C uncertainty is given by $\delta_{2C} = \sigma/R_{2C}$ and the 3C in-plane uncertainty is given by $\delta_{3C} = \sigma/\sqrt{2}R_{3C}$. The ratio of the displacement uncertainty between the two experiments is $\delta_{2C}/\delta_{3C} \approx 0.6$. Clearly, the single-plane experiment is capable of resolving smaller particle displacements than the dual-plane experiment; however, the larger Δt in the dual-plane experiment allows resolution of smaller velocities. The velocity uncertainty is given by $\sigma_u = \delta/\Delta t$. The velocity uncertainty of the single-plane measurement is 3% of the freestream, while the velocity uncertainty of the dual-plane experiment is 0.8% of the freestream. The vorticity is calculated from finite differences in the velocity field and its uncertainty will depend on the velocity uncertainty and the vector spacing. In our experiments, the vectors spacing was similar between the single- and dual-plane measurements (2 mm vs 2.3 mm, respectively); therefore, the ratio of uncertainties in the vorticity will reflect the ratio of uncertainties in the velocity. Letting Δy be the vector spacing, the uncertainty in the vorticity, σ_ω, is given by $\sigma_\omega = \sqrt{2}\sigma_u/\Delta y$. The normalized vorticity uncertainty $\sigma_\omega \cdot c/U_\infty$ is 1.96 in the single-plane experiment and 0.38 in the dual-plane experiment.

2.4 Results and Discussion

2.4.1 PIV measurement quality

We implemented a dual-plane PIV system to address the issue of small pixel displacements inherent in the traditional PIV configuration. Fig. 2.4 shows the center of a sample $64 \times 64\,\text{pixel}^2$ cross-correlation map from each PIV technique. The maps were sampled at the edge of the vortex core where velocity is the strongest. Fig. 2.4a shows the single-plane correlation map and demonstrates how small the pixel displacements are. Even in the strongest region of flow, the particle displacements are less than 1 pixel. Measurement of the velocity from the single-plane experiment is an exercise in sub-pixel interpolation.

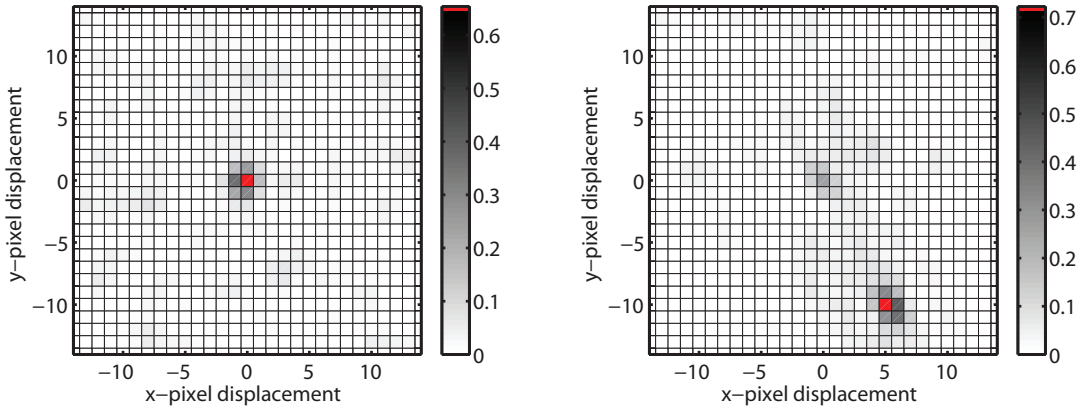

(a) Single-plane **(b)** Dual-plane, Camera A

Figure 2.4: Sample normalized correlation coefficient maps from the vortex core region as measured from each experiment are shown. Fig. 2.4a demonstrates the sub-pixel displacement from the region of largest displacement in the single-plane measurement. Fig. 2.4b shows the drastic increase in the displacements using the dual-plane technique. Note the secondary correlation peak at zero displacement.

Fig. 2.4b shows the correlation map from one camera recording the dual-plane experiment. The peak correlation is located approximately 11 pixels from zero displacement. This rather large pixel displacement is due to the large oblique camera viewing angle inherent in stereo PIV configurations (Table 2.3). The wake structures do not cause this large pixel displacement; rather, there is a large bias displacement due to the component of the freestream velocity in the image sensor plane.

Fig. 2.4b also demonstrates an important feature of digital recording. The second strongest peak in the correlation map is located at zero displacement. The presence of a strong secondary peak at zero displacement suggests the presence of camera ghosting. Ghosting is a residue of the previous exposure in the current image. The consequences for image correlation are obvious: if a residue of the first image is present in the second image of a PIV image pair, the residue will produce a "ghost" correlation peak at zero displacement. If the true correlation peak is in the neighborhood of the ghost peak, the computed correlation peak will be biased towards zero. If the true correlation peak lies sufficiently far from the ghost peak, the bias will be

negligible. An ideal camera sensor will exhibit zero ghosting; however, ghosting is often present in real systems, as it is in this case. The impact of camera ghosting can be difficult to quantify. Suppose two successive real images with no correlation are recorded. Ghosting in the recorded images can be detected by a correlation between the recorded images. However, in a PIV experiment the images are designed to be strongly correlated. If particle displacements are sub-pixel, correlation due to camera ghosting is indistinguishable from the desired correlation.

The maximum pixel displacement is important for understanding the dynamic range of a PIV measurement, especially in a 2-component PIV experiment where the camera is oriented normal to the interrogation plane. In a stereo PIV configuration, however, the cameras are oriented at an oblique angle to the interrogation plane. The dynamic range of the experiment depends upon the distribution of displacements. Fig. 2.4a shows the large pixel displacement at one location, but that vector will be distinguishable from other vectors only if there is an appreciable distribution in pixel displacements.

Fig. 2.5 shows the distribution of pixel displacement magnitude in the single- and dual-plane experiments. The single plane measurement (Fig. 2.5a) yields pixel displacements that are all less than one pixel, limited by the restriction of short interframe time delays. Outside of the vortex core, the flow-field is weak with pixel displacements on the order of 0.2; this is very near to the resolution limit of the cross-correlation algorithm, which is about 0.1 pixels. The strongest flow regions at the core of the vortex have maximum pixel displacement magnitudes of 0.5 pixels; hence, the dynamic range of the single-plane measurement is about 5.

The dual-plane experiment allowed longer interframe time delays resulting in a broader range of pixel displacement values (Fig. 2.5b). The range of displacement magnitudes vary from about 8 to 12. The distribution of displacements is much larger than the single-plane experiment, providing an order of magnitude larger dynamic

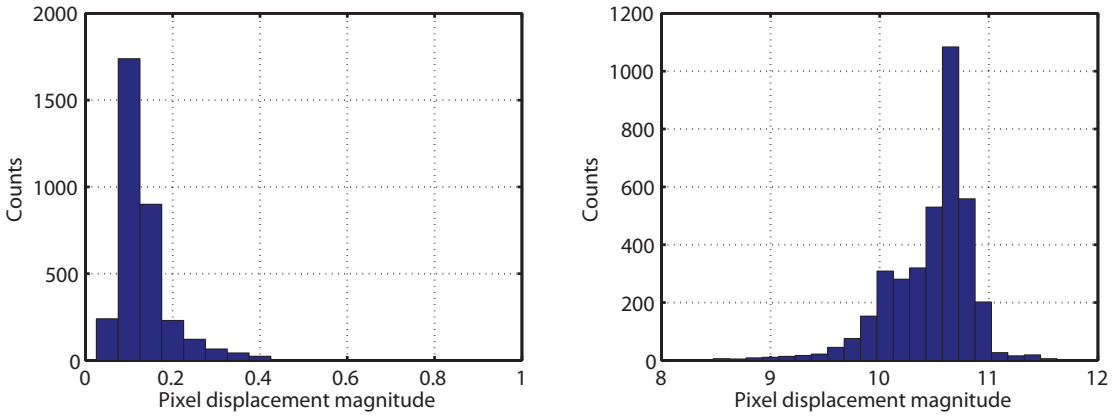

(a) Single-plane **(b)** Dual-plane

Figure 2.5: Distribution of pixel displacement magnitudes for the single-plane (Fig. 2.5a) and the dual-plane experiments (Fig. 2.5b).

range (≈ 40). The increased dynamic range of the dual-plane experiment allows the smaller velocities to be accurately resolved.

It should be noted that the spatial resolution of the single-plane experiment is more than twice the spatial resolution of the dual-plane experiment. The magnification of the single-plane experiment was increased from "typical" experiment parameters [e.g., 11] to maximize the particle image pixel displacements.

2.4.2 Vortex structure

Fig. 2.6 shows typical time-averaged streamwise vorticity fields at a station 10 chords downstream as measured by each of the PIV experiments. The vorticity contours from the left wing tip region are shown on a logarithmic scale to emphasize the entire structure, much of which consists of low-level vorticity outside the main core region. Vorticity from the trailing edge of the wing rolls up in a spiral around a well-developed vortex core that has been studied analytically [e.g., 48] and experimentally [e.g., 45]. The single plane measurement (Fig. 2.6a) of the wake suggests a low-level vorticity spiral around the vortex core, which has a maximum normalized vorticity ($10 \cdot log_{10}(\omega c/U_\infty)$) of 7.8. The roll-up structure is verified by the dual-plane

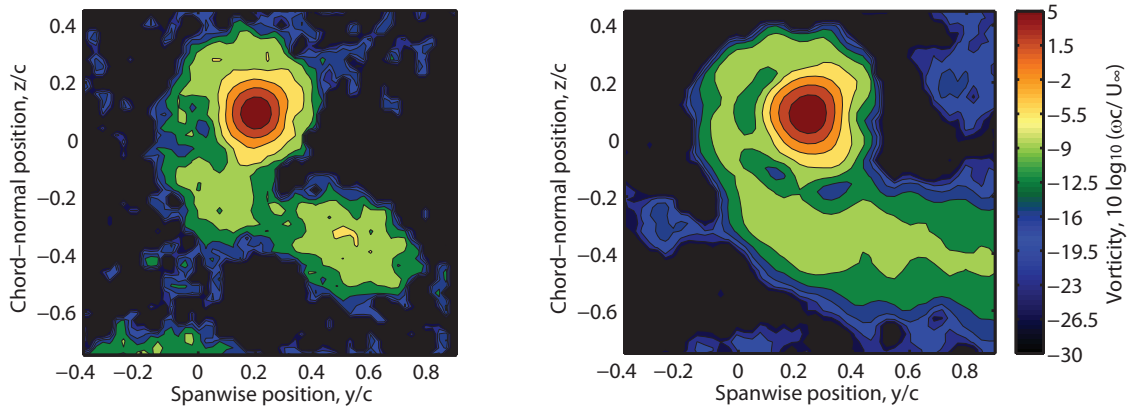

(a) Single-plane, $\frac{x}{c} = 10$ **(b)** Dual-plane, $\frac{x}{c} = 10$

Figure 2.6: Measured vorticity contours from each experiment at $x/c = 10$ are plotted on a logarithmic scale ($10 \cdot log_{10}(\omega c/U_\infty)$). The single-plane measurement in Fig. 2.6a has a peak value of 7.8. The dual-plane measurement in Fig. 2.6b very clearly illustrates the vorticity spiral outside the vortex core and demonstrates a stronger core with less noise in the outer flow. The peak value is 8.5.

measurement (Fig. 2.6b); however, the peak measured vorticity is 8.5. The vorticity spiralling outside the core is about 15 dB below the peak values. The measurement uncertainty of the vorticity is −11.6 dB in the single-plane average and −17.6 dB in the dual-plane average. The "patchy" appearance of the vortex in Fig. 2.6a is likely due to measurement uncertainty being same magnitude as the outer vorticity.

The estimated wake roll-up behavior from Sec. 2.2.1 predicted the radius of a Lamb-Oseen vortex to be 0.4 chords. Both Fig. 2.6a and Fig. 2.6b indicate a vortex much smaller than this estimated value. The disagreement is perhaps not surprising since the model is derived from using the Betz's circulation invariants assuming a Gaussian vorticity distribution (i.e., Lamb-Oseen) and an elliptic wing loading. As Fig. 2.6 shows, the vorticity distribution this close to the trailing edge is not Gaussian, are there is still vorticity in the winding spiral outside the core. A reasonable estimate of the distance downstream when the trailing vortices become approximately Lamb-Oseen is given by Moore and Saffman [48] as $x/c \approx 0.01 Re_{\mathcal{A}} \mathcal{R}^2$. This distance is 3700 chords in the single-plane experiment and 5500 chords in the dual-plane ex-

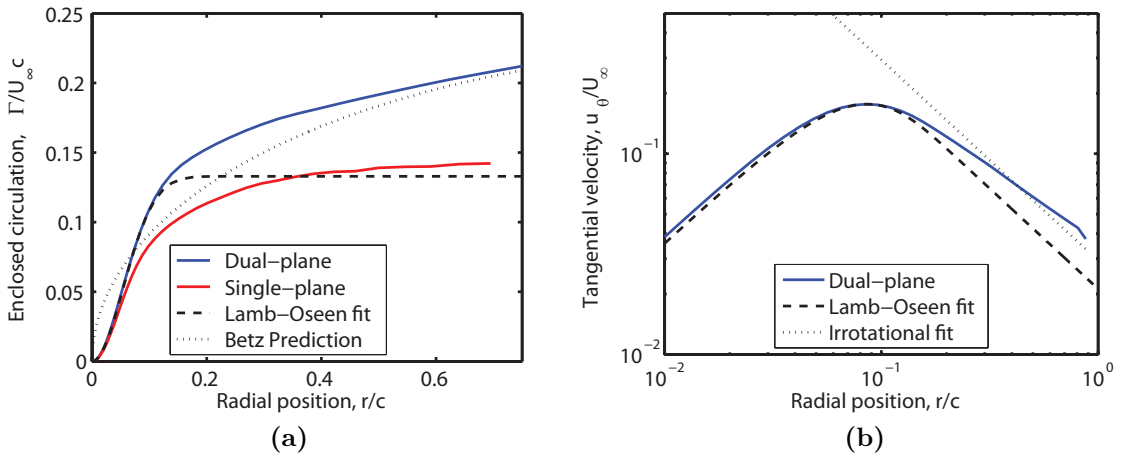

Figure 2.7: Vortex profiles are compared. Fig. 2.7a shows the circulation profiles from the single and dual-plane measurements at $x/c = 10$. A Lamb-Oseen vortex fit to the core of the dual-plane measurement and theory by Betz [5] are shown for comparison. Fig. 2.7b shows the theta-averaged tangential velocity profile of the trailing vortex measured by the dual-plane experiment. Two vortex fits are also shown. The Lamb-Oseen vortex is fit to the core region of the vortex by finding the location and value of the velocity maximum. The irrotational vortex has been fit to the region outside the core using a least-squares fit.

periment. The implication of a small vortex core is that larger peak velocities exist than are predicted by the analysis. Moore and Saffman [48] also give an estimate for the radius of maximum tangential velocity, $r/c = 2.92\sqrt{x/c} \cdot Re^{-1/2}$. We compare this prediction to the velocity profile measured at $x/c = 10$ (Fig. 2.7b). Moore and Saffman's equation predicts maximum velocity at $r/c \approx 0.056$ compared to the measured value $r/c \approx 0.08$. It should be noted that the correlation window used in the PIV evaluation is $0.11c$. Accurate measurement of the vortex core requires even higher spatial resolution.

The fact that the model is based on an elliptic wing loading while the experiment uses a rectangular wing also contributes to a difference between the model predictions and the PIV measurements. However, for relatively low aspect ratio wings, as is the case in these experiments, the difference between the wing loading on rectangular and elliptical wings vanishes [62]. Furthermore, we emphasize that the objective of

the model developed earlier is not to give a high-accuracy prediction of vortex wake structure and strength, but only to provide a guide for PIV parameter choices.

Fig. 2.7a shows the circulation enclosed as a function of the radial distance from the vortex center as measured by each PIV technique at $x/c = 10$. A Lamb-Oseen profile is fit to the measured core region and we see that a good fit is achieved for $r/c < 0.1$. Note that this is an empirical fit to the vortex core, and not to be confused with the use of the Lamb-Oseen vortex in Sec. 2.2.1. The Lamb-Oseen vortex was fit by matching the location of and magnitude of maximum tangential velocity. We see that the Lamb-Oseen model is an appropriate description of the vortex in the core; however, outside of the core, the measured circulation continues to increase while the Lamb-Oseen circulation levels off. A theoretical prediction using the Betz model (outlined in Donaldson et al. [49]) is shown in Fig. 2.7a. The model neglects viscosity and thus fails in the core region; however, the model provides a reasonable description of the wake outside of the core and of the total circulation as r/c increases. The single-plane PIV measurement significantly under-predicts the circulation.

The steady increase in the circulation outside of the core indicates that the flow is not irrotational. Fig. 2.6 clearly shows vorticity outside the vortex core. Outer flows with vorticity have already been observed experimentally [e.g., 38, 45, 47, 63], and predicted theoretically [e.g., 4]. Not all vorticity generated by the wing rolls into a tight vortex core; however, the vorticity spiraling outside of the vortex core is part the total circulation budget of the trailing vortex system in the wake. In order to measure the full strength of the wing's bound vortex, accurate flow measurement in the region outside of the vortex core is required to resolve the vorticity that remains exterior to the core. A measurement that is only capable of resolving the flow in the core region will under-resolve the vortex strength because it is not capturing all of the vorticity. Measuring the details inside the vortex core is not a requirement for accurate measurement of the total circulation.

Fig. 2.7b shows the dual-plane PIV measured velocity profile and the core-fit Lamb-Oseen vortex. The inner vortex region matches the linear velocity behavior of the viscous region of the Lamb-Oseen vortex; however, the measured data has a slight upward shift. This appears to be due to a more gradual transition between the inner and outer limiting behavior of the measured vortex. Recall that the Lamb-Oseen vortex is the model for laminar decay of a line vortex, while the measured tip vortex is the roll-up of a vortex sheet. The soft transition region between the viscous core and outer region could be attributed to the smoothed out spiral structure described by Saffman [4]. This region, however, occurs at the limit of the measurement's spatial resolution ($\approx 0.06c$); a higher resolution measurement would be required to investigate this region in sufficient detail. Outside of the core ($r > 2r_c$), the Lamb-Oseen model approaches $1/r$ behavior, and the measured velocity profile deviates from the model. The outer vortex region was fit with an irrotational vortex in a least-squares sense. The flow outside of the vortex core is not completely irrotational.

One method that has been proposed to calculate vortex strength from PIV data involves thresholding the data and fitting a Gaussian vorticity distribution [12, 43, 44]. However, the low level vorticity outside of the vortex core is lost in this approximation and the core-fit Gaussian vorticity distribution may not capture the full circulation leading to an under-prediction of the vortex strength.

2.4.3 Vortex position

Even though the strength and structure of the measured vortices is not fully resolved by the single-plane PIV, we can still ask if the overall wake topology and the location of the wake vortices can be faithfully captured. To address this, the position of the vortex core was measured as a function of downstream distance (Fig. 2.8). Both the single-plane and dual-plane PIV measurements observe the same vortex trajectory. The initial vortex position is just above and inside of the wing tip. As the measurement

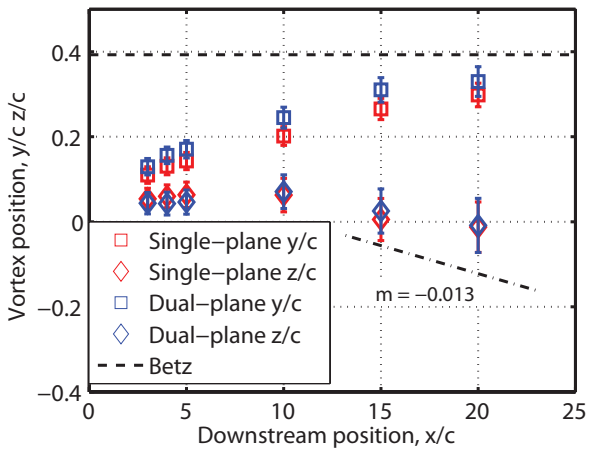

Figure 2.8: The measured vortex behavior from each experimental technique is compared. The two experiments agree quite favorably on the evolution of the vortex location downstream. Betz's spanwise position asymptote for elliptical wing loading is shown for comparison. The rate of vertical descent expected from the two oppositely signed trailing vortices is also shown.

plane moves downstream and the vortex sheet rolls up, the spanwise position of the vortex moves inboard and towards the position predicted by Betz' analysis [5], plotted for reference in Fig. 2.8. The measured vortex never reaches this asymptotic value, probably due to the limited downstream distance over which the measurements were performed (20 chords) and the difference between the experimental lift distribution and the elliptic wing distribution assumed in the Betz theory.

Fig. 2.8 also shows the vertical position (z) of the vortices. Two oppositely signed vortices translate together under each other's influence; therefore, we expect the steady decrease in the z-position of the vortex after the completion of roll-up. The rate of descent estimated from the last measured vortex separation and strength is shown. When $x/c > 10$, this behavior is evident; however, in the near wake region, the z-position is nearly constant. In fact, there is a slight increase in the z-position. The vortex resulting from the roll-up of a semi-infinite vortex sheet has increasing z-position [4]. Experimental observation of apparent upwash of the trailing vortex system in the near wake of low aspect ratio wings at low Reynolds numbers was also

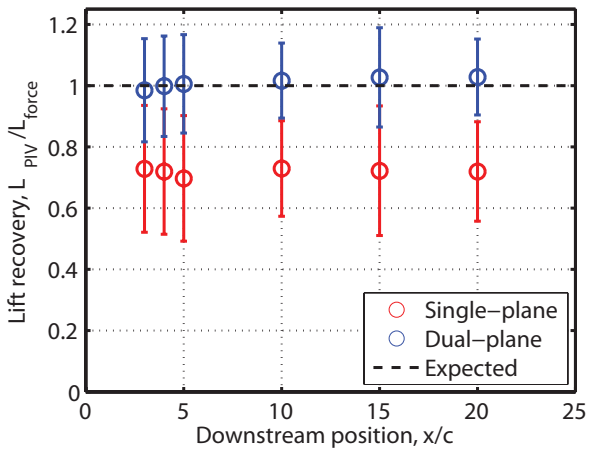

Figure 2.9: The PIV measured circulation from each experiment is compared to the direct lift measurement using the Kutta-Joukowski formula. The vortex strength is captured in the dual-plane experiments, but only partially in the single-plane experiments.

reported by Kaplan et al. [38].

Overall, the agreement between the two techniques in the measured vortex position is quite good. Despite limited ability to capture low level vorticity outside the core, the single-plane PIV technique appears capable of accurately locating the vortex structures.

2.4.4 Recovered lift

The estimates of the lift force from the PIV measurements are shown as a function of the downstream distance in Fig. 2.9. The force is predicted from the measured circulation using the Kutta-Joukowski formula and is compared with the lift force measured directly using the load cell. The dual-plane PIV measurement captures the expected circulation; however, the measured circulation from the single-plane PIV measurement fails to match the measured forces.

Circulation was calculated from integrating the vorticity over the measured Trefftz plane. Fig. 2.6 demonstrates lower vorticity in the single-plane measurement compared to the dual-plane measurement. Furthermore, it appears that parts of the vor-

ticity spiraling outside the core are missing, apparently lost in the measurement noise. Fig. 2.5 demonstrates the low dynamic range of the single-plane measurement—the majority of the measured flow field is at the limit of uncertainty of the cross-correlation algorithm. Fig. 2.7 shows the measured velocity contours and suggests that accurate measurement in the outer spiral region of the wake is requisite to capturing the full circulation strength. The sub-pixel displacements of the single-plane measurement is subject to zero-bias if camera ghosting is present during the measurement. The under-prediction of the velocity vectors results in under-prediction of the wake circulation and, consequently, under-prediction of the lift.

2.5 Concluding Remarks

We developed a simple model for the rolled up wake behind a free-flier. The model assumes the wake behind an elliptically loaded wing rolls into a pair of counter-rotating Lamb-Oseen vortices, and provides a method for estimating the PIV parameters necessary to resolve the wake. Trefftz plane velocities in the wake behind typical fliers are typically much smaller than forward flight speed. Consequently, Trefftz plane PIV experiments in wind tunnels suffer from short tracer particle residence times in the illumination volume; hence, the experiments suffer necessarily small interframe times. The limited dynamic range of single-plane PIV with strong out-of-plane flow can be addressed by displacing the laser sheet with the freestream, allowing longer interframe times without the penalty of losing image pairs. We introduced an electro-optical method for switching between laser sheet planes at high speed and high repeatability. The dynamic range of the PIV measurement can be increased by an order of magnitude with the dual-plane approach.

We conducted PIV wake experiments on a fixed wing and studied the vortex strength and behavior. Both techniques measure the same vortex position as a function of downstream distance; however, there is discrepancy between the measured

vortex strengths. The limited dynamic range of traditional PIV measurement in the Trefftz plane makes measurement outside of the trailing vortex core region very challenging because the flow is necessarily very weak compared with the freestream velocity. The interpretation of the spatial distribution of the vortex structures is not restricted, and this is nicely demonstrated by the agreement between the two tested measurements in their measured location of the trailing vortex.

The single-plane technique suffers some important disadvantages to the dual-plane measurements. The dynamic range of this measurement is very small because of the short interframe times permitted by through-plane motion of the seed particles. The actual measurement is barely above the accepted threshold of the resolution of the cross-correlation algorithm. Consequently, the uncertainty of the velocity and velocity-derived quantities (e.g., vorticity) will be an order of magnitude larger in a single-plane measurement as compared to a dual-plane measurement. Additionally, sub-pixel biasing occurs towards integral pixel displacements [64]. The possibility of camera ghosting (noticed in the dual-plane measurements but impossible to identify in the low-displacements of the single plane measurements) may further bias the calculated displacement towards zero. These are systematic errors that lead to under-predicting the velocity field (Figs. 2.7 and 2.9); however, they do not affect the measured spatial vortex structure (Fig. 2.7) or development (Fig. 2.8). The measured vortex profile (Fig. 2.7) shows that vorticity exists well outside the vortex core; therefore, accurate velocity measurements of the outer flow are required to capture the full vortex strength. Fitting a vortex model to the core will inevitably under-predict the full vortex strength because not all of the vorticity rolls into the core.

It should be noted that much of the understanding of the vortex structure in the wakes of bats are derived from measurements which fail to quantitatively explain weight-support Hedenström et al. [7, 8], Hubel et al. [9, 11]. While these authors have acknowledged the under-prediction of weight-support in their data, they proceed to

draw conclusions regarding wake structures from these data sets. One might question the validity of these results; however, this study shows no evidence that the qualitative observations of under-resolved measurements are invalid. While the single-plane experiment failed to predict the load-cell measured lift, there was good agreement in the vortex position during roll-up process with the dual-plane measurement technique. This suggests that despite the quantitative shortcoming of the vortex strength, the conclusions regarding vortex structure are valid.

It is clear that accurate measurement of the vortex strength in the wake requires one to accurately measure the subtle details in the outer flow; it is insufficient simply to measure the maximum velocities at the core edge and then to extrapolate. The dual-plane technique applied allowed an order-of-magnitude increase in the measurement dynamic range, thus allowing the velocities in the outer flow to be accurately captured. This technique can provide a method that can capture the qualitative aspects of the wake structure behind free-fliers—as in previous studies—as well as give quantitative insight to the strength of the wake structures, which previous studies have been challenged to do.

This work was supported by the AFOSR MURI on Bio-inspired flight, monitored by Drs. Doug Smith and Willard Larkin.

Table 2.3: Summary of the PIV experiments

	Freestream, U_∞ [m/s]	Laser thick., h [mm]	Laser disp., Δx [mm]	Interframe time, Δt [μs]	Vol. Ret., V_R [%]	Camera Res., R [pixel/mm]
Single-plane	7.5	2.0	0.0	50	68.4	8.1
Dual-plane	5.0	0.5	2.7	540	100	3.4

CHAPTER 3. The Aerodynamic Cost of Flight in Bats—Comparing Theory with Measurement

Abstract *Aerodynamic theory has long been used to predict the power required for animal flight, but widely used models contain many simplifications. It has been difficult to ascertain how closely biological reality matches model predictions, largely because of the technical challenges of accurately measuring the power expended when an animal flies. We designed a study to measure flight speed-dependent aerodynamic power directly from the kinetic energy contained in the wake of bats flying in a wind tunnel. We compared these measurements to two theoretical predictions that have been employed for several decades in diverse fields of vertebrate biology and to metabolic measurements from a previous study using the same individuals. A high-accuracy displaced laser sheet stereo PIV experimental design measured the wake velocities in the Trefftz plane behind four bats flying over a range of speeds (3–7 m/s). We computed the aerodynamic power contained in the wake using a novel interpolation method and compared these results with the power predicted by Pennycuick's and Rayner's models. The measured aerodynamic power falls between the two theoretical predictions, demonstrating that the models effectively predict the appropriate range of flight*

power, but the models do not accurately predict minimum power or maximum range speeds. Mechanical efficiency—the ratio of aerodynamic power output to metabolic power input—varied from 5.9 *to* 9.8% *for the same individuals, changing with flight speed.*

3.1 Introduction

The evolution of vertebrates capable of flapping flight has produced tremendous diversity in ecology; specialists may hover to extract nectar from flowers, catch insects on the wing, or snatch smaller vertebrates from the ground. Some species migrate thousands of kilometers annually, while others never travel further than a few meters from their roost or nest. The great diversity in flight ecology and behavior is mirrored in a wide range of wing architecture and musculoskeletal structure in bats and birds.

One way in which efforts have long been made to relate wing morphology and motion to flight performance is by understanding flight energetics, and for decades, biologists have tried to estimate the flight power curve, the relationship between aerodynamic energy required for flight and flight speed [e.g., 65]. However, measuring or estimating aerodynamic power of flapping vertebrates is challenging, which necessitates the use of simple models derived from fixed-wing aircraft and helicopter theory. In particular two models, developed by Pennycuick [18] and Rayner [19], have dominated the animal flight literature.

Because of the difficulty in making direct measurements of the aerodynamic power required for animal flight, there has been only one attempt to validate these models [20]. Nevertheless, they have been widely employed to generate diverse predictions, including not only the speed-dependent cost of flight, but also seasonal or life cycle changes in flight behavior, habitat use, migration behavior, and morphological and kinematic scaling [e.g., 66–69].

Both models assume that we can express the total aerodynamic power as the

sum of three subcomponents: induced power, parasite power, and profile power. The induced power, P_{ind}, is the rate of work required to support body weight:

$$P_{\text{ind}} = \frac{2\kappa \cdot (mg)^2}{\pi \rho U b^2} \quad , \tag{3.1}$$

where m is the mass of the animal, g, the acceleration due to gravity, ρ, the air density, b, the wingspan, U, the flight speed and κ, a constant that both the Pennycuick and Rayner models assign a value of 1.2, supported by recent experiments on two nectar-feeding bat species [70].

Parasite power, P_{par}, originates from the drag of the non-lifting parts (i.e., the body) and again, both models have the same functional structure:

$$P_{\text{par}} = \frac{1}{2}\rho S_b C_{D,\text{par}} U^3, \tag{3.2}$$

where the body frontal area $S_b = (8.13 \times 10^{-3}\,\text{m}^2\text{kg}^{-2/3}) \cdot m^{2/3}$, and the parasite drag coefficient $C_{D,\text{par}} = 0.4$.

The profile power, P_{pro}, is associated with the aerodynamic drag of the wings moving through the air. Pennycuick concluded that parasite power remains approximately constant in the mid-range of natural flight speeds [18]:

$$P_{\text{pro}} = 8.4 P_{\text{am}} / \text{Æ} \tag{3.3}$$

where Æ is the aspect ratio of the wing, and P_{am} is the sum of P_{par} and P_{ind} at the minimum power speed. In contrast, Rayner incorporates a drag-based calculation that varies with the cube of the flight speed to estimate the profile power [19, 42]:

$$P_{\text{pro}} = \frac{1}{2}\rho S C_{D,\text{pro}} U^3, \tag{3.4}$$

where S is the wing area and $C_{D,\text{pro}}$ is the coefficient of profile drag, with a typical value of 0.02.

3.1.1 Measurements of the energetic cost of flight

Just as the conservation of momentum dictates that the weight of a flier is supported by imparting equal but opposite momentum to the air in the wake, the conservation of energy dictates that the work done by the flier on the air is reflected in the kinetic energy of the wake. Measurements of animal wakes using Particle Image Velocimetry (PIV) have become common in recent years [e.g., 7, 17, 43]. However, the technical challenges are numerous. For bats and birds whose wings beat at frequencies of approximately 5–16 Hz, high-speed PIV systems capable of time-resolving the flapping cycle are required. Constraints on laser energy and camera resolution limit the size of the measured area, and compromises in experimental design can lead to inaccurate measurements of the vorticity (or circulation) contained in the wake [11, 71]. In the only study that has measured the kinetic energy in the wake of a flying vertebrate [20], the calculated self-energy was less than 60% of the expected value predicted by theory, and the estimated lift was only slightly greater than 50% of that required for weight support. Several other studies have reported that the measured vortex structures contained only 50–60% of the circulation required to support body weight [9, 20, 44, 72–74]. In one study that demonstrated weight support [14], vortex circulation was not computed directly but instead was estimated by thresholding the measured vorticity below a cut-off value and then extrapolated outside the vortices using an assumed Gaussian tail to the vorticity distribution. This assumption may not represent the actual circulation profile [71]. Other studies have used a variety of ad hoc assumptions and explanations to account for the missing lift [7, 8, 11]. Recently, a novel PIV method (dual-plane illumination) was developed and used to capture the complete circulation in the wake and to identify the sources of previous

difficulties associated with this challenging measurement [71].

3.1.2 Metabolic cost of flight and efficiency

Another approach to estimating the cost of animal flight is to measure metabolic energy used and thus estimate power input, rather than power output. Metabolic power can be measured directly from flying animals using a variety of techniques, including respirometry (open flow or closed system), isotope labeling techniques (doubly-labeled water or the sodium-bicarbonate method), and heat transfer modeling [75]. If both metabolic power input and aerodynamic power output can be measured, it is possible to estimate flight efficiency η, the ratio of metabolic and aerodynamic power of flight. Efficiency is notoriously difficult to measure empirically and hence not well understood for animal flight or even for terrestrial or aquatic locomotion. Estimates for efficiency during flight obtained using diverse techniques range between 3 and 33% for birds [76] and between 5 and 30% for bats [e.g., 77–79]. Flight efficiency may vary with body mass both among and within species, and some evidence has suggested it may change with flight speed [e.g., 80].

3.1.3 Current work

Here we report on a series of experiments designed to measure the aerodynamic power of Seba's short-tailed bats, *Carollia perspicillata*, flying in a wind tunnel. We compare these measurements with values predicted using the prevailing theories and estimate the energetic efficiency of bat flight over a range of flight speeds. We estimate the cost of flight from wake velocity measurements using an approach that is novel in several ways. First, we employ dual-plane, three velocity-component PIV, which enables high accuracy velocity measurements in the Trefftz plane and which captures all of the wake vorticity, without the need for corrections [71]. Second, we describe and apply an analytical method, the Helmholtz-Hodge decomposition, with which we can

accurately estimate the energetically significant wake velocity outside the measurement zone. The Helmholtz-Hodge decomposition allows us to accurately calculate the total aerodynamic power. Finally, we combine the measurements of flight power with previous measurements of metabolic power, made in the same facility, from the same individuals [81], to test the hypothesis that flight efficiency is flight-speed dependent.

3.2 Materials and Methods

3.2.1 Wind tunnel

Four non-reproductive Seba's short-tailed bats (*Carollia perspicillata*) were flown in the closed-loop, low-turbulence wind tunnel at the School of Engineering at Brown University. The test section is 3.8 m long and has a cross section of 0.60 x 0.82 m, relative to a mean wingspan of 0.28 m of the experimental animals. More details of the facility are reported by Hubel et al. [9]. Experiments were conducted at free stream velocities from 1 to 6 m/s, measured with a pitot tube and differential pressure transducer (Setra Model 239). True forward flight speed was determined to be the sum of the freestream and the animal's velocity relative to the lab frame. Wind tunnel temperature was monitored with a thermistor probe and digital controller (Omega DP25-TH) and was 21.3 $\pm$ 0.6°C (mean $\pm$ one standard deviation) during experiments. The atmospheric pressure was monitored by an absolute pressure transducer (Setra Model 270) and averaged 101.0 $\pm$ 0.9 kPa (mean $\pm$ one standard deviation). The animals were released into the wind tunnel and trained to fly through a hole in a net, emerging in the correct position within the test section such that forward flight would take the bats through the PIV and kinematic interrogation areas and the laser. The laser was triggered after the bats passed through the plane of the laser sheet so as to prevent direct exposure of the animals to any laser light. A right-handed coordinate system was defined with the x-axis aligned with the direction of the flow, the y-axis transverse to the flow, and the z-axis vertical.

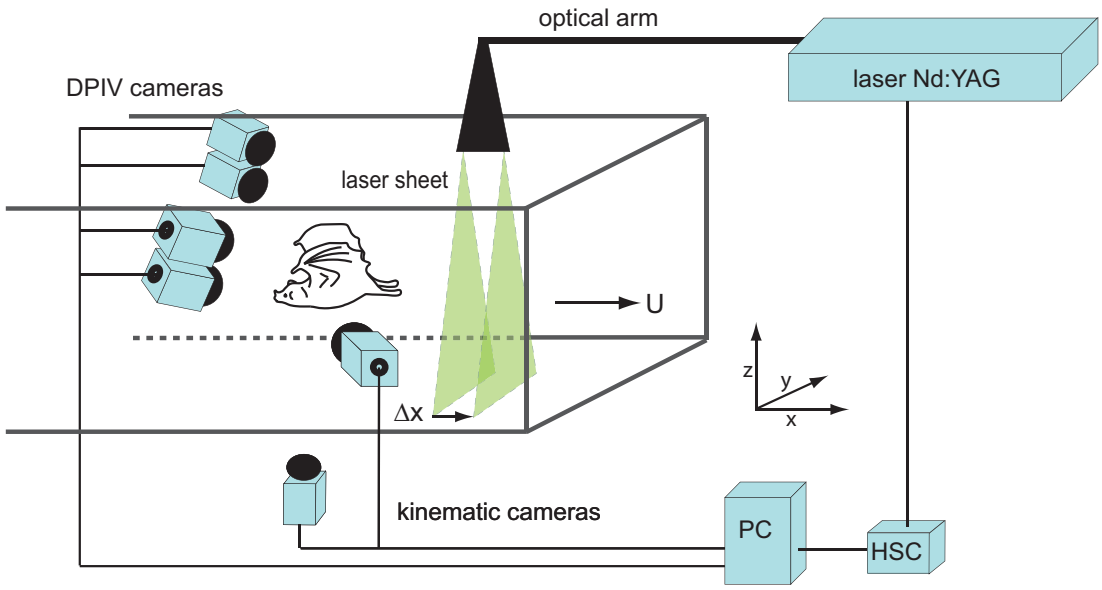

Figure 3.1: Experimental setup, illustrating dual-plane, double stereo PIV in the Trefftz plane. Four PIV cameras area used along with two kinematics cameras.

3.2.2 PIV measurement

The PIV experiment was controlled using commercial PIV software (DaVis v8). The image pairs were captured with four high-speed cameras (three Photron FASTCAM SA3 and one Photron FASTCAM SA5) using a 105 mm f/2.8D, a 60 mm f/2.8D, and two 85 mm f/1.4D Nikkor lenses on Scheimpflug mounts. Optical bandpass filters of 531 $\pm$ 22 nm were used to minimize stray light. The four cameras were arranged into two stereo pairs with fields-of-view stacked vertically to give an increased measurement region. The resulting combined field-of-view was approximately 22.7 $\times$ 31.1 cm^2 with a resolution of R = 4.5 pixel/mm. The cameras were calibrated using a LaVision Type 31 calibration target and the software's stereo camera calibration routine. Laser sheet illumination (532 nm) was provided by a double-pulsed 200 Hz, 50 mJ laser (Litron LPY-732). The wind tunnel was filled with 1 μm droplets of Di(2-ethylhexyl)sebacate (DEHS) generated using a Laskin nozzle. Image pairs were

captured in the Trefftz plane (y, z) behind the flying animal. At lower wind speeds (1-3 m/s), where wake structures are of comparable strength to the freestream, we used single-plane stereo PIV. At higher wind speeds (4-6m/s), we used a dual-plane PIV measurement system [71] (Table 3.1, Fig 3.1). PIV images were processed in DaVis, and cross-correlation was performed on a GPU using a multi-pass algorithm. Analysis used two initial passes with a 128 $\times$ 128 pixel^2 rectangular window and three passes with a final 64 $\times$ 64 pixel^2 Gaussian-weighted window and a window overlap of 75%, corresponding to a vector spacing of 3.7 mm with an equivalent independent vector spacing of 7.4 mm [82]. The resulting three component velocity fields, $\mathbf{u} = (u, v, w)$, were imported into a custom Matlab® analysis program (Matlab® R2011b, The MathWorks Inc., Natick, MA, USA) analysis program, where images from the upper and lower regions were stitched together into a composite vector field. The wake vorticity was computed from the measured velocity field using finite differences. Only PIV trials that captured the entire vorticity within our measurement region during a complete wingbeat cycle were included in the analysis. We analyzed a total of 75 trials: 2, 3, 13, 18, and 38 wingbeats at flight speeds of 3, 4, 5, 6, and 7 m/s, respectively. Since we only analyzed level flights with zero roll, we assumed sagittal plane symmetry and mirrored the wake measurements about the median plane of the animal.

3.2.3 Kinematics measurement

Bat kinematics were recorded synchronously with the PIV to enable spatial registration of the bat position and wake structures. Bats were filmed in ventral (x, y) and lateral (x, z) view at 400 Hz with a pair of high-speed cameras (Photron FASTCAM1024) (Fig. 3.1). Position of the body, defined as the midpoint between the legs (the coccyx) and wrist were digitized in both views and transformed into three-dimensional coordinates by direct linear transformation (DLT) using a custom track-

Table 3.1: Summary of the PIV experimental parameters

	free stream, U_∞ [m/s]	Laser thick., h [mm]	Laser disp., Δx [mm]	Inter-frame time, Δt [μs]	Vol. Ret., V_R [%]	Camera Res., R [pixel/mm]
Single-plane	1–3	3.0	0.0	505–167	71	4.0
Dual-plane	4–6	0.5	2.7	675–450	100	4.0

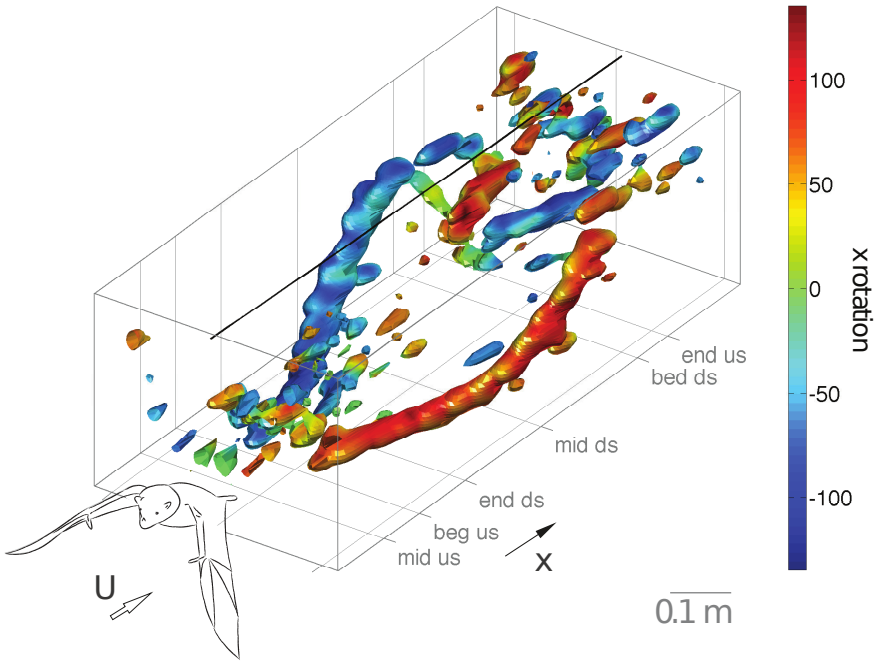

Figure 3.2: The stitched and mirrored PIV data are "stacked" to create a pseudo-volumetric wake, here for trial at 6 m/s. Free stream and PIV acquisition frequency used to assign streamwise spacing between successive PIV frames: $h_x = U_\infty / f_{\mathrm{PIV}}$. end us: end of upstroke; beg ds: beginning of the downstroke; mid ds: mid downstroke; end ds: end of downstroke; beg us: beginning of upstroke; mid us: mid upstroke. The q-criterion isosurfaces are colored by the local x vorticity.

ing routine [83]. The 3-dimensional marker locations were exported to MATLAB® and transformed to the PIV coordinate system for analysis. The bat's velocity relative to the PIV coordinate system was measured using a linear least-squares fit of body position versus time. Wingbeat frequency was calculated by fitting a sinusoid to vertical wrist position. Each PIV frame was assigned a wingbeat phase by adjusting the phase of the concurrent kinematic frame by the upstream position of the bat and the freestream.

3.3 Results

3.3.1 Wake structure

We quantified the wake structure in the Trefftz plane behind four Seba's short-tailed bats (*Carollia perspicillata*) flying freely in a wind tunnel at flight speeds of $U_\infty = 3$–$7\,\mathrm{m/s}$. The vortex structure of the wake (Fig. 3.2 and Fig. 3.3) is consistent with previous studies [7–9, 11, 14, 15, 84, 85]. We find a strong tip vortex at the beginning of the downstroke that persists until mid-upstroke (Fig. 3.3a,b), a wing root vortex that is observed at the beginning of downstroke (Fig. 3.3a), and a reversed vortex loop at the end of upstroke (Fig. 3.3c). The velocity fields (Fig. 3.3d–f) show a velocity deficit associated with the vortex core during the beginning of the downstroke. However, this changes to a wake velocity surplus by the end of downstroke. The velocity field extends over a far greater area than the vorticity field and well beyond the measurement area (Fig. 3.3g–i).

3.3.2 Lift

The wingbeat-averaged lift, L, can be calculated from the wake vorticity ω:

$$L = \frac{\rho U_\infty}{T} \int_{\mathrm{wb}} \int_{\mathrm{Trefftz}} y \cdot \omega \; dA \; dt \tag{3.5}$$

where the subscript "wb" denotes integration over a wingbeat cycle, and T is the wingbeat period. We calculated lift-to-weight ratio as a function of flight speed for each of 75 wingbeats using the appropriate average weight for each individual (Fig. 3.4). At higher speeds, the average of the measured lift equals weight with no additional assumptions (mean $L/W = 1.02 \pm 0.15$ std). At lower speeds, where we did not employ the dual-plane PIV method, the measured lift was less than weight (mean $L/W = 0.83 \pm 0.05$ std).

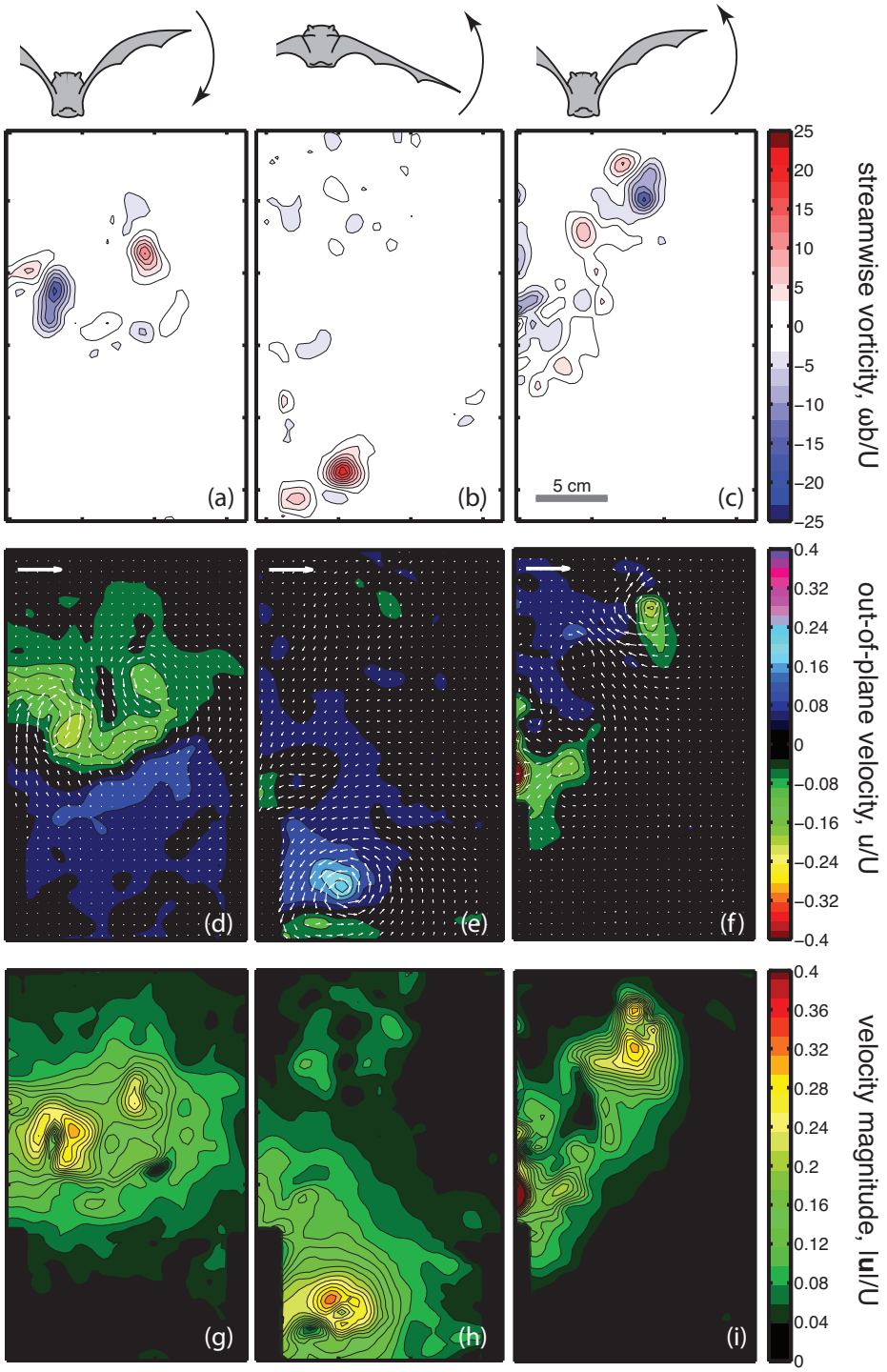

Figure 3.3: Out-of-plane (streamwise) vorticity field (a,b,c), velocity field (d,e,f), and velocity magnitude (g,h,i) contours for beginning of downstroke (a,d,g), end of downstroke (b,e,h), and end of upstroke (c,f,i)

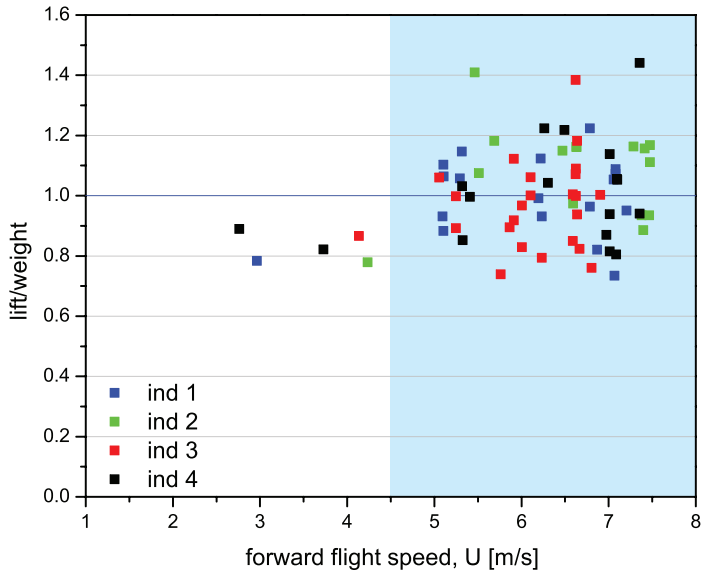

Figure 3.4: Lift-to-weight ratio versus forward flight speed for four individuals; blue background indicates use of dual-plane PIV method.

3.3.3 Aerodynamic power

Aerodynamic power was computed by measuring the total kinetic energy in the wake. In the absence of flight, we observe only wind tunnel freestream flow, and any difference between the wake velocity field and the undisturbed freestream derives from energy put into the wake by the bat. By measuring the wake velocities using PIV, we can simply integrate the wake energy to find the aerodynamic power. As noted above, velocity magnitude contours (Figs. 3.3g–i) indicate that nonzero wake velocities lie beyond the measured region; thus, a simple wake integration of the measured velocities will underestimate the power. However, since we have measured all of the wake vorticity (Fig. 3.3a–c), the velocity outside the measurement area can be uniquely calculated using an exact extrapolation technique based on the Helmholtz-Hodge decomposition [86]—a vector calculus theorem from nineteenth-century mathematical physics. Given a vorticity field and assuming incompressible flow, we can use the Helmholtz-Hodge decomposition to extend the wake velocity field (without approximation) to include the entire wind tunnel test section, and with this we obtain a

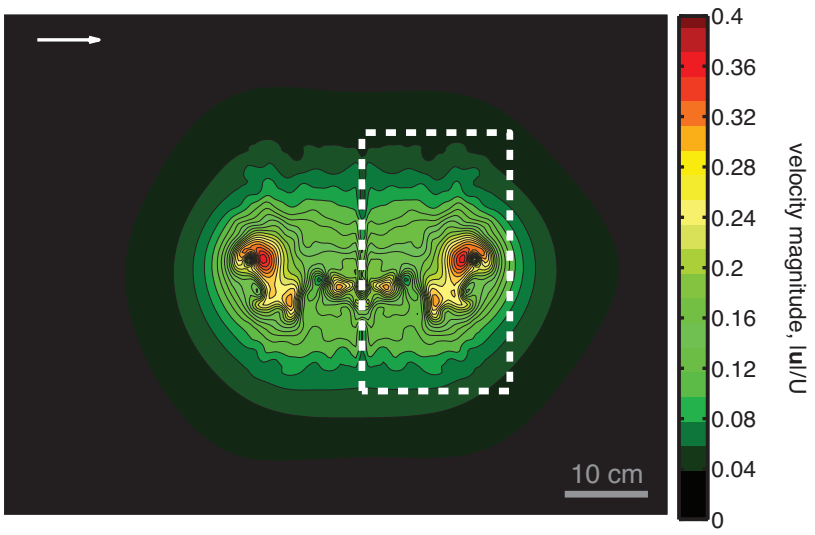

Figure 3.5: Typical contour of the wake velocity magnitude measured behind the bat over entire wind tunnel region. White dotted line depicts the measurement area over which wake velocities were measured using PIV. The complete wake velocity field is achieved by reflecting the measurements about the meridional plane of the bat and extending them beyond the measurement region by means of the Helmholtz-Hodge decomposition.

much more complete measurement of the aerodynamic power (see Appendix B and Fig. 3.5).

The total kinetic energy of a wingbeat was calculated from the extended velocity field,

$$E_{\mathrm{wb}} = \int_{\mathrm{wb}} \frac{1}{2}\rho|\mathbf{u}|^2\, dV. \tag{3.6}$$

and subsequently, the average aerodynamic power was calculated by multiplication with the wingbeat frequency, f_{wb}, as $P_{\mathrm{wb}} = E_{\mathrm{wb}} \cdot f_{\mathrm{wb}}$. The measured aerodynamic power falls between the two theoretical predictions (Fig. 3.6); Pennycuick's model shows higher, while Rayner's model shows lower values compared to our measurements (Fig 3.6). Aerodynamic power increases with speed (energy at 7 m/s is significantly greater than that at either 5 or 6 m/s; Student's t-test, $p = 0.0067$).

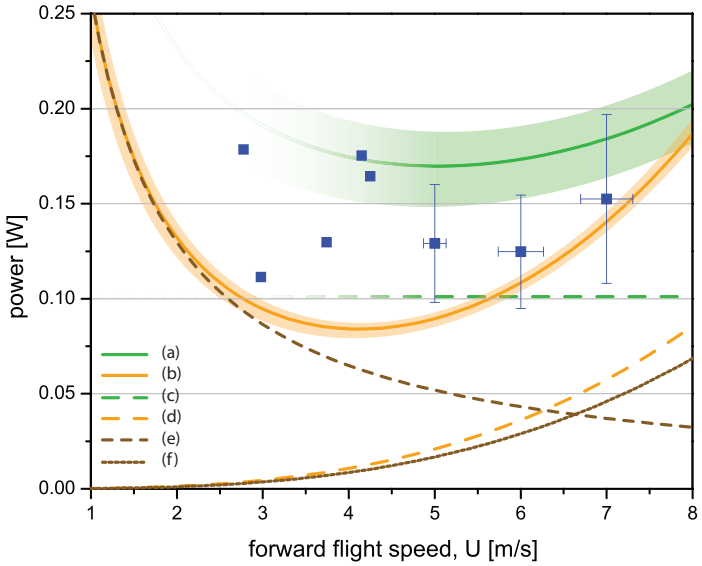

Figure 3.6: Aerodynamic power (Watts) from PIV measurement (blue; y-error bars are ± standard deviation of power, x-error bars are ± standard deviation of speed) and power predictions based on Pennycuick [18] (green) and Rayner [19] (orange) vs. flight speed. With the exception of the five wingbeats at the lowest speeds, the data are binned to nearest integer [m/s] flight speeds. Induced and parasite power (e and f) are estimated in the same way in the two models, but profile power (c and d) and total power (a and b) differ between Pennycuick's (a and c) and Rayner's (b and d) models. The uncertainty in total power prediction due to variation among study subjects in input parameters (body mass, wingspan, wing area) is indicated by shading around the solid green and orange lines. Pennycuick's model is only valid for flight speeds between minimum power and maximum range speed, indicated by the fading curves.

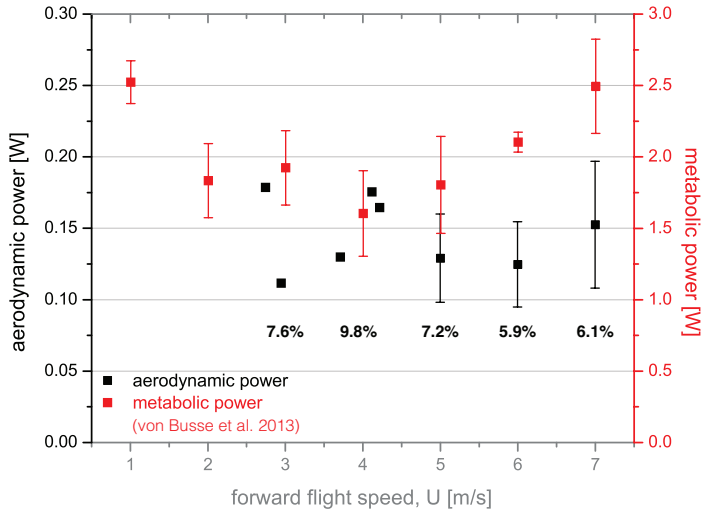

Figure 3.7: Aerodynamic power output (black, left y-axis) and metabolic power input (red, right y-axis) vs flight speed (metabolic data measured with Na-bicarbonate method from von Busse et al. [81]). Metabolic power measured over 1 to 7 m/s (median ± absolute deviation); aerodynamic power from 3 to 7 m/s (average ± standard deviation, where applicable). Percentages below symbols are mechanical efficiency (aerodynamic power/metabolic power).

3.3.4 Mechanical efficiency of flight

In a prior study, using the ^{13}C labeled Na-bicarbonate method [87], the same individuals in the same wind tunnel were found to exhibit a U-shaped dependence of metabolic power over speeds ranging from 1–7 m/s [81]. The ratio of aerodynamic power to metabolic power yields the mechanical efficiency of locomotion, η (Fig. 3.7). Our measurements of both parameters from multiple individuals allow estimates of efficiency at flight speeds between 3–7 m/s, and over this range η varies from 5.9% at 6 m/s to 9.8% at 4 m/s.

3.4 Discussion

Dual-plane PIV measurements and the Helmholtz-Hodge decomposition analysis have allowed us to calculate the aerodynamic power expended by bats in free flight and make comparisons with the leading aerodynamic theories. There are inherent challenges associated with both measurement and theory. Theoretical predictions are

sensitive to model uncertainties [88], while experimental estimates are sensitive to measurement accuracy.

At flight speeds above 4.5 m/s, we recover full weight support without any data corrections. There is, of course, scatter about the mean, but this scatter is expected given the fact that each point represents an individual wing beat. Using single-plane PIV at lower speeds, however, we only recover 80% of the lift. The low-speed data should be viewed with caution. First, at these lower speeds, it is difficult to obtain PIV measurements of complete wingbeats at low wind tunnel speeds; animals often prefer to fly through the measurement volume at a higher net airspeed or fly in an unsteady manner. Consequently, the low-speed results are based on only five wingbeats. Second, PIV measurement uncertainty is inversely proportional to the time between laser pulses [71]; thus, our highest uncertainty occurs at low freestream velocities (Table 3.1). Third, for our calculations to be valid, we assume that the freestream dominates the streamwise velocity fluctuations in the wake. However, this assumption breaks down at low flight speeds, where streamwise wake structures increase in strength relative to the freestream, and the relative importance of wind tunnel flow inhomogeneities and free stream turbulence increases. Nevertheless, there is no reason to exclude the data from low-speed flights, and we present them for completeness.

3.4.1 Measurement accuracy

The methodology described here makes two important contributions towards minimizing error. First, we measure all three components of velocity. The streamwise velocity component, u, has regions of both surplus and deficit (Fig. 3.3d–f), and if it were ignored, the energy would be underestimated by over 20% (Table 3.2). Second, the Helmholtz-Hodge decomposition, and the subsequent interpolation of the velocity field throughout the full wind tunnel test section, ensures that all of the energy in

the wake, including that falling outside the measurement field-of-view, is included in the energy budget. This "exterior" flow contains roughly 8% of the total energy budget (Table 3.2), thus a power estimate from only the directly measured region (e.g., Fig. 3.3) systematically underestimates the total aerodynamic power.

Table 3.2: Percentage of total aerodynamic power obtained using (i) two-component PIV with a single camera (only v, w components), or (ii) stereo PIV without using the Helmholtz-Hodge decomposition to interpolate the wake velocities beyond the experimental field-of-view.

Flight speed [m/s]	3	4	5	6	7
Single camera PIV [%]	75	83	81	77	73
Experimental field-of-view only [%]	92	92	91	92	93

Analysis of tomographic PIV-based volumetric reconstructions of locust wakes has highlighted several issues that may arise when representing the wake as a pseudo-volume reconstructed from a time-series of planar measurements [17]. In particular, the assumption that the wake is uniformly advected by the freestream can lead to two sources of error: (i) flow structures smaller than the spacing between successive measurements may not be detected, and (ii) wakes may undergo substantial deformation [17]. We evaluated the possibility that these phenomena could play a significant role in our results. In the present case, we seek to quantify the linear momentum and energy content of wakes. Conservation of energy ensures that the properties we measure at the interrogation plane are conserved as they advect, despite any possible distortion. The energy in the wake is contained in its large-scale structure (Fig. 3.8), thus the smallest scale details that may be undetected between successive measurements are also the least energetically significant. We also note that viscosity dissipates kinetic energy from the viscous length scales, $\sqrt{\nu t}$. Here, ν is the viscosity of air, t is the period of a wingbeat, and viscous length is approximately 1.4 mm, which is smaller than the vector spacing of our PIV measurement. Viscosity critically affects the energy content of a pigeon wake only after approximately 2.7×10^3 s [20], and

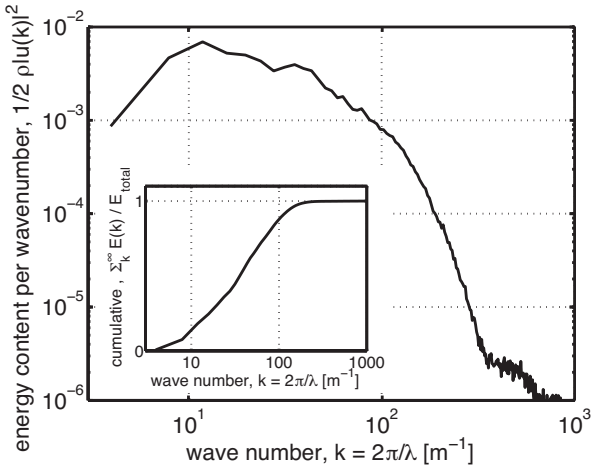

Figure 3.8: Wake kinetic energy per wavenumber from the wingbeat shown in Fig. 3.5. The bulk of the wake energy is contained in large-scale flow structures. The inset shows the fraction of the energy contained in the first k wavenumbers. For wavenumbers $k \leqslant 100$ m^{-1}, the error is less than 10%; hence, 90% of the wake energy is contained in flow structures larger than 6.3 cm.

given that the wingbeat period for *Carollia perspicillata* is even shorter than that of a pigeon, we can safely neglect the effects of viscosity. Furthermore, the far-field influence of these structures depends only on the total strength of these conserved quantities and not on the fine detail of their localized configuration. A discussion of wake deformation can be found in Appendix A.

3.4.2 Uncertainty in theoretical models

The magnitude of aerodynamic power measured falls between the predictions of the two most commonly used models for vertebrate flight energetics, those of Pennycuick [18] and Rayner [19] (Fig. 3.6). These models differ in their calculation of profile power. Pennycuick's assumption for the estimation of profile power is only valid between the minimum power and maximum range speed, in our case from around 5.0–8.5 m/s. Given the complex flow generated by flapping flight of compliant, highly articulated wings and the relative simplicity of the models, it is not surprising that the exact form of the predicted and observed power curves differ. Moreover, val-

ues for minimum power and maximum range speeds estimated by these models are very sensitive to the values of the input parameters. For example, the variation in wingspan, wing area, and body mass among the individuals in this study produces a range of predicted values for minimum power speed from 4.9–5.1 m/s using Pennycuick's model (see Fig. 3.6). However, due to the uncertainty in the predicted power curve the power cost at these minimum power speeds does not differ from the possible values of power cost between 3 and 7 m/s. Therefore, energetically, those speeds are not distinguishable from the minimum power speed. This broad range of speeds encompasses nearly the entire range of velocities tested in our study and suggests that defining a minimum power speed may be of little practical relevance. This uncertainty is often not recognized but may have significant implications where computations of minimum power speeds are used, for example, in modeling migration, predicting foraging behavior, etc. [67, 68, 89–91].

3.4.3 Flight efficiency

In previous studies of mechanical efficiency, estimates have been obtained by comparing metabolic power, usually measured by respirometry, to aerodynamic power, often calculated from Pennycuick's model [77, 80, 92–94]. These studies have yielded efficiency estimates that range between 12–40%. The estimates of mechanical efficiency we report here, using, for the first time, experimental measurements for both metabolic and aerodynamic power, ranged from 5.6–11.3%. Those values are at the low end of the recorded range for flying vertebrates and overlap with values reported for hovering in glossophagine bats and hummingbirds [79]. However, we note that previously reported values estimated aerodynamic power from Pennycuick's model and did not quantify power directly. Our empirical measurement of flight power demonstrates that Pennycuick's power curve, which makes a number of simplifying assumptions, overestimates aerodynamic power, particularly at intermediate flight

speeds (Fig. 3.6), which leads to artificially inflated estimates of mechanical efficiency. Additionally, our data suggest an increase of aerodynamic power with the observed lift, indicating a potential underestimation of our power estimates at low flight speeds (Fig. 3.4), which would lead to an increased mechanical efficiency at low speeds.

Although flight energetics models typically assume constant efficiency, it has been suggested previously that mechanical efficiency may vary as a function of flight speed in flying vertebrates and that this variation could depend on the ecology and flight specialization of a particular species [95]. Our results for *Carollia perspicillata* support the idea that efficiency can be flight-speed dependent. At present, it is impossible to know whether this is a general feature of bats or a trait that characterizes this species; mainly feeding on nectar and fruit, these bats are not specialized to hunt insects on the wing, nor are they known as particularly fast fliers. High efficiency at low-to-intermediate flight speeds could be particularly beneficial for animals with this kind of feeding ecology, but only comparisons with other, divergently specialized species can test this hypothesis.

3.5 Concluding Remarks

We present here a sophisticated yet tractable method to calculate aerodynamic power from the wake behind a flying animal. It is critically important that the measurement recovers lift, contains all three velocity components, and accounts for the extended spatial area that the wake energy occupies. The measured flight power does not show a clear U-shaped relationship with speed, although the difficulties associated with acquiring data at low speeds could affect this conclusion. Our aerodynamic power measurements are bracketed by the two most widely-used theories for estimating aerodynamic power, which confirms the utility and power of those relatively simple models. Nevertheless, the models' weak dependency on speed and the uncertainties associated with determining basic parameters such as wingspan and weight, reinforce

the caution that must be taken when applying such theories. We document a decline in mechanical efficiency at higher flight speeds, which appears to arise primarily from the increased metabolic power requirements of flight at these speeds.

The authors thank M. L. Hedberg and E. Giblin for their help during the experiments, C. Chan, for digitizing and Dr. G. Paul-Leyson and N. Trask for their discussions on wake energy calculations. All components of this study were approved by the Institutional Animal Care and Use Committee at Brown University. Financial support was provided by the Air Force Office of Scientific Research (AFOSR MURI) on Bio-inspired Flight, monitored by Drs. D. Smith and W. Larkin.

CHAPTER 4. Shape, Lift, and Vibrations of Highly Compliant Membrane Wings

Abstract *Membrane wings are common in flying animals such as bats, lemurs, flying squirrels, and pterosaurs, as well as in low Reynolds number Micro Air Vehicles. Vortices shed from the sharp leading and trailing edges and wing tips of membrane wings, and the vortex interactions with the membrane play an important role in the wing's performance. With compliant membrane wings that are initially tension-free at rest, there are two issues to consider: (a) the static relationship between the net aerodynamic forces and the bulk wing deformation, and (b) the interaction between the membrane dynamics and unsteady flow structures. We present a simple model of the finite deformation and natural frequency of an initially tension-free membrane wing, which depends only on an aeroelastic parameter. We extend our theory with a computer model that accounts for nonuniform chordwise load. We conduct experiments on low aspect ratio membrane wings with different support structures and thicknesses, over a broad range of freestream velocities and angles of attack. We measure wing shape and dynamics, aerodynamic force, and the wake, and find good agreement between the experimental results, the computer model, and our theoretical*

model. Membrane deformation affects the membrane vibration modes, which in turn affects the coupling between the membrane and vortex shedding. Wings with different wing tip support, but similar stiffness show similar static behavior, but exhibit markedly different dynamic behavior.

4.1 Introduction

Membrane wings are characteristic of flying animals such as bats, lemurs, flying squirrels, and pterosaurs as well as in low Reynolds number ($Re < 10^5$) Micro Air Vehicles (MAVs). These wings exhibit interesting features such as self-cambering, soft stall, and enhanced performance at large angles of incidence [30]. Furthermore, these wings operate in a parameter space where complex phenomena such as flow separation and reattachment, and the unsteady interactions between the elastic and vortical structures over the wings may critically affect the wing's aerodynamic performance. In the literature, the modeling of elastic membrane wings has evolved from work on the aeromechanics of inextensible sails [96, 97], where the shape of the sail is determined by the requirement that each element of the sail is in mechanical equilibrium with fluid stresses, and the fluid stresses in turn depend on the sail shape. In this case, the tension in the sail acts as a Lagrange multiplier to satisfy the inextensibility constraint [98]. Membrane elasticity complicates the problem because the tension must be related to the stretch of the deformed membrane, which manifests itself as an additional equation for the elastic stress. The forces on the membrane result from fluid forcing; therefore, an appropriate model for the fluid is required. In the literature, the general approach to modeling membrane wings is to state an equation of motion for the membrane, state a fluid-dynamical regime of operation (e.g., two-dimensional steady laminar flow, turbulent flow, three-dimensional unsteady, etc...), and then to solve the problem numerically by coupling a structural solver to a fluid dynamical solver [25, 27–29, 99, 100].

As an example, Smith and Shyy [25] modeled the membrane airfoil as a two dimensional linear elastic membrane governed by the Young-Laplace equation. In their calculations, they assigned the membrane with a large modulus—sufficiently large to make the wing approximately inextensible—and excess length, and coupled the membrane solver with a Reynolds-averaged Navier–Stokes solver to compute equilibrium two-dimensional configurations for the sail-like wing. Their calculations showed that inviscid wing theory provides a reasonably accurate description for small angles of attack and only for small excess length.

Elastic membrane wings present an additional challenge, because the tension and length of the wing change with the aerodynamic load. Whereas inextensible sails have a fixed excess length, elastic membranes may initially have zero excess length or even pretension, and may still adopt a camber under aerodynamic load. Experiments by Song et al. [30] examined elastic membrane wings with leading and trailing edge support and demonstrated enhanced lift and delayed stall compared to a rigid flat plate, albeit at the expense of increased drag. The self-cambering of the compliant wing allows positive lift to be sustained even at small negative angles of attack. Furthermore, Gordnier's [27] high-fidelity simulations of membrane wings show that compliance allows positive average lift to be maintained at zero angle of attack. Experiments on wings with free trailing edges passively change their angle of attack in response to flow conditions [31, 36]. Changes in the Reynolds number lead to changes in the boundary layer thickness and stability [27], which affects the pressure distribution on the wing. Experimentally, it is difficult to independently vary Reynolds number and effective membrane elasticity because both depend on the freestream velocity.

Membrane dynamics also play an important role in the behavior of membrane wings [27, 30, 32, 33, 36]. Membrane wings may exhibit standing mode vibrations near integer multiples of the membrane fundamental frequency [27, 30, 32, 33], or they may exhibit traveling wave characteristics [27, 36]. The unsteady motions of

the membrane lead to smaller separated regions over the membrane wing than on identically shaped rigid wings [27, 32]. Membrane dynamics vary greatly with the membrane pretension or excess length [30, 33], with the character of the membrane supports [31, 35, 36, 101], and with the Reynolds number [27]. The natural modes in the membrane and supports may interact with the natural modes in wake to select the particular mode of vibration and vortex shedding.

Despite the experimental and computational work on compliant membrane wings, relatively little effort has been spent on simple analytical descriptions that can provide valuable insight as well as leading order predictions. Song et al. [30] developed a model for membrane wing behavior by neglecting the complexities of chordwise load distributions and assuming that a two-dimensional membrane was subjected to a uniformly distributed load. Linear membrane behavior yields a parabolic shape; therefore, the relationship between the membrane deflection and the force can be simply stated. The resulting description of the membrane wing is a statement of equilibrium in the final membrane configuration and is governed by a "Weber" number,

$$We = \frac{L}{Ehs}, \tag{4.1}$$

which relates the aerodynamic forces on the wing (e.g., the lift), L, and the surface force (e.g., membrane tension), characterized by the membrane modulus, E, thickness, h, and span, s. Despite it's simplicity, this theory compares favorably with experimental data. However, the model is not predictive because the aerodynamic load, L, must be specified. Furthermore, the wing loading depends on the camber, which in turn depends on the wing loading. Clearly, a relationship that provides camber as a function of aerodynamic loading is needed to provide a complete model of the wing behavior.

Furthermore, modeling membrane wings without pretension presents mathemat-

ical difficulties because the wing exhibits infinite compliance for small deformation; hence, nonlinear geometry changes must be incorporated in the model of the aerodynamic response. Stanford and Ifju [101] investigated the accuracy of linear and nonlinear membrane models applied to perimeter-supported circular membranes subject to uniform load. They compared experimental measurements to different membrane models and found that membranes without pretension require geometrically nonlinear models and may also require the use of nonlinear material effects when subjected to very large load.

To address the shortcomings of the current analytical framework, we expand upon the model given by Song et al. [30] by adding a simple aerodynamic model for the lift which accounts for self-camber (Sec. 4.2). The resulting theory provides a simple but complete description of the static fluid-structure interaction. The model allows the static behavior of the wing to be estimated, given a proposed set of aerodynamic parameters (e.g., freestream velocity and angle of attack). Our model continues to use the assumption that the membrane is subject to uniform aerodynamic loading. To assess the validity of this assumption, we compare our results with a numerical model (Sec. 4.3) that uses the true aerodynamic load to calculate the membrane shape. Finally, we compare our results with wind tunnel experiments (Sec. 4.4) conducted using low aspect ratio wings with two types of wing tip support. The unsteady motion of the wing is also examined and the predictions of the analytical theory are compared with the experimental observations in Sec. 4.5.

4.2 Theoretical Considerations

Song et al. [30] provided a simple theory for the static behavior of membranes subject to uniform aerodynamic load in which the membrane camber is determined by the total force on the membrane. Fig. 4.1 illustrates the two-dimensional membrane wing problem. Because the deformed shape is determined via the uniform load assumption,

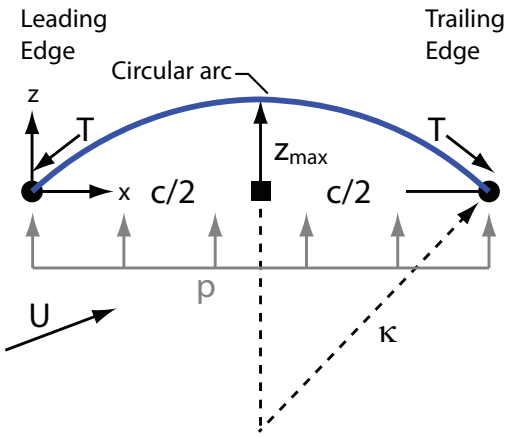

Figure 4.1: The two-dimensional membrane wing of chord, c, under aerodynamic load. The tension, T, and the curvature, κ, balance the normal aerodynamic load, p. Under the assumption of uniform load, $p(x) = const$, the solution to the Young-Laplace equation governing the membrane shape is given by a circular arc segment, in which case the curvature is given entirely by the membrane camber, z_{max}.

geometric nonlinearity is accounted for with an analytical expression for the membrane tension in the deformed configuration, and camber is determined by making a statement of force equilibrium between the membrane and aerodynamic forces in the deformed configuration. However, the interesting feature of membrane wings is that the aerodynamic forces are influenced by the membrane shape, and the description given by Song et al. [30] fails to address the coupled nature of the fluid-structure interaction. To address the coupled fluid-structure problem of the membrane wing, we add an aerodynamic model to the membrane model established by Song et al. [30] that relates the aerodynamic force to the wing shape.

4.2.1 Static wing configuration

The static equilibrium shape of a membrane under a pressure load is governed by the steady-state Young-Laplace equation,

$$\kappa + \frac{p}{T} = 0. \tag{4.2}$$

Here, the local membrane curvature κ balances the pressure load p divided by tension, T. Previous works have used the Young-Laplace model for static [25] and dynamic [27] simulations. For a spatially uniform load, the Young-Laplace equation states that the curvature is everywhere constant; hence, the equilibrium shape is a circular arc. When the Young-Laplace equation is linearized for small deformations, the curvature term is replaced by a second derivative term, resulting in the Poisson equation,

$$\nabla^2 z + \frac{p}{T} = 0. \tag{4.3}$$

For a spatially uniform load, the Poisson equation states that the second derivative of the membrane deflection is constant; thus, the solution defines a parabolic membrane shape. The Poisson equation was used by Song et al. [30] to formulate their membrane model.

In the case of an initially tension-free elastic membrane, the pressure term, p/T, is singular and the membrane is infinitely compliant; hence, nonlinear geometry changes must be considered. The governing equation for the membrane shape should be interpreted as a statement of equilibrium in the *deformed* configuration and should remain valid in the presence of large deformations. We proceed with the more general Young-Laplace membrane model for our analysis; however, the difference between the Young-Laplace and Poisson models is minor (as we will see). We maintain the uniform-load simplification used by Song et al., which leads to the circular arc membrane shapes. Under this assumption, the deformed membrane configuration is uniquely defined by its maximum camber, $z_{\max}$. For convenience, we normalize the camber by the wing chord, $z^* = z_{\max}/c$. We can write the expression for the chord-normalized curvature of the wing, κ^*, from the normalized camber,

$$\kappa^* = \frac{8z^*}{1 + 4z^{*2}}. \tag{4.4}$$

The membrane tension in the deformed configuration is given by the appropriate material constitutive behavior. For simplicity, we use a plane-stress linear elastic description for the membrane with a Young's modulus, E, a thickness, h, and a prestretch, λ_0, in which case the tension is given as,

$$T = Eh(\lambda - 1), \tag{4.5}$$

where the chordwise stretch, λ, is the ratio of the total length of the deformed segment to the chord length. The stretch is determined by the geometry of a circular arc with camber z^* (Fig. 4.1):

$$\lambda = \lambda_0 \frac{1 + 4z^{*2}}{4z^*} \arcsin\left(\frac{4z^*}{1 + 4z^{*2}}\right). \tag{4.6}$$

It should be noted that any suitable constitutive model for the membrane material can be used. If very large deformations need to be modeled, then a nonlinear material response may be required [101].

To complete the model, we need a description of aerodynamic behavior of a circular arc segment. Circular arcs are a subfamily of Joukowski airfoils whose aerodynamic response is easily written [50]; therefore, the Joukowski airfoil solution is the obvious choice for a simple relationship for the membrane load in its deformed configuration:

$$p = \frac{1}{2}\rho U^2 C_L, \tag{4.7}$$

$$C_L = 2\pi \sin\left(\alpha + \frac{1}{2}\arcsin\left(\frac{4z^*}{1 + 4z^{*2}}\right)\right). \tag{4.8}$$

Here, U is the freestream velocity, ρ is the density of air, C_L is the coefficient of lift, α is the angle of attack. Because this model is based on two-dimensional potential flow, there is no drag in accordance with d'Alembert's paradox.

After substituting the aerodynamic behavior (Eqns. 4.7 and 4.8) and the consti-

tutive behavior (Eqns. 4.5 and 4.6) into the membrane force equilibrium equation (Eqn. 4.2) and rearranging, we find that the resulting governing equation becomes a function of a single dimensionless parameter, which we define as an aeroelastic number, Ae:

$$\frac{Eh}{\frac{1}{2}\rho U^2 c} + \frac{C_L(z^*, \alpha)}{(\lambda(z^*) - 1) \cdot \kappa^*(z^*)} = 0, \tag{4.9}$$

$$Ae = \frac{Eh}{\frac{1}{2}\rho U^2 c}. \tag{4.10}$$

The second term in Eqn. 4.9 is a ratio of functions that depend only on the deformed configuration of the membrane (z^*) and must exactly balance the aeroeleastic number. These functions, $\kappa^*(z^*)$, $\lambda(z^*)$, and $C_L(z^*, \alpha)$ are given by Eqns. 4.4, 4.6, and 4.8, respectively. Therefore, upon specifying the aeroelastic number and the angle of attack of a wing, the resulting camber can be predicted by solving Eqn. 4.9 implicitly for z^*. We used a numerical scheme—e.g., MATLAB's *fsolve*—to handle the implicit nature of the equation. This model permits estimating the behavior of a membrane wing *a priori*, whereas the model given by Song et al. [30] explains membrane behavior *a posteriori*.

We have made several important simplifications to keep the model tractable. The membrane is simplified as a massless, linear elastic, steady, two-dimensional structure under uniform load; the aerodynamic load is derived from a two-dimensional potential flow model that neglects the effects of viscosity, separation, transition, and unsteadiness. As these unaccounted phenomena become important, the accuracy of the model will undoubtedly degrade. Nevertheless, we can still derive some insight from the model.

4.2.2 Finite span wings

The preceding analysis for two-dimensional membrane wing sections can be adjusted further to account for some limited three-dimensional effects, thereby allowing com-

parison with experimental data from real wings. Here, we will introduce simple finite wing corrections for the aerodynamic and structural components of our model.

The change in the aerodynamic forces due to finite aspect ratio, $\mathcal{AR}$, can be easily approximated using a finite wing correction such as Helmbold's formula [see 62],

$$\frac{\partial C_L}{\partial \alpha} = \frac{2\pi}{\frac{2}{\mathcal{AR}} + \sqrt{1 + \left(\frac{2}{\mathcal{AR}}\right)^2}}.$$

This correction factor is used to correct the sectional lift coefficient given in Eqn. 4.8. Furthermore, the induced drag may contribute to the chord-normal force at large incidence, and its contribution can be approximated by $C_D = C_L^2/(\pi \mathcal{AR})$. The load on the three-dimensional membrane wing can now be found by

$$C_N = C_L \cos(\alpha) + C_D \sin(\alpha).$$

The membrane mechanics are also affected by the finite extent of the wing geometry and depend on the wing tip boundary conditions. The Young-Laplace equation given by Eqn. 4.2 was simplified for two dimensions in which the membrane can only have a single axis of curvature [50]. This two-dimensional membrane model only considers a single axis of curvature and tension in the chordwise direction—in fact this is a very reasonable approximation for a membrane wing with unrestrained wing tips or one with high aspect ratio—but in general there can be both spanwise and chordwise curvature in a finite membrane wing, and the membrane can support a biaxial stress state.

We consider an isotropic membrane under equibiaxial loading, which is a good approximation for a fully supported square membrane region under uniform load. The stretches, stresses, and curvature are equal in the spanwise and chordwise directions

and the Young-Laplace equation is simply [50, 102]

$$2\kappa + \frac{p}{T_{\text{bi}}} = 0. \tag{4.11}$$

Here, T_{bi} is the tension per length in both directions, and it is related to the equibiaxial stretch λ_{bi} [102],

$$T_{\text{bi}} = \frac{1+\nu}{1-\nu^2} Eh(\lambda_{\text{bi}} - 1). \tag{4.12}$$

The Poisson ratio, ν, depends on the membrane material. The rubbers typical of artificial membrane wings [30, 32, 36] are approximately incompressible [102]; therefore, we assume a Poisson ratio of $\nu = 1/2$, in which case $1 + \nu/(1-\nu^2) = 2$. Thus, the governing equation for this square membrane wing differs only by a factor of four from the two-dimensional membrane—a factor of two from the curvature, and a factor of two from the biaxial material response. If we simply define a modified aeroelastic constant, $Ae_{\text{bi}} = 4 \cdot Ae_{\text{2D}}$, then we can use the same formulation that we derived for the two-dimensional wing to describe the behavior of the square membrane wing. We note that a similar modification can be made for finite wings with aspect ratios between our limiting cases of $\mathcal{AR} = 1$ and $\mathcal{AR} = \infty$ although we have not explored this generalization. We also comment that the aerodynamic aspect ratio and the membrane aspect ratio are not necessarily the same if the wing is composed of multiple perimeter supported membrane regions, which is a common configuration in the literature [31, 36].

4.2.3 Wing dynamics

Now that we have a model for the bulk wing deformation, we can address the unsteady behavior of the wing about the equilibrium configuration. Previous works have found that the membrane wings undergo standing mode vibrations [27, 30, 32, 35, 36]; however, the different authors present the dynamics in a different context. Song et

al. [30] consider the natural frequency of the deformed membrane, Rojratsirikul et al. [32, 103] consider the Strouhal number typical behind rigid airfoils, Arbos-Torrent et al. [35] consider the natural frequency of the leading and trailing edge supports, and Timpe et al. [36] consider a representative frequency that is based on characteristic membrane values.

Following Song et al. [30], we use the natural modes of the deformed membrane to predict the dynamics. The governing equation (Eqn. 4.9) determines the deformed configuration of the membrane wing, so we can write the equation for the membrane fundamental frequency:

$$f_0 = \frac{1}{2\lambda c}\sqrt{\frac{T}{\rho_m h}}, \tag{4.13}$$

where the tension is given by constitutive model (Eqn. 4.5) and ρ_{m} is the membrane density. We expect the fluid-structure interaction to be strongest when the frequency of flow-instabilities match the membrane harmonics.

4.3 Computational Model

The model developed in the previous section assumes that the membrane wing is subject to a uniformly distributed load that is predicted from the Joukowski airfoil model (which is, of course, based on potential flow theory). This is a highly idealized assumption, particularly given the fact that these thin wings operate at low Reynolds number and often exhibit leading edge separation and unpredictable transition to turbulence. To assess the validity of our theory, we have developed a numerical model that couples a full aerodynamic model with the membrane wing deformations. We start with a simple structural model (linear membrane equation) and couple it with a simple flow solver (potential flow). We then progressively build up the model with additional details—such as viscous flow and nonlinear membrane mechanics—thus allowing us to systematically test the effect of each additional level of detail.

This computational model allows us to validate our analytical model in Sec. 4.2 and understand its strengths and limitations and serves as an intermediate step between the theory and our experiments.

Our approach to the computational model is similar in approach to the previous numerical works discussed [25, 28, 104]: A structural solver receives a pressure distribution from a flow solver and computes a membrane shape. Then, the structural solver informs the flow solver of a new shape. This "hand-shaking" process is iterated until an equilibrium configuration is achieved.

4.3.1 The structural model

The membrane shape is computed with a MATLAB program that solves the membrane equation (Eqn. 4.3), given a pressure distribution $p(x)$ provided by the aerodynamic model. The membrane is defined by its mean-line, $z(x)$, with leading and trailing edge coordinates $(x, z) = (0, 0)$ and $(c, 0)$ respectively. The membrane is assumed to be comprised of a linear elastic material, and the tension is given by Eqn. 4.5. The membrane has a chord length c, a thickness h, an elastic modulus E, and an unstressed initial length L_0. The membrane prestretch is $\lambda_0 = c/L_0$. The deformed membrane length L is calculated by integrating the membrane arclength,

$$L = \int_0^c \sqrt{1 + \left(\frac{d}{dx} z(x)\right)^2}\, \mathrm{d}x. \tag{4.14}$$

The tension in the membrane is calculated using linear elastic theory:

$$\begin{aligned} T &= Eh\left(\frac{L}{L_0} - 1\right) \\ &= Eh \cdot \left(\frac{\lambda_0}{c} \cdot \left(\int_0^c \sqrt{1 + \left(\frac{d}{dx} z(x)\right)^2}\, \mathrm{d}x\right) - 1\right). \end{aligned} \tag{4.15}$$

The integration in Eqn. 4.15 is approximated numerically with trapezoidal inte-

gration. The governing equation is cast using finite-difference operators,

$$\mathbf{D}_2\mathbf{z} + \frac{1}{T}\mathbf{p} = 0. \tag{4.16}$$

Here, the membrane profile and pressure are represented at discrete locations in the vectors $\mathbf{z}$ and $\mathbf{p}$, respectively. The three-point, centered finite difference operator for second derivatives $\mathbf{D}_2$ is an $N \times N$ tri-diagonal matrix.

The tension is a function of the camber profile, $T(\mathbf{z})$; therefore, the membrane equation (Eqn. 4.16) is a nonlinear equation. However, because $T(\mathbf{z})$ is a scalar factor and the Poisson equation's curvature operator is linear, Eqn. 4.16 can be solved by assuming unit tension and then rescaling the amplitude of the deformation. The final deformation is found by solving a nonlinear equation of a single variable—the maximum camber—such that Eqn. 4.16 is satisfied in the deformed configuration. The nonlinear problems are solved using MATLAB's *fsolve*.

4.3.2 The aerodynamic model

The flow over the membrane wing was computed using XFOIL, a two-dimensional steady airfoil code [105]. XFOIL uses an integral boundary layer method coupled with an outer potential flow to calculate steady flow solutions over a wing section. We use the membrane shape calculated from the structural solver to define the midline of a 1% thick membrane with rounded leading edge and cusped trailing edge and compute the flow around this "thick" membrane. Details of the membrane profile definition are described in Appendix C.

Simulations were conducted using a potential flow assumption (inviscid), and at finite Reynolds numbers: $Re = 10^5$ and 10^6. The XFOIL analysis yields pressure and skin friction coefficients at each node. At the Reynolds numbers investigated, the skin friction is two orders of magnitude less than the typical membrane tension

values and is therefore neglected.

4.3.3 Implementation

We are interested in the equilibrium configuration of a membrane under specified flow conditions. We began calculations at $\alpha = 0$ with a known solution of $z(x) = 0$, then proceeded through a series of α's where the solution of the previous angle of attack was used as the initial guess.

At each angle of attack, a new membrane profile $\mathbf{z}^s$ was calculated from the pressure distribution $\mathbf{z}^j$. The membrane profile was updated using a relaxation scheme:

$$\mathbf{z}^{j+1} = (1 - w) \cdot \mathbf{z}^j + w \cdot \mathbf{z}^s \tag{4.17}$$

where w is a relaxation parameter (typically, $w = 0.25$). A new pressure distribution $\mathbf{p}^{j+1}$ was then computed using $\mathbf{z}^{j+1}$ and the process was iterated until a self-consistent configuration was achieved. Convergence was determined by the root-mean-square change in the airfoil shape, normalized by camber:

$$\Delta z = \sqrt{\frac{1}{N} \cdot \sum_{i=1}^{N} \left(\frac{\mathbf{z}^s - \mathbf{z}^j}{\max_i(\mathbf{z}^s)} \right)^2}. \tag{4.18}$$

When $\Delta z < 5 \times 10^{-3}$, $\mathbf{z}^s$ was accepted as the the converged solution. The behavior at the next α was then computed using $\mathbf{z}^s$ as the initial guess. Using this technique, a sequence of solutions was calculated for various values of the Reynolds number Re, the aeroelastic number Ae, and the prestretch λ_0.

4.4 Experimental Methods

To validate the theoretical and numerical predictions, we performed a series of experiments on low aspect ratio ($\mathcal{AR} = 2$) rectangular membrane wing models with either free or fixed wing tips. A single experiment simultaneously measured the time-

resolved membrane shape, aerodynamic lift and wake velocities over a large range of the aeroelastic parameter.

The experiments were conducted in the Brown University low-speed wind tunnel. The facility is a closed-return tunnel with a $61 \times 58\,\mathrm{cm}^2$ test section. The experiments were conducted at freestream velocities of 5–12 m/s, which correspond to chord Reynolds numbers of 3.3×10^4–8.0×10^4. Freestream turbulence levels are $< 0.01\,\%$ [30]. The environmental conditions in the tunnel were monitored simultaneously with the experiment. The freestream velocity was measured by a Baratron pressure transducer (MKS 398HD, MKS instruments, Andover, MA), and the atmospheric pressure was monitored by an absolute pressure transducer (Model 270, Setra, Boxborough, MA). A thermistor probe and digital controller (Omega DP25-TH, Omega Engineering, Stamford, CT) monitored the temperature test section air temperature. All signals were sampled at 14 kHz for 10 seconds during each trial.

Fig. 4.2 shows the wing models used in the experiments. The model wings are comprised of a silicon rubber (Smooth-on Dragon Skin®Medium 10, Smooth-On Inc., Easton, PA) supported by 3.2 mm diameter carbon fiber rods at the leading and trailing edges. The rubber material is nearly incompressible and has a Youngs modulus $E = 280\,\mathrm{kPa}$. Two membrane thicknesses ($h = 150$ and $300\,\mu\mathrm{m}$) and two boundary conditions at the wing tip (free and fixed) were tested, for a total of four wing models. The wings were clamped in the middle, dividing the wing into two square membrane regions. In all cases the wing membranes were initially tension-free. The forces were sampled from a 6-axis force/torque transducer (Nano17, ATI Industrial Automation, Apex, NC) at 14 kHz for 10 seconds during each trial. Fig. 4.3 shows the broad range of aeroelastic constants covered by the experiments.

The membrane wing kinematics were captured by imaging a laser line that was projected onto the wing chord using a high-speed camera (Photron APX, Photron, San Diego, CA) at 1500 Hz. Two-dimensional direct linear transformation coefficients

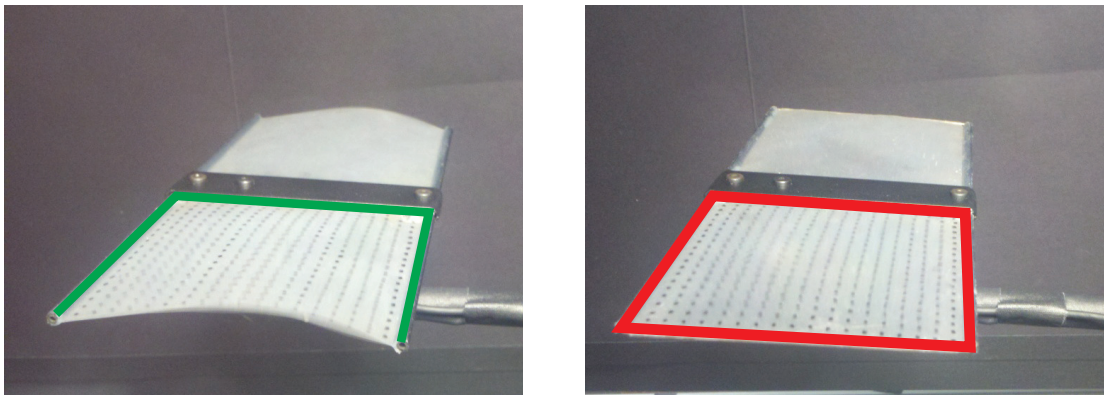

(a) Free wing tip **(b)** Fixed wing tip

Figure 4.2: The different wing configurations used in the experiments. The "free wing tip" (Fig. 4.2a) and the "fixed wing tip" (Fig. 4.2b) models were constructed with different thicknesses and tested across a range of freestream velocities 5–12 m/s resulting in a Reynolds number range based on chord length of 3.3×10^4–80×10^4. The wings were clamped at midchord, resulting in two square membrane regions that were structurally independent.

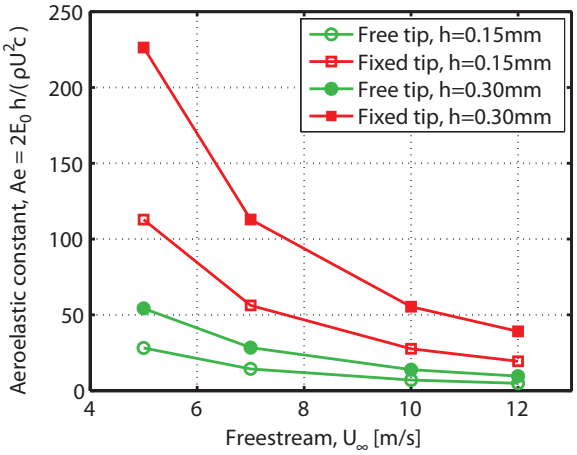

Figure 4.3: The experiments were performed over a broad range of aeroelastic constant. The wing planform was identical between all wing models; therefore, the range of Ae at a single freestream demonstrates the effect of membrane thickness and boundary support.

were computed using a calibration target in the plane of the laser sheet [106]. The plane of measurement was located at mid-half-span.

Three thousand images were captured, yielding two seconds of membrane kinematics. The images were dewarped and transformed into a coordinate system aligned with the wing chord. An FFT-based convolution of the image along the vertical direction provided a fast algorithm for locating the center of the laser line. Sub-pixel accuracy was achieved with a Gaussian sub-pixel peak finding algorithm identical to the standard PIV technique. The wing camber was calculated from the ensemble average of the digitized wing shapes. The instantaneous wing fluctuations were calculated by subtracting the time average shape from the instantaneous realizations. The wing fluctuations were approximated by Fourier sine modes in space. Power spectra of the sine mode coefficients were calculated to study the temporal behavior of the wing dynamics.

The PIV experiment was controlled by commercial PIV software (LaVision DaVis 8). The cameras (Photron SA-3) were fitted with 532 nm line-pass filters and Nikon Nikkor 85 mm/1.4 D lenses on Scheimpflug adapters. The imaged region measured $12.5 \times 12.5\,\mathrm{cm}^2$ and was illuminated with a 15 Hz dual-oscillator frequency-doubled pulsed Nd:YAG (Quantel Evergreen). The sheet forming optics were focused at a point far beyond the floor of the test section, such that the laser sheet thickness was 1.5 mm at the location of the wing tip and varied less than 0.5 mm throughout the imaged region. The flow was seeded by a Laskin nozzle that produced 1 μm DEHS oil droplets.

The PIV trials consisted of 625 image pairs. Multipass cross-correlation with an initial window size of $128 \times 128\,\mathrm{pix}^2$ and final window size $32 \times 32\,\mathrm{pix}^2$ with Gaussian weight resulted in about 106×124 vector fields with 1.2 mm spacing. The mean and fluctuation velocity fields were calculated from the PIV measurements. The fluctuation velocity fields were used to calculate root-mean-squared velocity fluctuation

intensity maps, and proper orthogonal decomposition (henceforth, POD) of the mean-subtracted velocity fields were calculated using the method of snapshots [107]. POD (also "Principle component analysis" (PCA), "Karhunen–Loeve expansion," and "the method of empirical eigenvectors"), calculates a set of eigenvectors and coefficients from a set of observations such that reconstruction with the first N eigenvectors provide the best N-order approximation of the observed data (see Berkooz et al. [108]). In the case of velocity field data, the first POD eigenvector is the most energetic mode, and the first N POD modes capture the most energy possible with an N-mode reconstruction. POD has been applied to a wide range of related problems, including model order reduction in aerodynamic flow models (e.g., Brunton and Rowley [109]) and PIV studies of aerodynamic wakes (e.g., Kim et al. [110]). Graftieaux et al. [111] have suggested POD as a tool to separate large scale vortex structures from the small scale fluctuations of turbulence or noise.

Coupled force-kinematics-PIV measurements for each wing were conducted for $\alpha = 0$–35° in 5° increments. In a separate set of experiments, detailed force measurements were performed for $\alpha = 0$–25° in 1° increments.

4.5 Results and Discussion

4.5.1 Static performance

To illustrate the difference between the aerodynamic behavior of the different wing boundary conditions, we show the lift behavior of two different wings in Fig. 4.4. These wings have the same membrane thickness ($h = 150\,\mu$m) and are subject to the same freestream velocity ($U = 12\,$m/s), but their different wing tip support leads to different effective compliance ($Ae_{\text{fixed}} = 39$ vs. $Ae_{\text{free}} = 9.6$). As seen in similar studies such as Song et al. [30], Gordnier [27], and Rojratsirikul et al. [33], the wings produce finite lift at zero angle of incidence. At low angles of attack, the lift slope is fairly linear—indicating attached flow—until about 10–12° angle of attack when the

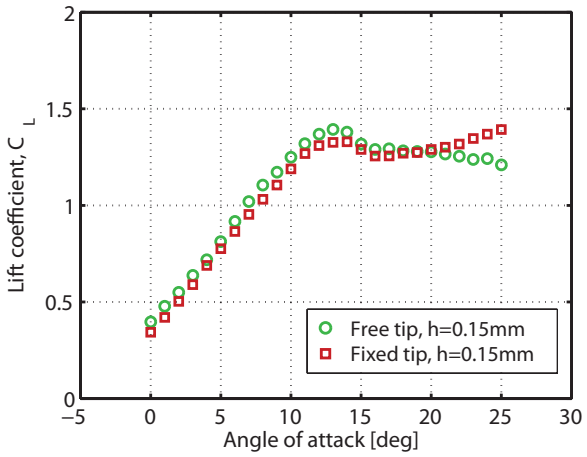

Figure 4.4: The lift coefficient is plotted as a function of angle of attack ($U = 12\,\mathrm{m/s}$ and $h = 150\,\mu\mathrm{m}$). The different wing tip boundary condition alters the post-stall behavior, but the lift at moderate angles of attack is similar between the two wings.

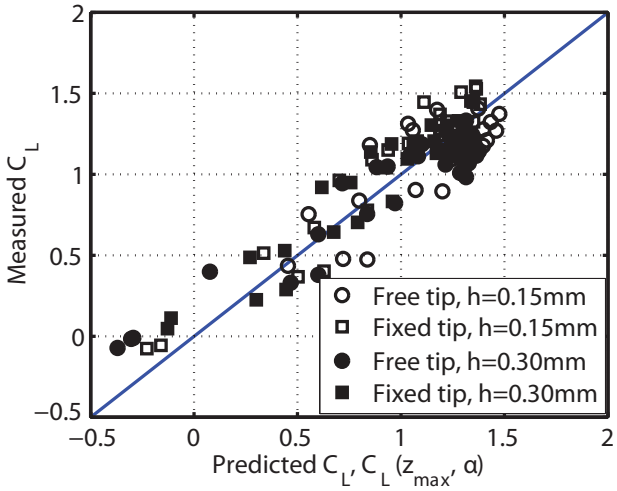

Figure 4.5: We show the directly measured lift coefficients versus the Joukowski airfoil lift prediction with finite wing correction. The lift forces are measured directly from the low aspect ratio wing models. The theory uses the wing angle of attack and the measured camber to predict the lift from the finite wing. The model comes from potential flow analysis and cannot capture viscous effects such as flow separation.

lift coefficients start leveling off. The more compliant "free" tip wings (i.e., smaller aeroelastic number) produce higher lift coefficients in the attached flow regime because of their ability to camber. The onset of stall indicates a breakdown of the Joukowski airfoil theory used in the theoretical model. At the onset of stall, the lift levels off and remains relatively flat; however, there is a noticeable difference in the behavior between the differently supported wings. The free wing tip model steadily declines in lift from 15° onwards, whereas the fixed wing tip model continues to increase in lift beyond 20°.

Here, we compare the components of the theory developed in Sec. 4.2 to experiments and calculations to demonstrate the capabilities and limitations of the theory.

4.5.1.1 Aerodynamic model

One of the contributions of this work is the incorporation of an aerodynamic model to relate the aerodynamic forces to the shape of the membrane. Here, we test the validity of the inviscid, two-dimensional Joukowski theory for a measured camber. The Joukowski airfoil theory accepts the angle of attack and the camber as inputs and provides the lift coefficient (Eqn. 4.8). We compare all of the experimentally measured lift coefficients to the Joukowski airfoil prediction in Fig. 4.5. The line is a reference for agreement between measurement and the model, and the data indeed collect along this line. The data points tend to bunch near the upper end of the lift coefficient values because nearly half of the data points occur after the onset of stall where the lift remains nearly constant (Fig. 4.4).

4.5.1.2 We–z behavior

Following Song et al. [30], we have neglected the details of the aerodynamic load distribution in order to simplify the analysis. The membrane camber is a function of the normalized aerodynamic load, i.e., the Weber number (Eqn. 4.1), which in turn

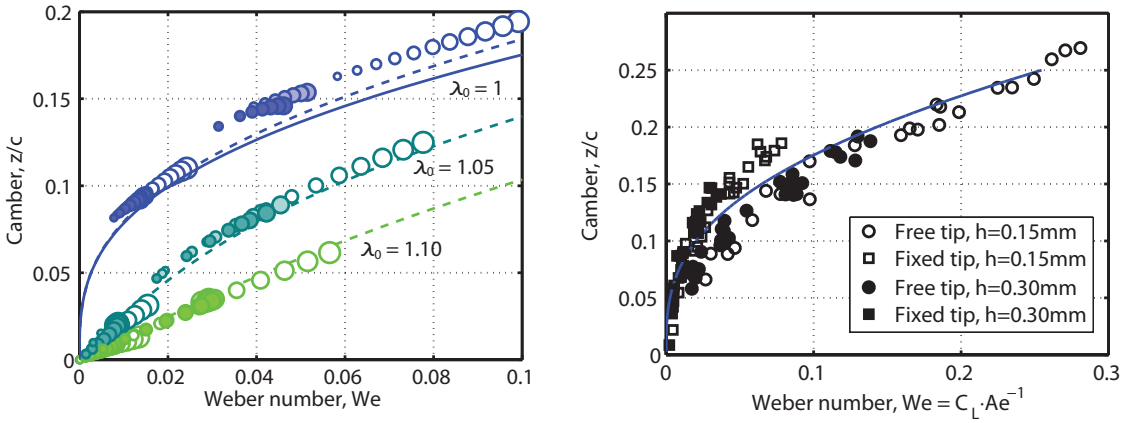

(a) Computation **(b)** Experiment

Figure 4.6: The maximum camber is given as a function of aerodynamic loading. Fig. 4.6a gives the solutions from the numerical model with specified aeroelastic number ($Ae = 31.0$ and 93.0) and specified prestretch ($\lambda_0 = 0$, 1.05, and 1.10, represented by blue, blue-green, and green, respectively) at increasing angles of attack ($\alpha = 0^\circ$ through 10°, symbol size scaled by α). The Reynolds numbers of 10^5, 10^6, and ∞ are shown, denoted by dark, shaded, and empty symbols, respectively. The solid blue line is the theoretical prediction of the model developed in Sec. 4.2. The dashed lines use the Poisson equation and are equivalent to the theory given by Song et al. [30].

is related to to the lift coefficient and the aeroelastic constant by $We = C_L \cdot Ae^{-1}$. When we arrange the membrane wing governing equation (Eqn. 4.9) in terms of the Weber number, we arrive at the relationship between camber and aerodynamic force,

$$We = -\kappa(z) \cdot (\lambda(z, \lambda_0) - 1). \tag{4.19}$$

Fig. 4.6 shows the theoretical Weber number–camber relationship (Eqn. 4.19) as the solid blue line and compares this theory to the numerical model (Fig. 4.6a) and the experiment (Fig. 4.6b). In Fig. 4.6a, symbols show results from the numerical model for two choices of the aeroelastic number ($Ae = 31$ and 93), three Reynolds numbers ($Re = 10^5$, 10^6, and potential flow), three prestretch values ($\lambda_0 = 1$, 1.05, and 1.10), and angles of attack $\alpha = 0^\circ$–10°. For each prestretch, a dashed line shows the theo-

retical dependence of camber on the Weber number when the membrane is modeled with the Poisson equation (Eqn. 4.3) [30]. The solid line represents the theoretical prediction for $\lambda_0 = 1$ (Eqn. 4.19) that was derived using the Young-Laplace membrane equation (Eqn. 4.2). Comparing the results using these two theories, we find that at small values of camber the theories are in excellent agreement, but they begin to deviate as the camber becomes large. When the camber is 15% of the chord, the difference between the two models is 4%. The difference between theses two models is small for the range of parameters calculated, thus validating the decision to use the computationally simpler Poisson equation in the numerical model [101]. Comparing the computed solutions in Fig. 4.6a to the theory, we find that the membranes without prestretch exhibit large cambers that exceed the theoretical prediction—sometimes by 10% or more for the most compliant wings. Conversely, the membranes with large prestretch exhibit small cambers that are slightly less than predicted. These theoretical under- and over-predictions of the membrane camber are due to the changing spatial distribution of the aerodynamic force as we will see in Sec. 4.5.1.3. This difference aside, the shape of the theoretical curves approximate the calculated data quite well. Starting from a point on one of the theoretical curves, changes in the aeroelastic number, Reynolds number, or angle of attack tend to move the solution along the theoretical curve; however, given a wing that is operating under certain flow conditions—namely, fixing the aeroelastic and Reynolds numbers—the calculations show that only a limited portion of the theoretical We–z curve is accessible. For example, the calculations show that the wings without prestretch exhibit nonzero camber and Weber numbers at zero angle of attack. These are the wings that exhibit lift hysteresis [30] and can never reach zero Weber number. Furthermore, stall limits how large the Weber number a given wing can attain because the Weber number is proportional to the lift coefficient. The maximum reported lift coefficients for membrane wings are in the range of 1–2 [27, 30, 103], placing an upper limit on the Weber

number around $We_{\max} \sim 2 \cdot Ae^{-1}$. For our calculations, the most compliant wing had an $Ae = 31$, therefore, $We_{\max} \sim 0.067$. As shown in Fig. 4.6a, the only calculations to reach and exceed this value were potential flow calculations; therefore, these hypothetical solutions are unrealistic and demonstrate a limitation of potential flow-based models. The limited range of Weber numbers accessible to a given wing results in the clustered appearance of the data in Fig. 4.6a, which is especially evident in the zero prestretch solutions. The Reynolds number plays a more subtle role in the operational range of a wing along its We–z curve. In general, decreasing the Reynolds number moves the operating point of the wing along its We–z curve toward the origin—i.e., less camber and less lift—a trend that has been reported in the literature [27, 28] and is attributed to the changes in the boundary layer. The inability to account for these Reynolds number effects is another limitation of potential flow-based aerodynamic models.

Fig. 4.6b shows the experimental measurements plotted against the theory. The agreement of the simple two-dimensional static theory to experimental data is good, although not perfect, particularly at low We. Like the numerical model, the fixed wing shows higher camber than predicted by the theory; however, the free wing tip tends to camber less than the theory. It is possible that spanwise variations in lift explain the discrepancy.

4.5.1.3 Chordwise load distribution

The details of the chordwise load distribution affect the We–z behavior. According to the uniform assumption, the aerodynamic load is evenly spread along the chord of the membrane; however, this is not the case in real membranes. Fig. 4.7a shows the pressure load on a membrane wing with $\lambda_0 = 1$, $Ae = 31$, and $Re = 10^5$ at angles of attack $\alpha = 2$–6°. The circles mark the center of pressure. This wing has about a 15% camber (Fig. 4.6a). At the lowest angle of incidence, the pressure distribution is

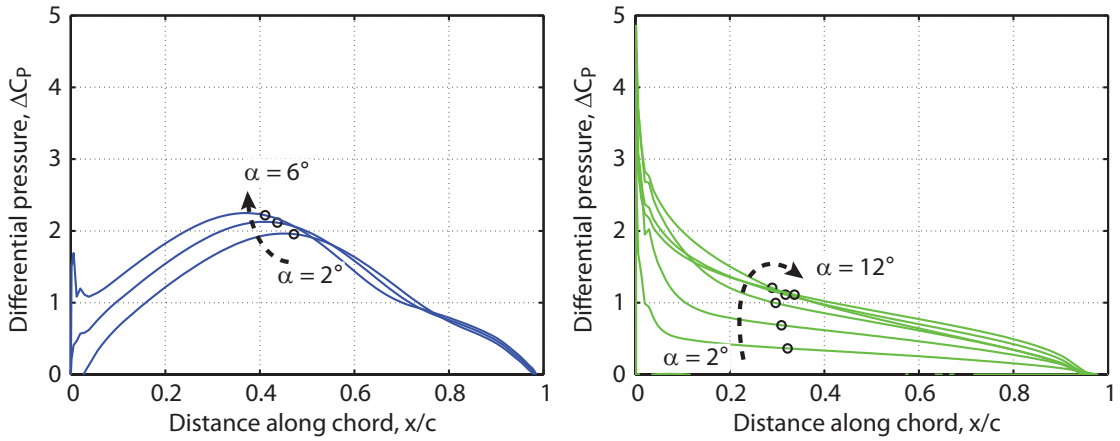

(a) $\lambda_0 = 1.00$ **(b)** $\lambda_0 = 1.10$

Figure 4.7: The XFOIL computed differential pressure profiles at $Re = 10^5$, $Ae = 31$ are shown for an unpretensioned ($\lambda_0 = 1$) and pretensioned ($\lambda_0 = 1.1$) membrane wing. The center of pressure is denoted with a circle. The arrow indicates the direction of increasing angle of attack.

concentrated near midchord where the membrane is most susceptible to deformation. As the angle of attack increases, the center of pressure shifts forward toward the leading edge support, and a leading edge suction peak develops. Fig. 4.7b shows the pressure load on a membrane wing with $\lambda_0 = 1.1$, $Ae = 31$, and $Re = 10^5$ at angles of attack $\alpha = 2$–12° and adopts cambers less than 4%. Here, the pressure distributions on the membrane wing resemble those on a flat plate, exhibiting a leading edge suction peak and a center of pressure located near the quarter chord location. As the wing begins to stall around 10°, the center of pressure moves rearward. These pressure distributions are concentrated near the leading edge support, and consequently the membrane cambers less than predicted by uniform load theory. Gordnier reported calculations that exhibit a similar behavior where a membrane wing with $Ae = 50$ and $Re = 2.5 \times 10^3$ increases in lift monotonically from $\alpha = 0$–20°; however, pressure distribution changes because of stall lead to the $\alpha = 12^\circ$ case having larger camber despite the $\alpha = 16^\circ$ case having a higher lift coefficient [27]. Clearly, the details in the aerodynamic lift distribution can play an important role on the behavior of

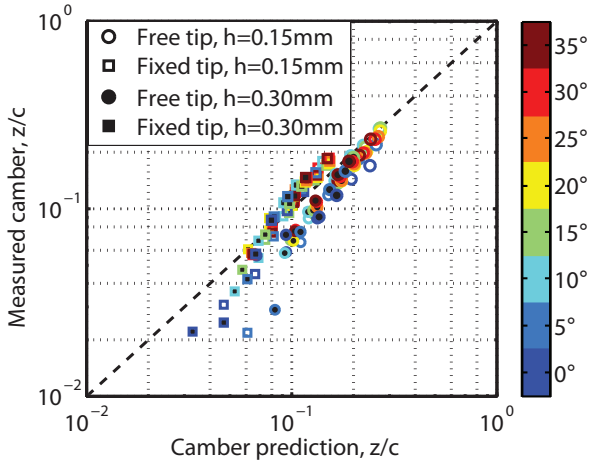

Figure 4.8: The experimentally measured camber is compared to the theoretical prediction using only Ae and α as inputs. The symbol color gives the angle of attack, and the symbol size gives the freestream velocity where the smallest size corresponds to 5 m/s and the largest corresponds to 12 m/s. The dashed line indicates perfect agreement between the model and the experiment.

a membrane wing, and our theory's uniform load assumption inhibits its ability to capture these features.

4.5.1.4 A priori prediction of membrane wing aerodynamics

The advantage of composing simple models into the aeroelastic theory developed in Sec. 4.2 lies in the ability to make a priori predictions of the wing's aerodynamic response. We predicted the maximum camber at each angle of attack and aeroelastic numbers of our experiments. The predictions are plotted against the measured values in Fig. 4.8. Each marker represents the maximum of the time-averaged camber measurement at a given freestream velocity and angle of attack and the corresponding prediction. The symbol size increases with the freestream and the color denotes the angle of attack. The circles and squares denote free and fixed wing tip models, respectively. For reference, the dashed line indicates the match between prediction and measurement. The observed camber of the free-tip wing tends to be smaller than the predicted camber, while the observed fixed-tip wing camber tends to exceed the pre-

dicted camber. The exception is at very small expected cambers where both wing's observed camber is below the theoretical prediction. These problematic predictions coincide with the smallest angle of attack and the highest aeroelastic constants where the small expected lift coefficients are comparable to the weight of the membrane.

4.5.1.5 Membrane equilibrium at $\alpha = 0^\circ$

Normally, an uncambered membrane wing at $\alpha = 0^\circ$ will produce zero lift; therefore, it is in static equilibrium in the uncambered configuration. However, any small perturbation to the membrane shape will result in the generation of an aerodynamic lift force and a membrane restoring force. If the membrane restoring force is larger than the aerodynamic force, then the membrane will return to its uncambered equilibrium configuration; however, if the aerodynamic force is larger, then the membrane camber will further increase until the membrane reaches a new equilibrium configuration with a self-sustained camber. Highly compliant membrane wings are known to exhibit self-cambering around $\alpha = 0^\circ$ [30]. Like Euler buckling for beams, this tendency for compliant membranes to adopt a deformed equilibrium configuration is due to a mathematical instability in the membrane equilibrium equation.

We can use our theoretical model to determine the critical point where the uncambered configuration changes from a stable equilibrium to an unstable equilibrium. We differentiate the Weber number (Eqn. 4.19) with respect to camber at zero camber and at zero angle of attack, and find the combinations of (λ_0, Ae) that cause the left-hand side to vanish:

$$\frac{\partial}{\partial z}\left[Ae^{-1}\cdot C_L\left(z,a\right)-\kappa(z)\cdot\left(\lambda\left(z,\lambda_0\right)-1\right)\right]\Big|_{\substack{\alpha=0\\ z=0}}=0. \tag{4.20}$$

We want to find the relationship between the prestretch and the aeroelastic number that describes the neutral stability of the uncambered equilibrium configuration.

Combinations of (λ_0, Ae) that result in the left-hand side of Eqn. 4.20 being positive will result in a self-cambering wing; conversely, when the left-hand side is negative, the wing is stable in its uncambered configuration. The criterion for stability of the uncambered equilibrium configuration is given by

$$Ae_{\mathrm{s}} \geqslant \frac{\pi}{2\left(\lambda_0 - 1\right)}. \tag{4.21}$$

We can compare the wing behavior computed with potential flow (Fig. 4.6a) to the criterion of Eqn. 4.21. The aeroelastic numbers are 31 and 93, and at the computed prestretches $\lambda_0 = 1$, 1.05, and 1.10, the criteria on the aeroelastic constant for uncambered wings is $Ae_{\mathrm{s.}} \geqslant \infty$, 10π, and 5π, respectively. From the stability criterion, we expect the pretensioned cases with $Ae = 93$ to tend to zero camber as angle of attack tends to zero, namely, $\lim_{\alpha \to 0} z = 0$. Conversely, the stability criterion indicates that the uncambered configuration is never a stable equilibrium for unpretensioned membranes; hence, unpretensioned membrane wings will always self-camber at $\alpha = 0°$—this is also clearly the case in Fig. 4.6a. The interesting case occurs at $Ae = 31$ and $\lambda_0 = 1.05$. Our analysis indicates that in this example, the stability criterion just barely exceeds the aeroelastic number ($Ae_{\mathrm{s}} = 31.4$); therefore, this case should exhibit self-camber at zero angle of attack. Indeed, for this case, $z/c = 5.1\% \neq 0$ at $\alpha = 0$ as predicted; however, as viscous effects are introduced and the Reynolds number reduced, we see that the $\alpha = 0$ camber is $z/c = 1.5\%$ at $Re = 10^6$ and $z/c = 1.0\%$ at $Re = 10^5$. Our theory does not account for the aerodynamic changes caused by viscous effects (such as boundary layers, separation bubbles, stall, etc.), but it may be possible that the decrease in lift with a decrease in Reynolds number (as described in Sec. 4.5.1.2) could stabilize a membrane wing's uncambered equilibrium that was otherwise deemed unstable by the potential flow theory.

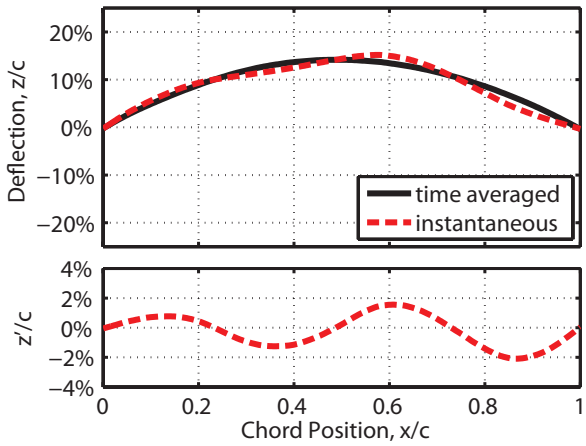

Figure 4.9: The mean membrane shape with instantaneous shape measured at mid-half-span for a fixed-tip wing at $\alpha = 10^\circ$ and $U = 10\,\mathrm{m/s}$. A fourth-mode standing wave dominates the membrane motion. Each kinematic time sequence was spatially decomposed into Fourier sine modes, and time power spectra were used to identify the dominate spatial vibration modes.

We find that our analysis is consistent with other wings reported in the literature. Song et al. [30] report lift results from two compliant latex wings, a thin wing ($h = 100\,\mu\mathrm{m}$ and $Ae \approx 10$) with prestretch $\lambda_0 = 1.04$ and a thick wing ($h = 250\,\mu\mathrm{m}$ and $Ae \approx 25$) with prestretch $\lambda_0 = 1.11$. Applying Eqn. 4.21, we find that their thin wing with less prestretch fails its stability criterion ($Ae_s \geqslant 39$), while their thick wing with more prestretch satisfies its stability criterion ($Ae_s \geqslant 14$). As expected, the thin wing self-cambered at zero angle of attack, while the thick wing remained uncambered [30].

4.5.1.6 Comment on aeroelastic constants

It should be noted that Smith and Shyy [25] use a slightly different aeroelastic parameter $\Pi_1 = \sqrt[3]{Ae}$, where the one-third power was inspired by the work of Seide [112]. Indeed, when we linearize the Weber number (Eqn. 4.19) about zero camber, we find $We \sim \frac{64}{3} z^3 + \mathcal{O}(z^5)$. This result is exactly the same as the solution given by Seide [112] with the exception of the additional plane-strain factor of $(1 - \nu^2)$ in Seide's configu-

ration. If we consider the possibility of a pretensioned membrane with initial stretch, λ_0, then we find,

$$We \sim 8\left(\lambda_0 - 1\right) z + \left(\frac{64}{3} - 32(\lambda_0 - 1)\right) z^3 + \mathcal{O}\left(z^5\right). \tag{4.22}$$

Therefore, if the membrane is pretensioned, camber will grow proportionally to We, not $\sqrt[3]{We}$.

4.5.2 Dynamic behavior

We characterized the membrane dynamics by decomposing the kinematic measurements into spatial Fourier modes. Fig. 4.9 shows a typical instantaneous membrane shape with a dashed line overlaid on the time-averaged membrane shape. Shown below, a sample instantaneous fluctuation is calculated by subtracting the instantaneous shape from the time-average. Fig. 4.9 indicates a fourth-mode wave. The mode amplitude is only about 10% of the mean deflection, supporting the idea that the membrane vibrations are small fluctuations and secondary to the mean shape.

In Fig. 4.10 we the show the experimentally measured membrane vibration frequency and compare with the standing mode estimate (Eqn. 4.13). For each measurement, we calculate the tension from the uniaxial (Eqn. 4.5) or biaxial (Eqn. 4.12) tension equation and predict the fundamental frequency of vibration (Eqn. 4.13). We then use the Fourier analysis of the fluctuations to determine the dominant mode number, and we use the frequency of the dominant membrane mode to back-calculate the membrane fundamental frequency. As mentioned in Sec. 4.2.3, the body of literature on membrane wing dynamics provides numerous approaches for understanding wing dynamics [27, 30, 32, 35, 36], including membrane natural frequency, vortex shedding frequency, chordwise advection timescales, and support vibration frequency. The validity of our choice to focus on membrane natural frequency is supported by the

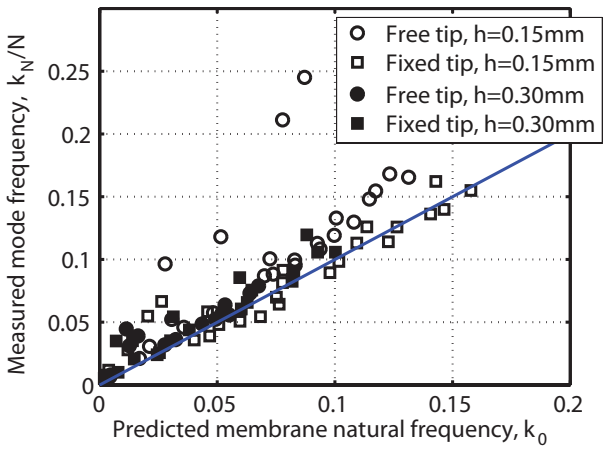

Figure 4.10: The membrane dynamics measured from the experiment are compared with the model dynamics. The solid line is the expected frequency from the linear membrane dynamics given in Eqn. 4.13. Each data point represents the expected natural frequency of the measured membrane by normalizing the observed frequency by the observed dominate mode and the expected wave speed, estimated from the measured deformation. We only plot trials with vibration mode amplitudes larger than the uncertainty of the kinematic measurement.

agreement between the predicted frequency and the observed frequency in Fig. 4.10. Furthermore, recall that we only considered chordwise modes and neglected spanwise dynamics. The experiments by Song et al. [30], Tregidgo et al. [34], and the simulation by Gordnier and Attar [29] all show predominately chordwise mode shapes dominating the dynamics of low aspect ratio wings. While this demonstrates that our simple model captures a dynamic behavior that is fundamental to membrane wings, it does not explain the choice of membrane modes. To completely understand the problem, we need to consider the other aspects that affect the wing dynamics—namely, the vortex shedding and possibly the effects of the wing supports—and understand how they relate and interact with the natural membrane modes. Song et al. [30] found the observed membrane modes of their low aspect ratio wing to be various harmonics of the fundamental frequency, with mode numbers increasing with We.

In our theoretical treatment of membrane dynamics, we simply used the deformed configuration in static equilibrium to prescribe the membrane tension that governs

the membrane dynamics. In doing so, we imply that the equilibrium wing configuration is determined independently of any wing dynamics; whereas, the membrane dynamics are intimately dependent on the bulk wing deformation. However, calculations [27] and experiments [32] show that membrane dynamics enhance the average flow structures over the wing, compared to rigid versions of identical mean shape. We find evidence for strong interaction between the membrane dynamics and the flow. Fig. 4.11 shows the lift unsteadiness as a function of angle of attack for the $h = 150\,\mu$m wings at $U = 12\,$m/s. The free-tip wing shows slightly enhanced force unsteadiness at low angles of attack; whereas, the fixed-tip wing exhibits a greatly enhanced response at moderate angle of attack. These two wings show similar lift at the moderate angles (see Fig. 4.4); however, at $\alpha = 10^\circ$ the lift unsteadiness of the fixed-tip wing ($\star\star$) is significantly higher than the free-tip wing ($\star$), despite the average lift coefficients being similar. The spectra of the force unsteadiness for these trials (Fig. 4.12) show that large force unsteadiness on the fixed-tip wing ($\star\star$) is dominated by a single frequency component. The free-tip wing ($\star$) force spectrum exhibits a peak 14.7 dB less than ($\star\star$) but with higher levels of broadband energy. Here, it appears that ($\star\star$) exhibits a strong resonance with the flow, while ($\star$) does not. Thus, while the bulk wing deformation determines membrane tension and, consequently, the membrane natural frequency, the overall dynamics are determined by the membrane harmonics that interact the most synergistically with the flow.

4.5.3 Wake measurements

Previous studies have shown 2-component PIV measurements over the suction surface of membrane wings [31, 32, 34, 36, 103]. The studies have have provided insight to the behavior of the time averaged streamlines and turbulence intensity as a function of aerodynamic conditions and membrane properties; however, these measurements fail to shed significant light on the coupling mechanism between the membrane and

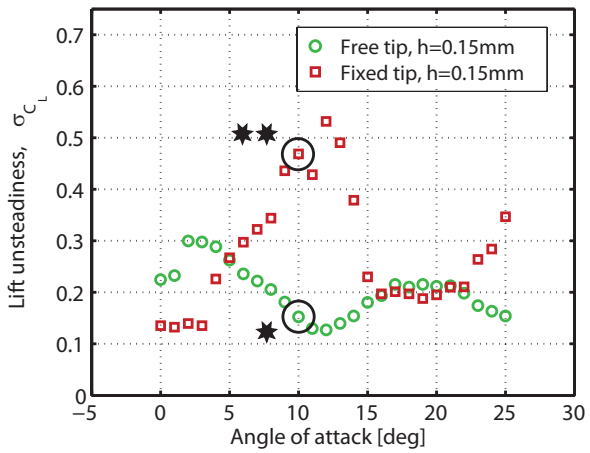

Figure 4.11: Lift coefficient unsteadiness are plotted as a function of angle of attack ($U = 12\,\mathrm{m/s}$ and $h = 150\,\mu\mathrm{m}$). At $\alpha = 10^\circ$ the lift unsteadiness of the fixed-tip wing is significantly higher than the free-tip wing, despite the average lift coefficients being similar (Fig. 4.4).

the flow. Here, we examine the measured wakes behind the two cases examined in the previous section, whose lift coefficients are similar but whose dynamics are drastically different. Fig. 4.13 shows the measured flow field in the near wake behind the free-tip wing ($\star$) and fixed-tip wing ($\star\star$) discussed in the previous section with a cartoon wing (not to scale) illustrating the relationship between the field of view and the approximate wing location. The first row shows contours of the fluctuation intensity, the second row shows the largest POD mode as a vector field for the in-plane velocity and with contours depicting the third out-of-plane velocity component, and the third row shows the vorticity field of the largest POD mode. Perhaps unexpectedly, Fig. 4.13 shows that the wake with the highest velocity fluctuation intensity ($\star$) is not the wing with the highest force unsteadiness. The free-tip wing ($\star$) wake shows high intensity velocity fluctuations developing downstream of the wing above the trailing edge. Also, high intensity velocity fluctuations emanate from the wing's trailing edge. Velocity fluctuations are completely absent in the region above the fixed-tip wing ($\star\star$). Instead, the velocity fluctuations behind the fixed-tip wing are restricted to a region approximately twice the height of the camber that emanates

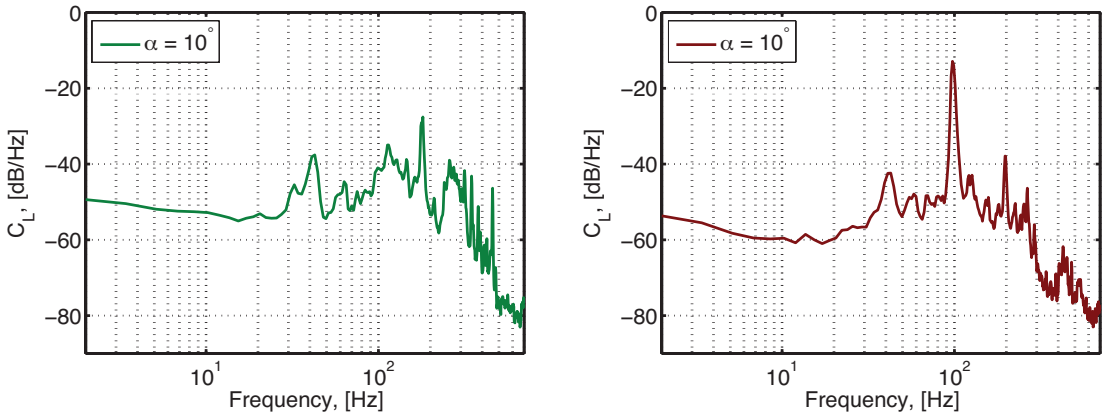

(a) ($\star$) Free tip **(b)** ($\star\star$) Fixed tip

Figure 4.12: The lift coefficient power spectra of the free- and fixed-tip wings are plotted for $\alpha = 10°$, $U = 12\,\mathrm{m/s}$, and $h = 0.15\,\mathrm{mm}$.

from the trailing edge.

The velocity fields of the first POD mode show that the large velocity fluctuations behind the free-tip wing ($\star$) are associated with flow structures with a large out-of-plane velocity component. The region behind the trailing edge of the free tip wing, despite having significant velocity fluctuations, have no influence on the first POD mode. Because POD modes are uncorrelated in time [108] we can conclude that the flow structures forming downstream and above the wing are uncorrelated to the flow structures being shed from the trailing edge. The dominant POD mode behind the fixed-tip wing ($\star\star$) shows that velocity fluctuations in the wake result from a train of vortical structures. The plot of the spanwise vorticity in the first POD mode indicate alternate vortex shedding. The vorticity behind the free-tip wing ($\star$) is much less well defined.

In each case, the second POD mode is very similar to the first POD mode, but with a 90° phase shift, as would be expected from advecting flow structures [109]. Therefore, it seems possible that the vortex street behind the fixed-tip wing is advecting with the flow, and it represents periodic starting and stopping vortices, which manifest with periodic incremental changes in the bound circulation on the wing and,

consequently, in the lift. Timpe et al. [36] calculated correlation coefficients between the membrane motion at the trailing edge of their wing and the wake velocity field. They found that their correlation coefficient fields advected downstream, suggesting that the unsteady flow structures are interacting with the membrane dynamics. Perhaps the flow structures shed from the trailing edges of these wings are correlated with the membrane dynamics. If this is the case, then the flow structures that form downstream and above the free-tip wing ($\star$) are uncorrelated with the wing motion at the trailing edge. The strong spanwise component of this POD mode suggest that these flow structures instead emanate from a different spanwise location on the wing, like the wing tip, and are convected into the current spanwise plane by the spanwise velocity. Nevertheless, despite having significantly higher velocity fluctuations in the wake, the free-tip wing has much smaller force unsteadiness than the fixed-tip wing. Hence, coherent periodic vortex shedding is more important to force unsteadiness than high levels of velocity fluctuation.

4.6 Concluding Remarks

We presented a simple description for the static and dynamic behavior of highly compliant membrane wings, which is governed by an aeroelastic constant, Ae. We conducted two-dimensional equilibrium simulations using a coupled flow and structural solver to consider the effects of chordwise load distribution. We tested several membrane wing models over a large range of Ae and angles of attack. Good agreement between our experimental results, simulations, and our predictions indicate that we have captured the essential physics.

The simple model succeeds in providing reasonable agreement with the behavior of compliant wing systems with only minimal information. The model is founded on two-dimensional linear membrane theory and two-dimensional potential flow aerodynamics yet can be adapted to give a reasonable description of a low aspect ratio

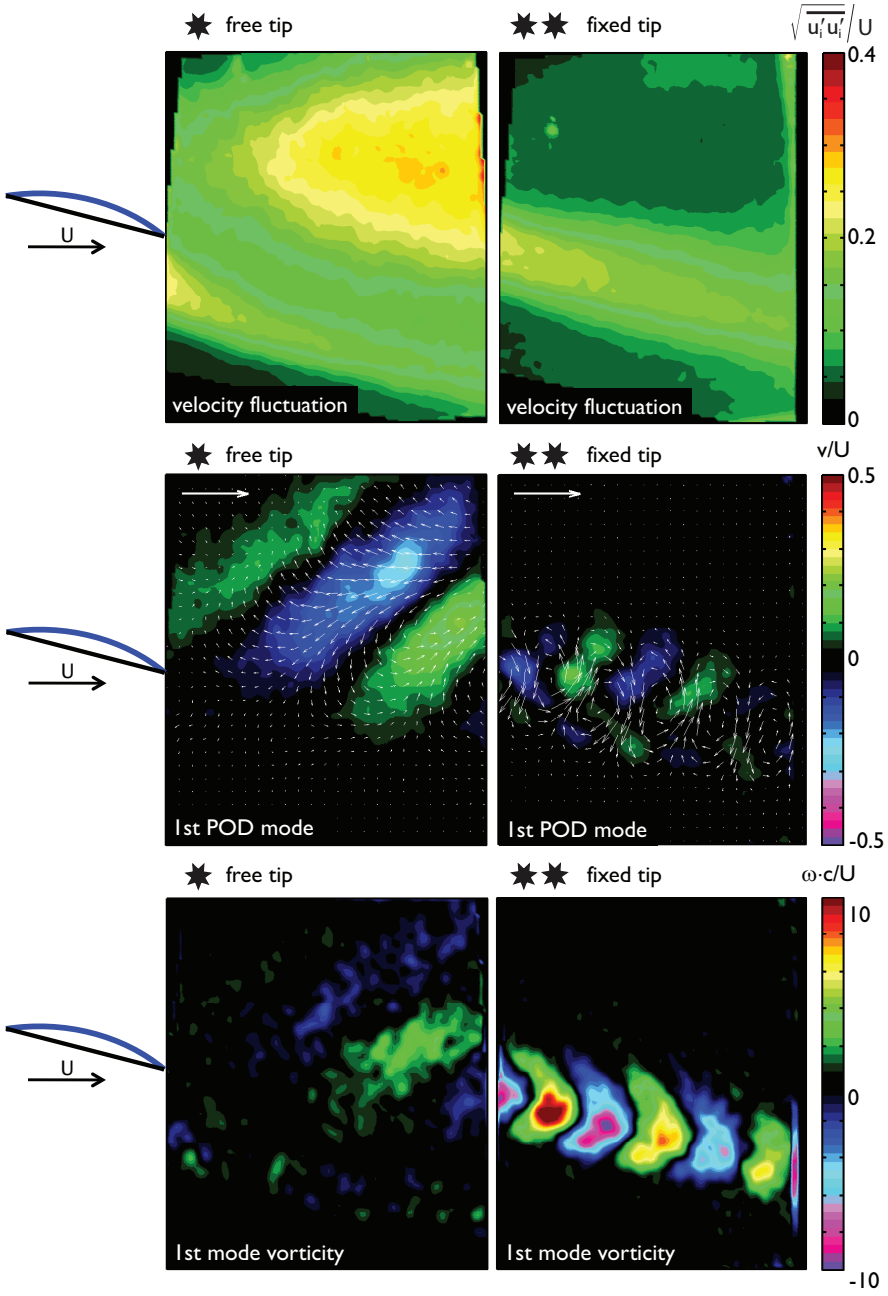

Figure 4.13: The wakes behind the special cases ($\star$) and ($\star\star$) from Fig. 4.11 are shown. The approximate wing location and a reference freestream direction are illustrated for orientation. The first row gives contours of the velocity fluctuation intensity for each wing. The second row plots the in-plane velocity vectors of the largest POD mode of each wing and represents the out-of-plane velocity (spanwise) component with contours. The third row shows the out-of-plane vorticity of the first POD mode. All values have been nondimensionalised using the freestream velocity and the chord length.

system at moderate Reynolds number. The simulations show that the uniform load distribution assumption that makes the simple model tractable still provides reasonable results. The model provides an explanation for the tendency of some membrane airfoils to snap into a cambered configuration at zero angle of incidence as well as an explanation of the vibration modes. The large wing deformation is determined by an equilibrium of the membrane forces with the average aerodynamic forces, while the membrane dynamics can be predicted from the average deformed membrane configuration.

By extending the model to simple three-dimensional geometry, we provide a simple but reasonably satisfactory explanation for the effect membrane support plays on the membrane wing behavior. We found that the boundary support for our membrane wings greatly affect their behavior—under certain conditions, the free wing tip model experienced small force unsteadiness while the fixed wing tip model exhibited a resonance. The PIV-measured wakes suggest that a resonance between vortex shedding and membrane dynamics can lead to very large unsteadiness in the force experienced by a membrane wing. The relationship between the flow conditions, the membrane mode number, and the amplitude of the membrane dynamics and forcing remains an open question.

This work was supported by AFOSR MURI on bio-inspired flight for Micro Air Vehicles, monitored by Drs. Douglas Smith and Willard Larkin

CHAPTER 5. Vortex-Wing Interactions on Low Aspect Ratio Membrane Wings

Abstract *Low Reynolds number flight ($Re < 10^5$) has recently received considerable attention because of the interest in designing Micro Air Vehicles (MAVs) as well as understanding the flight of animals who operate in similar flight conditions. Inspired by the flight of bats, we present measurements on the steady and unsteady behavior of low aspect ratio membrane wings. Membrane wings interact with the vortices shed from the leading and trailing edges and wing tips. To investigate the fluid-structure interactions on low aspect ratio membrane wings, we conduct wind tunnel experiments with coupled force, kinematic, and flow field measurements, both on the wing and in the near wake. Membrane wings interact strongly with the vortices shed from the leading and trailing edges and the wing tips, and the details of the membrane support play an important role in the fluid-structure interaction. Membranes that are supported at the wing tip exhibit less membrane flutter, more coherent tip vortices, and enhanced lift. The interior wake can exhibit organized spanwise vortex shedding and shows little influence from the tip vortex. In contrast, membranes with an unsupported wing tip show exaggerated static deformation, significant membrane fluttering, and a diffuse, unsteady tip vortex. The unsteady tip vortex modifies the behavior of the interior wake, disrupting the wake coherence.*

5.1 Introduction

Low Reynolds number ($Re < 10^5$) flight has recently received considerable attention because of the interest in designing Micro Air Vehicles (MAVs) as well as understanding the flight of animals who operate in similar flight conditions [1, 2]. The complexity, unsteadiness, and three-dimensionality of the flow features that are typical in this flight regime warrant a different flight strategy than the traditional fixed-wing approach suitable for man-made aircraft that operate at high Reynolds numbers. Design features that are traditionally considered non-ideal—such as thin wing sections, low aspect ratio, and wing compliance—have been demonstrated to boost aerodynamic performance [30, 38, 40]. Biological fliers utilize these features to successfully operate in a variety of flight modes, from hovering to migration [42].

Membrane wings are found in flying animals such as bats, gliding mammals such as flying squirrels, as well as in MAVs. The aerodynamic characteristics of these wings—e.g., self-cambering, soft stall, and enhanced performance at large angles of incidence [30]—help these wings operate at low Reynolds number. In this regime, complex phenomena such as flow separation and reattachment and the unsteady interactions between the elastic and vortical structures over the wings may critically affect the wing's aerodynamic performance. Modeling membrane wing behavior is challenging because the membrane wing's shape is not known a priori. Instead, the deformation of the membrane must be computed from the fluid forcing, which in turn depends on the membrane deformation [25, 27–29, 99, 100].

Recently, Waldman and Breuer [113] considered a simple model of a membrane wing where a time-independent equilibrium configuration of the membrane shape is calculated and then the membrane dynamics are approximated as linearized vibration modes about the equilibrium shape. This approach simplifies the analysis by decoupling the time-averaged membrane behavior from the dynamic effects and con-

sidering each in turn. The time-averaged behavior of the membrane depends on the aeroelastic number, Ae:

$$Ae = \frac{Eh}{\frac{1}{2}\rho U_\infty^2 c}. \tag{5.1}$$

Here, the membrane elastic stiffness is characterized by the modulus of elasticity, E, and the membrane thickness, h, while the aerodynamic load is characterized by the dynamic pressure, $\rho U_\infty^2/2$, and the chord length, c.

The experiments by Song et al. [30] highlight some of the key time-averaged behaviors of membrane wings. Song et al. [30] examined elastic membrane wings with leading and trailing edge support and demonstrated enhanced lift and delayed stall compared to a rigid flat plate, albeit at the expense of increased drag. The experiments also demonstrated that self-cambering of the compliant wing allows positive lift generation even at small negative angles of attack. This self-cambering behavior was also present in the high-fidelity simulations of membrane wings [27]. Here, compliance allows positive average lift to be maintained at zero angle of attack. Waldman and Breuer [113] determined that the criteria for the self-cambering depends on the pre-stretch of the membrane and the membrane stiffness. The time-averaged behavior of membrane wings also depends on the membrane's boundary conditions. Membranes with leading and trailing edge support passively change their camber in response to flow conditions [27, 30, 113], while membranes with free trailing edges passively change their angle of attack [31, 36].

Simulations by Gordnier [27] demonstrate how changes in the Reynolds number alter the thickness and stability of the boundary layer, which affects the pressure distribution on the wing. Experimentally, it is difficult to independently vary Reynolds number and effective membrane elasticity because both depend on the freestream velocity.

Membrane dynamics also play an important role in the behavior of membrane wings [27, 30, 32, 33, 36, 113]. Membrane wings may exhibit standing mode vibrations

near integer multiples of the membrane fundamental frequency [27, 30, 32, 33, 113], or they may exhibit traveling wave characteristics [27, 36]. Furthermore, the unsteady motions of the membrane alter the flow over the wing. Experimental investigations by Rojratsirikul et al. [32] and numerical studies by Gordnier [27] demonstrate that wing compliance leads to smaller separated regions over two-dimensional membrane wings than on identically cambered but rigid wings. Membrane dynamics vary greatly with the membrane pretension or excess length [30, 33], with the character of the membrane supports [31, 35, 36, 101], and with the Reynolds number [27]. The natural modes in the membrane and supports may interact with the natural modes in the wake to select the particular mode of vibration and vortex shedding. Experiments show that the wing dynamics, vortex shedding, and force unsteadiness can be altered by changing the membrane support [113] or by modulating the membrane tension at the correct frequency [114].

Another feature that is common in biological fliers and MAV design is low aspect ratio [1]. Low aspect ratio wings may take advantage of the tip vortices to entrain the flow over the wing, delaying separation as well as generating vortex lift [37, 38]. The classic result for the contribution of vortex lift was first derived for the leading edge vortices on delta wings by Polhamus [39] and later adapted for wing tip vortices by Lamar [115]. Vortex lift introduces a non-linear contribution to the potential flow lift, and the overall lift coefficient C_L as a function of angle of attack α is given by

$$C_L = K_p \sin\alpha \cos\alpha^2 + K_v \cos\alpha \sin\alpha^2. \tag{5.2}$$

Here, the empirical factor K_p is the potential flow lift slope and depends on the wing's planform [39], and in the case of an aspect ratio, $\mathcal{AR} = 2$ wing, $K_p \approx 2.5$ [37, 38]. K_v is the empirical factor for vortex lift and is typically taken to be $K_v \approx \pi$ [e.g., 37, 38]. The lift slope for a finite aspect ratio wing can be estimated using Helmbold's relation,

which relates the lift slope of the finite wing to the lift slope of the two-dimensional wing profile and the aspect ratio [62]:

$$\frac{\partial C_L}{\partial \alpha} = \frac{2\pi}{\frac{2}{\mathcal{AR}} + \sqrt{1 + \left(\frac{2}{\mathcal{AR}}\right)^2}}. \tag{5.3}$$

Experiments on low aspect ratio membrane wings with free wing tips show exaggerated wing tip dynamics and deformations compared to the midspan of the wing [30]. Computations on low aspect ratio membrane wings with fixed wing tips show that the tip vortex strength and suction are enhanced by passive mean cambering near the wing tip; however, it is unclear whether wing dynamics play an important role in the behavior of the tip vortex [29]. Stereo PIV measurements were conducted in a streamwise plane behind low aspect ratio wings with and without wing tip support [113] and show large magnitude spanwise velocity unsteadiness behind wings with free wing tips; however, the wings with supported wing tips showed much lower levels of spanwise velocity unsteadiness. Furthermore, despite having significantly less wake unsteadiness, the fixed-tip wing showed much larger force unsteadiness than the free-tip wing. Thus, the wing tip boundary condition seems to play a pivotal role in the structure of the wake and in the generation of aerodynamic forces.

In the previous chapter, we considered how the wing tip boundary support modifies the effective global stiffness of the membrane [113]; however, it is clear that there is a local effect at the wing tip, which is of critical importance for low aspect ratio wings. In this study, we investigate the relationship between the wing tip boundary support and the kinematics and aerodynamics of low aspect ratio membrane wings. We utilize Trefftz plane PIV to measure the near wake and tip vortex structure, high-speed videography to measure the membrane shape and wing tip dynamics, and direct force measurements to quantify the aerodynamic forces. We discuss the effects of the wing tip support on the local fluid-structure interactions at the wing tip, and

the consequences of these interactions on the generation of aerodynamic forces.

5.2 Experimental Methods

We performed a series of wind tunnel experiments on low aspect ratio ($\mathcal{AR} = 2.2$) rectangular membrane wings. The experiments were conducted in the Brown University low-speed wind tunnel using the same configuration as the experiments presented in the previous chapter. The facility is a closed-return tunnel with a $61 \times 58\,\mathrm{cm}^2$ test section. The experiments were conducted at freestream velocities of 5–12 m/s, which correspond to chord Reynolds numbers of 3.3×10^4–8.0×10^4. Freestream turbulence levels are $< 0.01\,\%$ [30]. The environmental conditions in the tunnel were monitored simultaneously with the experiment. The freestream velocity was measured using a Baratron pressure transducer (MKS 398HD, MKS instruments, Andover, MA), and the atmospheric pressure was monitored using an absolute pressure transducer (Model 270, Setra, Boxborough, MA). A thermistor probe and digital controller (Omega DP25-TH, Omega Engineering, Stamford, CT) monitored the test section air temperature. The forces were measured using a 6-axis force/torque transducer (Nano17, ATI Industrial Automation, Apex, NC). All signals were sampled at 14 kHz for 10 seconds during each trial.

The membrane wings are the same wings tested by Waldman and Breuer [113] and therefore supplement the kinematic and PIV measurement data from the previous work. Fig. 5.1 shows the membrane wing models. The wings are comprised of $h = 150\,\mu$m thick silicon rubber (Smooth-on Dragon Skin®Medium 10, Smooth-On Inc., Easton, PA) supported by 3.2 mm diameter carbon fiber rods at the leading and trailing edges. The rubber material is nearly incompressible and has a Young's modulus $E = 280\,$kPa. The leading and trailing edge support rods are held apart at $c = 10\,$cm by a 2.5 cm wide steel clamp at the center of the wing. The overall wingspan is $s = 22.5\,$cm, hence separating the wing into two square membrane re-

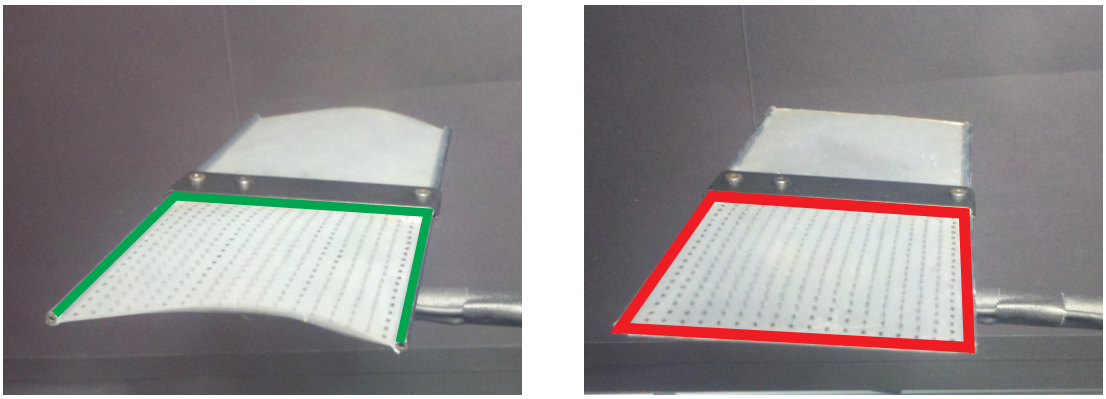

(a) Free wing tip **(b)** Fixed wing tip

Figure 5.1: The experiments were conducted on two rectangular planform membrane wings. Both wings have rigidly supported leading and trailing edges and are rigidly clamped at mid span; however, the wings have different membrane support at the wing tips. The "free-tip" model has wing tips that are completely unrestrained (Fig. 5.1a), while the "fixed-tip" model has rigidly supported wing tips (Fig. 5.1b). The range of freestream velocities $U_\infty = 5$–$12\,\mathrm{m/s}$ corresponds to a chord-Reynolds number range $Re = 3.3 \times 10^4$–80×10^4.

gions on either side of the clamp. Two boundary conditions at the wing tip (free and fixed) and a 3 mm thick aluminum flat plate with identical planform were tested.

5.2.1 Kinematics

The membrane wing kinematics were captured by imaging a laser line that was projected near the wing tip using a high-speed camera (Photron APX, Photron, San Diego, CA) at 1500 Hz. Two-dimensional direct linear transformation coefficients were computed using a calibration target in the plane of the laser sheet [106]. The plane of measurement was 16 mm from the wing tip. The measurement location is depicted in Fig. 5.2.

Three thousand images were captured, yielding two seconds of membrane kinematics. The images were dewarped and transformed into a coordinate system aligned with the wing chord. An FFT-based convolution of the image along the vertical direction provided a fast algorithm for locating the center of the laser line (see Appendix D). Sub-pixel accuracy was achieved with a Gaussian sub-pixel peak finding

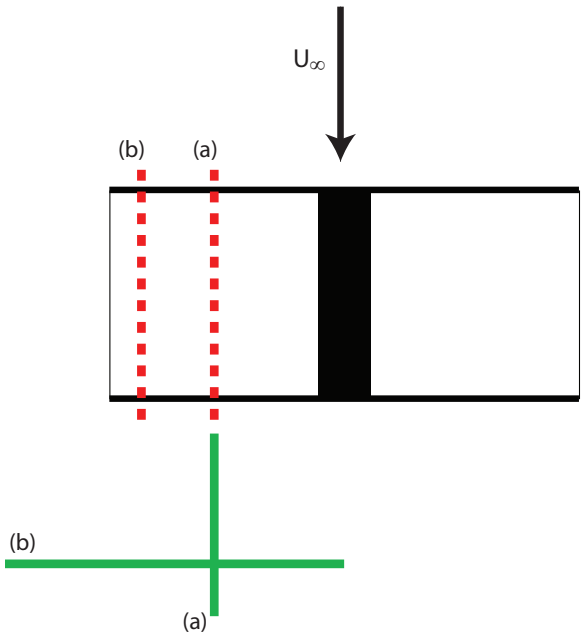

Figure 5.2: The locations of the kinematic and PIV measurements are illustrated by the dashed red lines and the solid green lines, respectively. The label (a) indicates the location of previous kinematic measurements at 25% span and co-planar streamwise wake PIV measurements [113]). The new kinematic measurements are located close to the wing tip, and the PIV measurement is oriented in the flow-normal Trefftz plane, which is labeled (b).

algorithm identical to the standard PIV technique [54]. The wing camber was calculated from the ensemble average of the digitized wing shapes, and the instantaneous wing fluctuations were calculated by subtracting the time average shape from the instantaneous realizations. At each chordwise location, power spectra of the wing fluctuations were calculated to quantify the wing dynamics.

5.2.2 Stereo PIV

The wake behind the left half of the wing was measured in the Trefftz plane using stereo PIV. The PIV measurement location relative to the wing is depicted in Fig. 5.2. At low-to-moderate angles of attack, the measurements were performed using the dual-plane PIV technique for increased accuracy [71]. Single-plane PIV measurements were conducted at post-stall angles of attack ($\alpha = 20$–25°) to adequately capture the large streamwise velocity deficits due to separated flow. The laser sheet thickness, h, the laser sheet displacement, Δx, the interframe time, Δt, and the volume retention, V_R, were determined for each freestream velocity $U_\infty = 5$–$12\,\mathrm{m/s}$ based on the analysis by Waldman and Breuer [71], and the experimental parameters are summarized in Table 5.1.

Table 5.1: PIV experimental details

	Angle of attack α [deg]	Laser thick., h [mm]	Laser disp., Δx [mm]	Interframe time, Δt [μs]	Vol. Ret., V_R [%]
Single-plane	20–25	3.0	0.0	100–40	71
Dual-plane	0–15	2.0	2.7	540–225	100

The PIV experiment was controlled by commercial PIV software (LaVision DaVis 8). The cameras (Photron SA-3) were fitted with 532 nm line-pass filters and Nikon Nikkor 85 mm/1.4 D lenses on Scheimpflug adapters. The imaged region measured $20 \times 30\,\mathrm{cm}^2$ and was illuminated with a 15 Hz dual-oscillator frequency-doubled pulsed Nd:YAG laser (Quantel Evergreen). The laser sheet was formed by a negative cylindri-

cal lens ($f = -25\,\text{mm}$), and the laser sheet thickness was controlled with a focusable lens according to Table 5.1. The flow was seeded by a Laskin nozzle that produced $1\,\mu$m DEHS oil droplets.

Each PIV trial consisted of 625 image pairs. Multipass cross-correlation with an initial window size of $128 \times 128\,\text{pix}^2$ and final window size $32 \times 32\,\text{pix}^2$ with Gaussian weight resulted in about 106×124 vector fields with 1.2 mm spacing. The PIV measurements were used to calculate the ensemble average velocity and the fluctuation energy fields for each trial. The tip vortex properties were extracted from the PIV measurements using the full-field vortex fitting approach proposed by Bhagwat and Ramasamy [116]. Meander-corrected ensemble average and fluctuations were calculated using the instantaneous vortex locations.

5.3 Results and Discussion

5.3.1 Lift

Fig. 5.3 shows measured lift coefficients from the membrane wings and the flat plate for a freestream velocity $U_\infty = 12\,\text{m/s}$, and theoretical lift curves as given by Eqn. 5.2. The non-zero lift evident at $\alpha = 0^\circ$ results from the self-cambering behavior of the membrane wings. At low angles of attack, the lift from the wings increases linearly with angle of attack until reaching a maximum around $\alpha = 13^\circ$. The linear lift behavior at low angles of attack is consistent with previously reported experimental measurements [30] and simulations [27]. After reaching maximum lift, the free-tip wing exhibits a decrease in lift coefficient as the angle of attack further increases. In contrast, after the fixed-tip wing initially stalls, the lift coefficient continues to increase again with further increases in the angle of attack.

The measured lift coefficient of the flat plate wing is compared to Polhamus' suction analogy prediction (Eqn. 5.2). Here, Helmbold's relation (Eqn. 5.3) was used to approximate $K_p = 2.82$ for the $\mathcal{AR} = 2.25$ wing, which is consistent with results

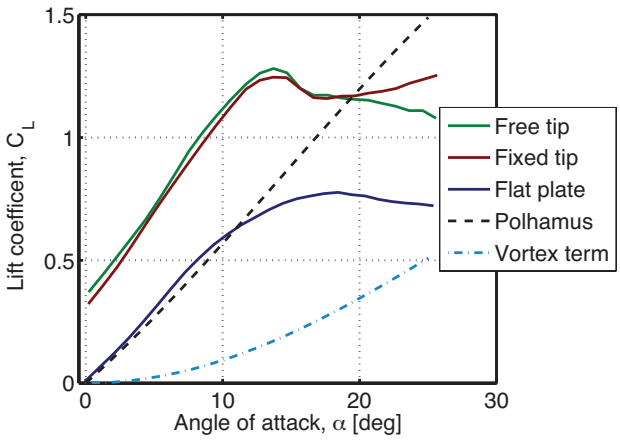

Figure 5.3: The measured lift coefficient vs angle of attack for the two membrane wings, a flat plate, and theoretical prediction based on the suction analogy are compared. Measurements were taken at a freestream velocity $U_\infty = 12\,\mathrm{m/s}$. The dashed line is the full suction analogy originally given by Polhamus [39] for delta wings. The dash-dot line is only the vortex-lift term from the full suction analogy.

of Torres and Mueller [37]. At low angles of attack, the measured flat plate lift slope is slightly larger than the suction analogy prediction until the wing begins to stall at about $\alpha = 10°$. Fig. 5.3 also shows the contribution of the second term in the suction analogy equation (Eqn. 5.2), the "vortex term," which accounts for the nonlinear contribution of the vortex to the total lift.

Fig. 5.4 shows the lift behavior of the membrane wings over the tested range of freestream velocities. The error bars specify the standard error of each force measurement, $\sigma/\sqrt{N}$. Here, σ is the standard deviation of each trial's force samples, and N is the number of independent measurements and is estimated as the number of chord lengths the freestream advects during the trial. For a given wing, the aeroelastic number decreases proportional to inverse square of the freestream velocity (Eqn. 5.1), which leads to increases in wing camber and lift [113]; this can be seen in Figs. 5.4a–d as a monotonic upward shift in the lift curves with increasing freestream velocity. Across the tested freestream velocities, the wings consistently exhibit linear lift dependence on angle of attack at low-to-moderate angles of attack. At these pre-stall angles, the free-tip wing exhibits larger lift coefficients than the

fixed-tip wing [113]; however, the difference between the free-tip and fixed-tip wings' lift coefficients decreases as the freestream velocity increases. The theoretical model developed in chapter 4 overpredicts the measured camber for the fixed-tip wing, but the model underpredicts the measured camber for the free-tip wing (Fig. 4.8). Thus, the decreasing difference between the lift coefficients of the free- and fixed-tip wings may be caused by the wing camber effects that cannot be predicted by the two-dimensional, potential flow theory.

At post-stall angles of attack, Fig. 5.4 shows that the fixed-tip wing exhibits superior lift to the free-tip wing at some point after the onset of stall. Furthermore, at the three highest freestream velocities tested, the fixed-tip wing lift coefficient is still increasing with angle of attack beyond 25°, while the free-tip wing lift coefficient is monotonically decreasing from the maximum lift attained at the onset of stall.

The negative lift recorded at the lowest angles of attack at $U_\infty = 5\,\mathrm{m/s}$ highlights a characteristic of highly compliant membrane wings that has been largely ignored in previous studies—sagging under gravity. Previous studies on unpretensioned membrane wings have neglected membrane weight in their models [e.g., 25, 27, 30, 113], avoided data points near $\alpha = 0°$ [e.g., 32, 33, 35], or have avoided the issue by mounting the membrane wings vertically [e.g., 30]. Given a membrane wing configured in the traditional sense, with the planform oriented normal to the direction of gravity, the weight of the membrane effectively acts as a uniformly distributed negative lift. The weight of the membrane wing will be significant when it is comparable to the lift coefficient:

$$\frac{\rho_m g h}{\frac{1}{2}\rho U_\infty^2} \quad \text{vs.} \quad C_L. \tag{5.4}$$

Here, ρ_m is the membrane material density, h is the membrane thickness, and g is the gravitational acceleration. For a freestream velocity $U_\infty = 5\,\mathrm{m/s}$, and a membrane density $\rho_m = 1.07\,\mathrm{g/cm^3}$, the membrane weight bias is -0.105. Given that the membrane wing experiences an effective negative lift coefficient of -0.105 because of

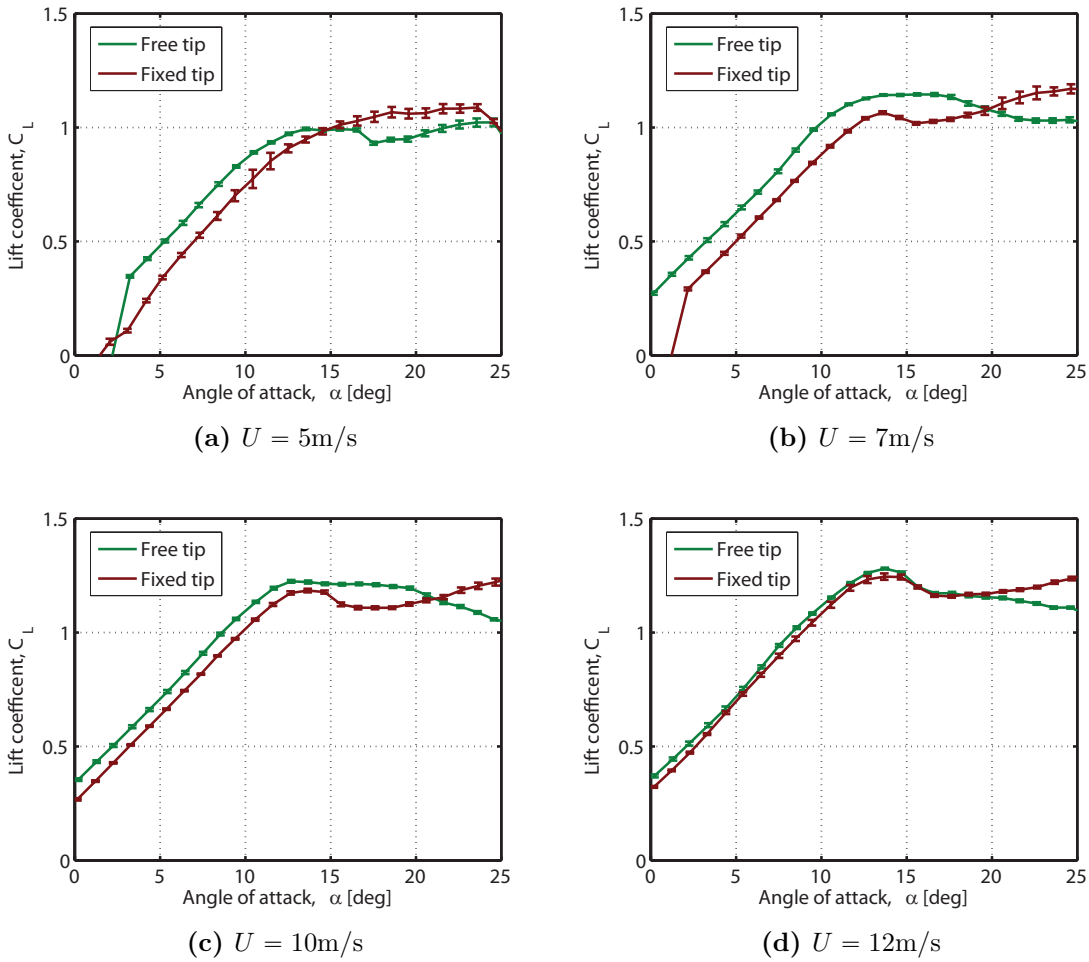

(a) $U = 5\text{m/s}$ **(b)** $U = 7\text{m/s}$

(c) $U = 10\text{m/s}$ **(d)** $U = 12\text{m/s}$

Figure 5.4: The free- and fixed-tip wing lift coefficients are plotted versus angle of attack for each freestream velocity $U_\infty = 5$–$12\,\text{m/s}$. The error bars represent the standard error of each measurement.

gravity, and the lift slope $K_p = 2.82$ as estimated by Helmbold's equation (Eqn. 5.3), we can estimate an equivalent angle of attack bias due to gravity as $\alpha_{\text{bias}} = 2.2^\circ$. This bias estimate agrees with the positive-negative lift transition in Fig. 5.4a.

5.3.2 Kinematics

The wing tip membrane support plays an important role in the behavior of the membrane wing by altering the global effective membrane stiffness [113] and by directly affecting the membrane behavior in close proximity to the wing tip. Fig. 5.5 shows the

ensemble-averaged camber of the wing as a function of angle of attack at both the mid-half-span and near-wing-tip locations. The wing camber at mid-half-span (located at 25% span from the wing tip) reflects the aerodynamic forces on the wing. Similar to the lift coefficient, the camber is initially positive at $\alpha = 0^\circ$ and steadily increases with the angle of attack. As the wing begins to stall and the lift coefficient reaches a maximum, the camber also reaches its maximum. Furthermore, as the free-tip wing continues to lose lift with further increase in the angle of attack, the wing camber also decreases with the angle of attack. Meanwhile, the fixed-tip wing lift and camber begin to increase again with angle of attack in the post-stall regime. Overall, the lift coefficients of the free- and fixed-tip wings are very similar; however, because of the wing tip constraint, the fixed-tip wing exhibits smaller wing camber. This relationship between the camber and the lift is consistent with membrane wing theory [25, 30] and is consistent with the reported membrane behavior [27, 30, 32, 33, 113].

The camber near the wing tip (located at 7% span from the wing tip) shows markedly different behavior. Near the fixed wing's tip, because of the support of the nearby rigid tip, the membrane camber resembles a scaled-down version of the mid-half-span behavior. The free-tip wing, however, is unconstrained and exhibits enhanced compliance in the wing tip region, which causes the wing tip to exhibit a larger camber than observed at the inboard regions of the wing. Strangely, the wing tip shows increasing camber all the way to $\alpha = 20^\circ$ despite the fact that the lift coefficient is monotonically decreasing for $\alpha > 14^\circ$. Song et al. [30] reported measurements that demonstrated exaggerated wing tip flare until $\alpha = 30^\circ$ and postulated the presence of a strong tip vortex that was responsible for the wing tip behavior.

The error bars in Fig. 5.5 represent the root-mean-square amplitude of the membrane deflections about the ensemble-averaged camber, and thus quantify the unsteadiness of the membrane about its ensemble-averaged configuration. The free-tip wing shows large membrane fluctuations at the wing tip when $\alpha = 0^\circ$, and the

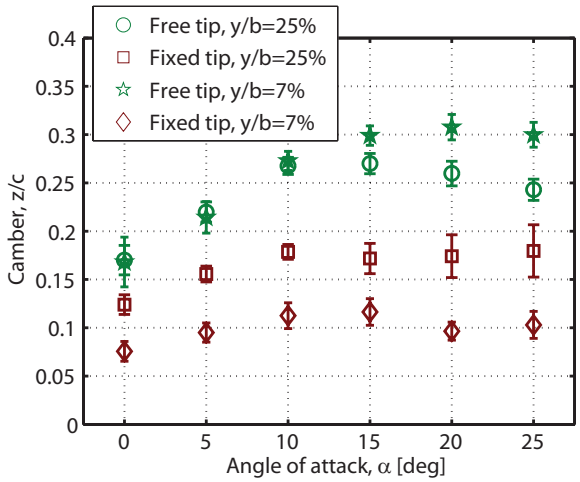

Figure 5.5: Membrane camber is shown as a function of angle of attack with a freestream velocity $U_\infty = 12\,\mathrm{m/s}$. The membrane camber was measured at two locations: mid-half-span ($y/b = 25\%$) and near-wing-tip ($y/b = 7\%$). The error bars show the root-mean-square amplitude of the membrane deflection around the mean shape. The mid-half-span membrane kinematics data are originally from [113].

presence of fluctuations throughout the post-stall angles. The fixed-tip wing's mid-half-span exhibits large membrane post-stall dynamics; however, at moderate angles of attack, the membrane unsteadiness is very moderate. Near the fixed wing tip, the membrane unsteadiness is moderate throughout all angles of attack, despite being in close proximity to a rigid membrane boundary.

To investigate the details of the membrane dynamics, we calculated the power spectra of the time-resolved membrane fluctuations. At each chordwise location, we calculated the power spectral density of the membrane deflection using Welch's method [117] with 600-sample windows and 50% window overlap. The resulting periodogram versus chordwise position reveals the spatial distribution of the membrane vibrations (Figs. 5.6 and 5.7 for the free-tip and fixed-tip wings, respectively). The dynamics measured at mid-half-span ($y/b = 25\%$) are shown in the left column, and the dynamics measured near the wing tip ($y/b = 7\%$) are shown in the right column. Selected spectra are shown for the angles of attack, $\alpha = 0°$, $10°$, and $25°$, which represent the dynamics when the wings are under the smallest load, under pre-stall

conditions, and under post-stall conditions, respectively.

First, consider the dynamics of the free-tip membrane wing shown in Fig. 5.6. At $\alpha = 0^\circ$, the free-tip wing exhibits large amplitude dynamics with vibration energy distributed throughout many frequencies and membrane modes. The most prominent mode is the first-mode vibration at about 20 Hz, which is obvious at the wing tip and present to a lesser degree on the inner wing. The center frequency of the first vibration mode at the wing tip is below the frequency of the first mode observed at mid-half-span, which indicates that the membrane tension (and consequently, the wave speed) at the free wing tip is lower than the inner wing tension [113]. As the angle of attack increases to $\alpha = 10^\circ$, the vibration energy is contained in a strong sixth-mode vibration near 180 Hz, with some second-mode energy also present at 60 Hz. These modes imply that the membrane fundamental frequency is at 30 Hz, which reflects the increase in tension with the increase in camber (Fig. 5.5). Further increasing the angle of attack into the post-stall regime ($\alpha = 25^\circ$) results in the mid-span dynamics reverting to a second-mode vibration just below 60 Hz. As the lift decreases beyond stall (Fig. 5.4d), the wing camber decreases (Fig. 5.5) and results in reduced membrane tension, wave speed, and fundamental frequency, which is seen by the decrease in the second-mode frequency. At the wing tip, the membrane dynamics are still dominated by vibrations just below 60 Hz, but the second-mode's node is missing. Additional energy is present at frequencies corresponding to third-mode and higher harmonics and is spatially distributed along the chord. This distribution of energy along the chord—along with second-mode dynamics expected from the previous Fourier mode analysis [113]—suggests that the wing tip experiences traveling wave motions. In all cases, the membrane dynamics at the mid-half-span show more clearly defined standing mode shapes, whereas the wing tip dynamics are less clearly spatially defined, indicating more traveling wave dynamics. Also, the dynamics near the free wing tip shows more vibration energy in the background throughout the

frequency and spatial range, thus demonstrating noisier, less coherent membrane vibrations. For example, at the post-stall angle ($\alpha = 25^\circ$), the 60 Hz dynamics have an amplitude of -6 dB at both mid-half-span and at the wing tip; however, the mid-half-span low frequency noise has a lower amplitude (-21 dB), is more spatially localized (between $x/c = 0.3$ and 0.6), and has a smaller bandwidth ($f < 6$ Hz) than the noise at the wing tip (-17.5 dB amplitude, between $x/c = 0.2$ and 0.8, and $f < 20$ Hz).

The fixed-tip membrane dynamics are shown in Fig. 5.7. Similar to the free-tip wing dynamics, at $\alpha = 0^\circ$, the fixed-tip wing dynamics show vibration energy distributed over many modes and frequencies, especially in the first and third modes at 20 and 60 Hz, respectively. At mid-half-span, the third vibration mode does not show a clear separation between the second and third antinodes, indicating traveling wave dynamics over the trailing edge half of the wing. Near the fixed wing tip, none of the nodes in the third mode can be clearly identified between antinodes, and the additional presence of the fourth and fifth modes indicate traveling waves dominate the motion at the wing tip. At $\alpha = 10^\circ$, the membrane is in a standing fourth-mode vibration just below a frequency of 100 Hz, with very little low frequency energy present. At the post-stall angle $\alpha = 25^\circ$, the membrane motion is dominated by the second mode with 60 Hz frequency, with very little low frequency energy present.

Both wings exhibit shifts in the natural frequency with changing angle of attack. The changing natural frequency is expected as the wing camber and, consequently, the wing tension changes with wing loading [113]. Comparing the magnitude of the membrane unsteadiness, the fixed-tip wing exhibits much smaller background vibrations near the wing tip compared to the free-tip wing. The energy in the fixed-tip wing's vibrations is concentrated in the dominant vibration mode of the given configuration, while free-tip wing's vibration energy is distributed among larger background vibrations and harmonics. Both wings show higher levels of broadband background

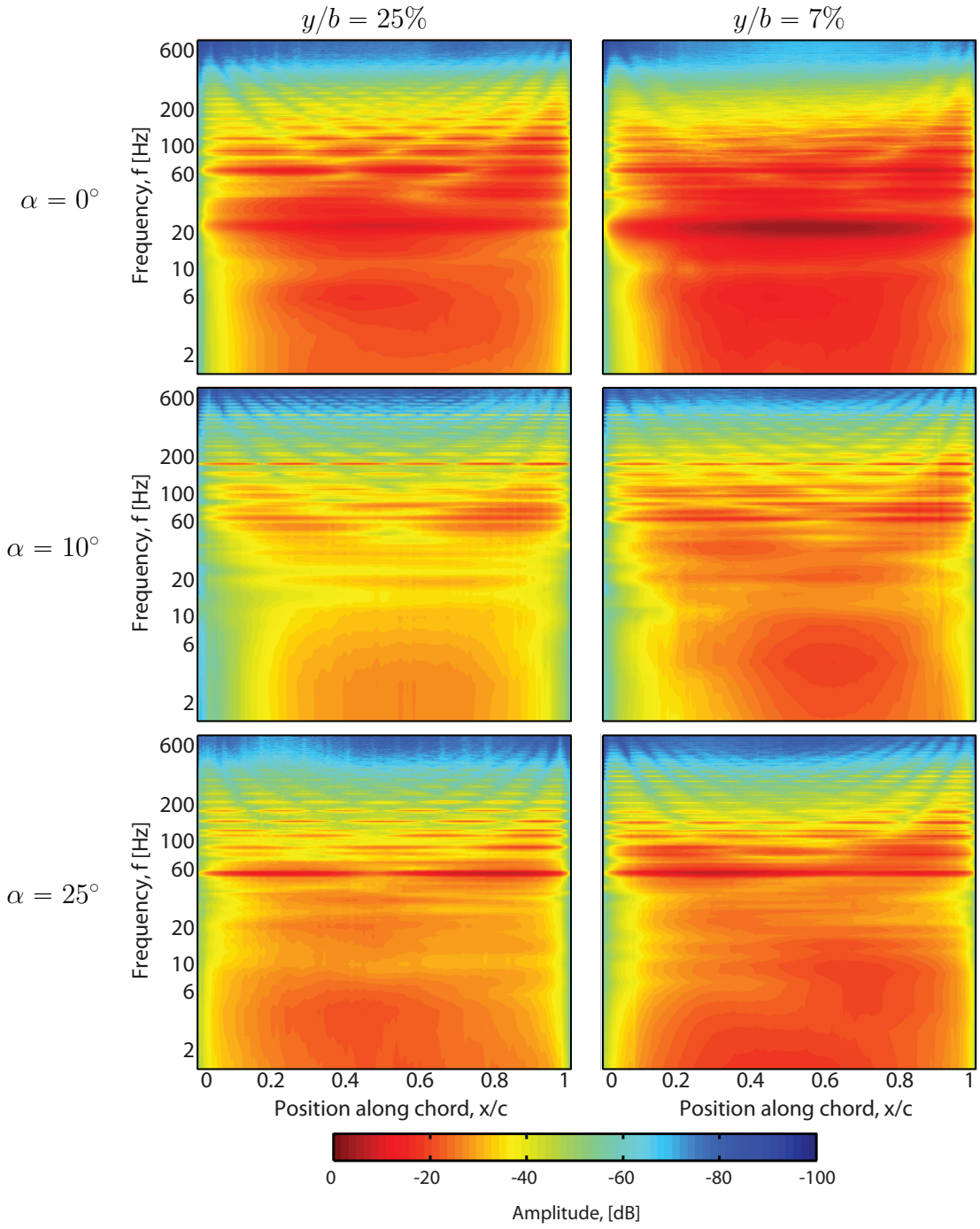

Figure 5.6: Free-tip wing membrane dynamics at the mid-half-span ($y/b = 25\%$) and near-wing-tip ($y/b = 7\%$) locations. The power spectra are plotted in a decibel scale referenced to 1 mm displacement. The mid-half-span membrane kinematics data are originally from [113].

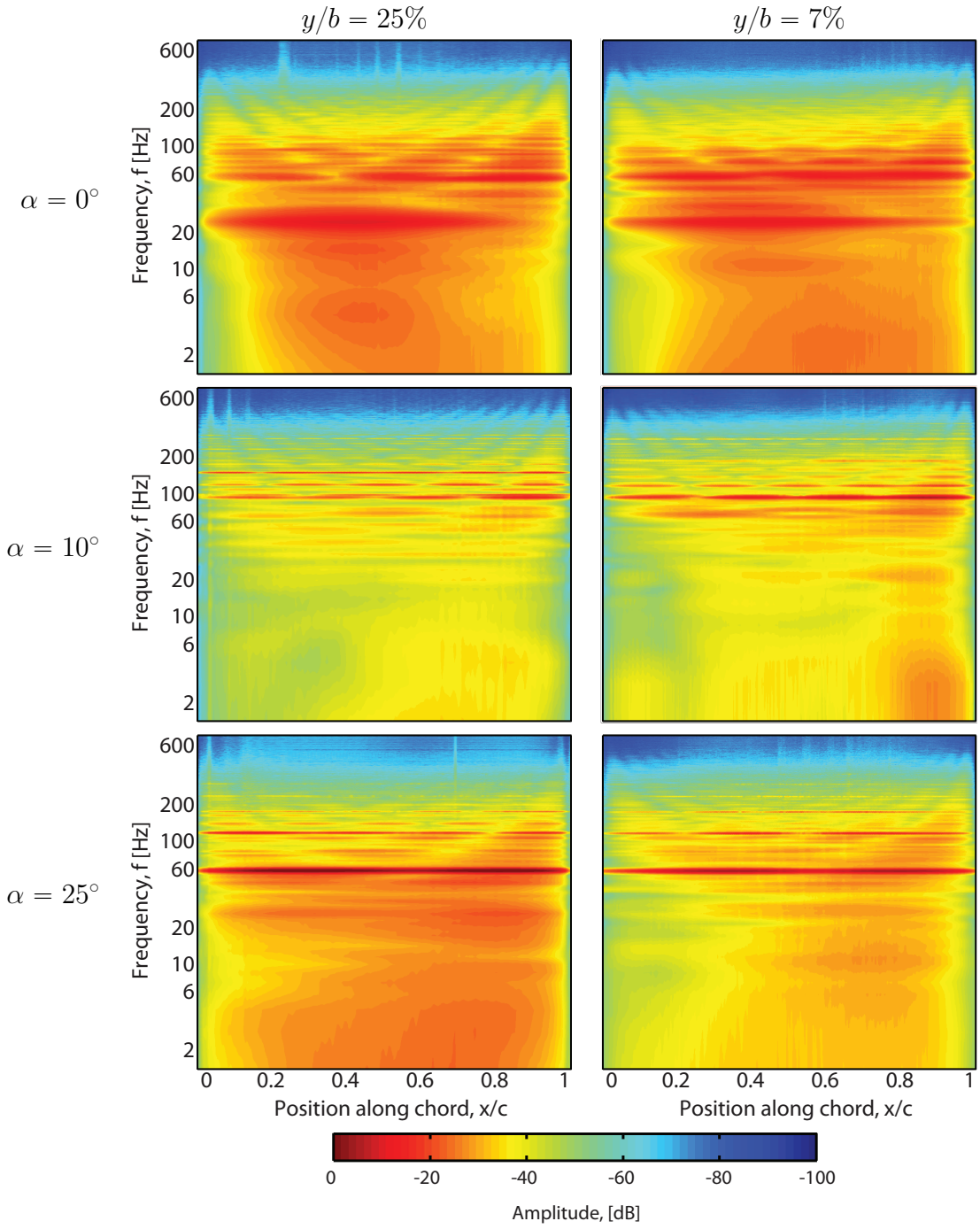

Figure 5.7: Fixed-tip wing membrane dynamics at the mid-half-span ($y/b = 25\%$) and near-wing-tip ($y/b = 7\%$) locations. The power spectra are plotted in a decibel scale referenced to 1 mm displacement. The mid-half-span membrane kinematics data are originally from [113].

vibration near the trailing edge across all angles of attack, which is visible as higher concentrations of yellows, oranges, and reds at the trailing edge throughout the frequency range in both Figs. 5.6 and 5.7. The higher concentration of broadband vibrations at the trailing edge suggest that trailing edge flow separation occurs on all models at all angles of attack. Previous experiments by Rojratsirikul et al. [32, 33] show attached flow on the front of cambered membrane airfoils and the presence of flow separation near the trailing edge. Furthermore, Rojratsirikul et al. [32] also reported observing second-mode vibrations for angles of attack greater than 20°, which is consistent with our experimental data. It is important to note that the wing tip dynamics were measured a short distance (7% span) inward from the actual wing tip. On the fixed-tip wing, the membrane is rigidly constrained by the boundary condition; thus, both the dynamics and camber line at the very tip of the wing are necessarily zero. Meanwhile, the free wing tip will have both an exaggerated mean camber and flutter. Thus, the kinematic measurements show that the free-tip wing exhibits a highly deformed and unsteady wing tip, whereas the fixed-tip wing has a flat, rigid wing tip.

5.3.3 Wake structure

The differences in the wing tip shape and dynamics lead to significant differences in the structure of tip vortices behind the free- and fixed-tip membrane wings. The ensemble-averaged streamwise vorticity contours (Fig. 5.8) show that for all angles of attack, the free-tip wing has a large and diffuse tip vortex, while the fixed-tip wing has a much smaller, more intense tip vortex. The strength of the tip vortex behind the free-tip wing increases in intensity until $\alpha = 15°$, after which the vortex becomes very diffuse. The tip vortex behind the fixed-tip wing has a smaller size and higher intensity and retains these features even beyond stall. Interesting features to note are the small patches of opposite-signed vorticity on the right side of the figures

near mid-span. These patches represent the vortex lines being shed from the wing root as the bound circulation decreases with decreasing camber towards the clamp at half-span.

The velocity unsteadiness helps to explain the difference between the tip vortex structure of the two membrane wings. Fig. 5.9 shows the magnitude of the velocity fluctuations, namely, the root-mean-square of the velocity fluctuations,

$$RMS\left(\mathbf{u}'\right) = \sqrt{\overline{u'^2} + \overline{v'^2} + \overline{w'^2}}. \tag{5.5}$$

Here, the prime $'$ denotes a fluctuation from the ensemble average, and u, v, and w are the streamwise, spanwise, and vertical components of the velocity vector $\mathbf{u}$, respectively.

The impact of the free membrane boundary condition at the wing tip on the tip vortex is very clear: in all cases, the extent of the wake unsteadiness is vastly increased by the presence of a free wing tip. At pre-stall angles of attack, the extent of the unsteadiness from the free wing tip nearly reaches across the entire span of the wake. At post-stall conditions, massive flow separation across the wingspan contributes additional velocity unsteadiness. The fixed-tip wing exhibits a much smaller unsteady region emanating from the wing tip. At $\alpha = 10^\circ$, the velocity fluctuations exist in a compact region around the wing tip, and the unsteadiness shed from the inner wing is distinct from the wing tip unsteadiness. The wake shed from the inner wing exhibits the expected spiral shape as the wake rolls around the tip vortex during the roll-up process [4, 45]. After the onset of stall at $\alpha = 20^\circ$, the free-tip wing still shows evidence of a highly organized tip vortex, even though the center of the wing has stalled.

Trailing vortices are known to fluctuate about their average positions, and accurately quantifying mean vortex properties requires a procedure to correct for vortex

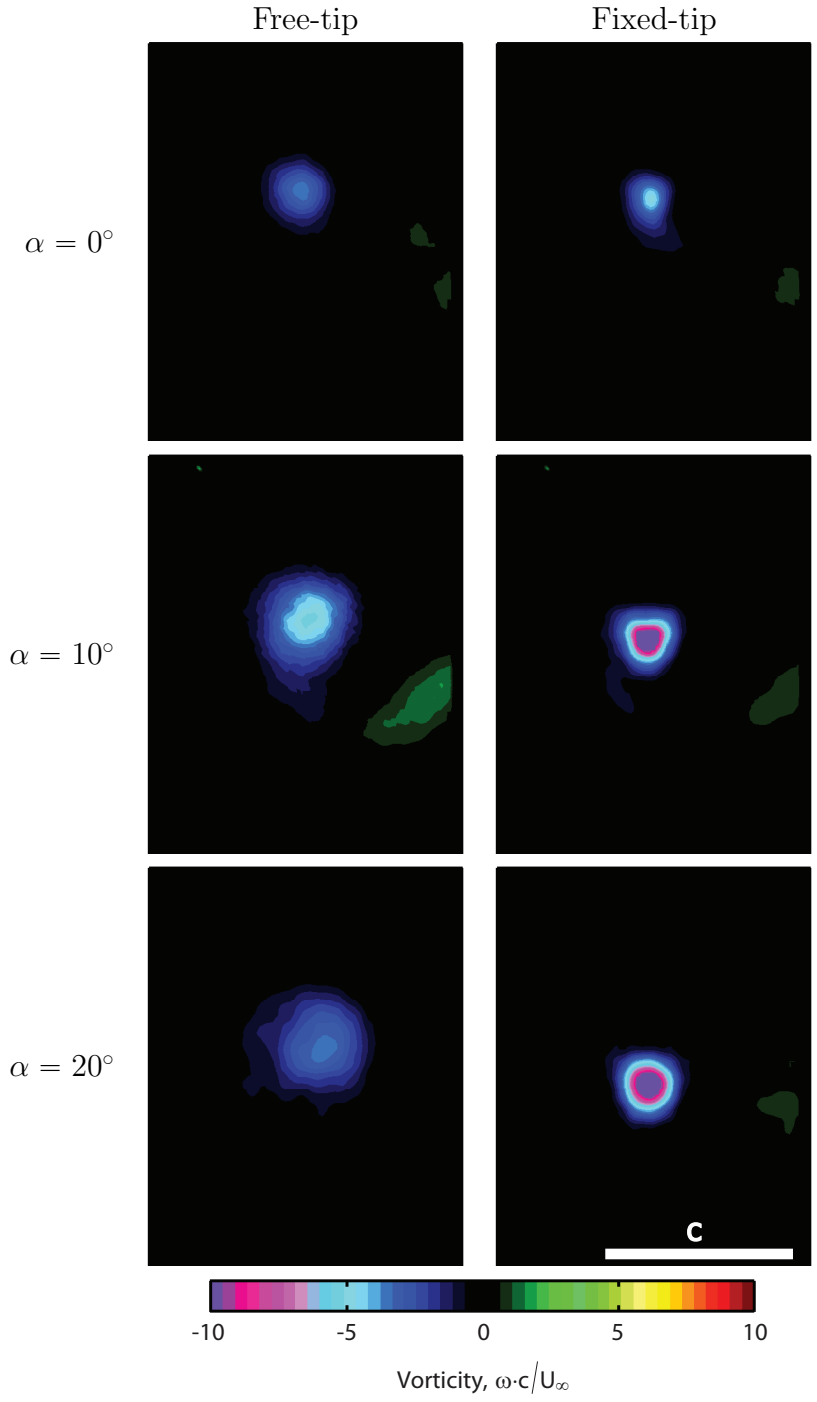

Figure 5.8: The streamwise vorticity contours for the free- and fixed-tip wings are compared across a range of angles of attack at $U_\infty = 12\text{m/s}$. The view is behind the left half of the wing, located a distance $1.4c$ downstream of the trailing edge. The scale bar indicates one chord length.

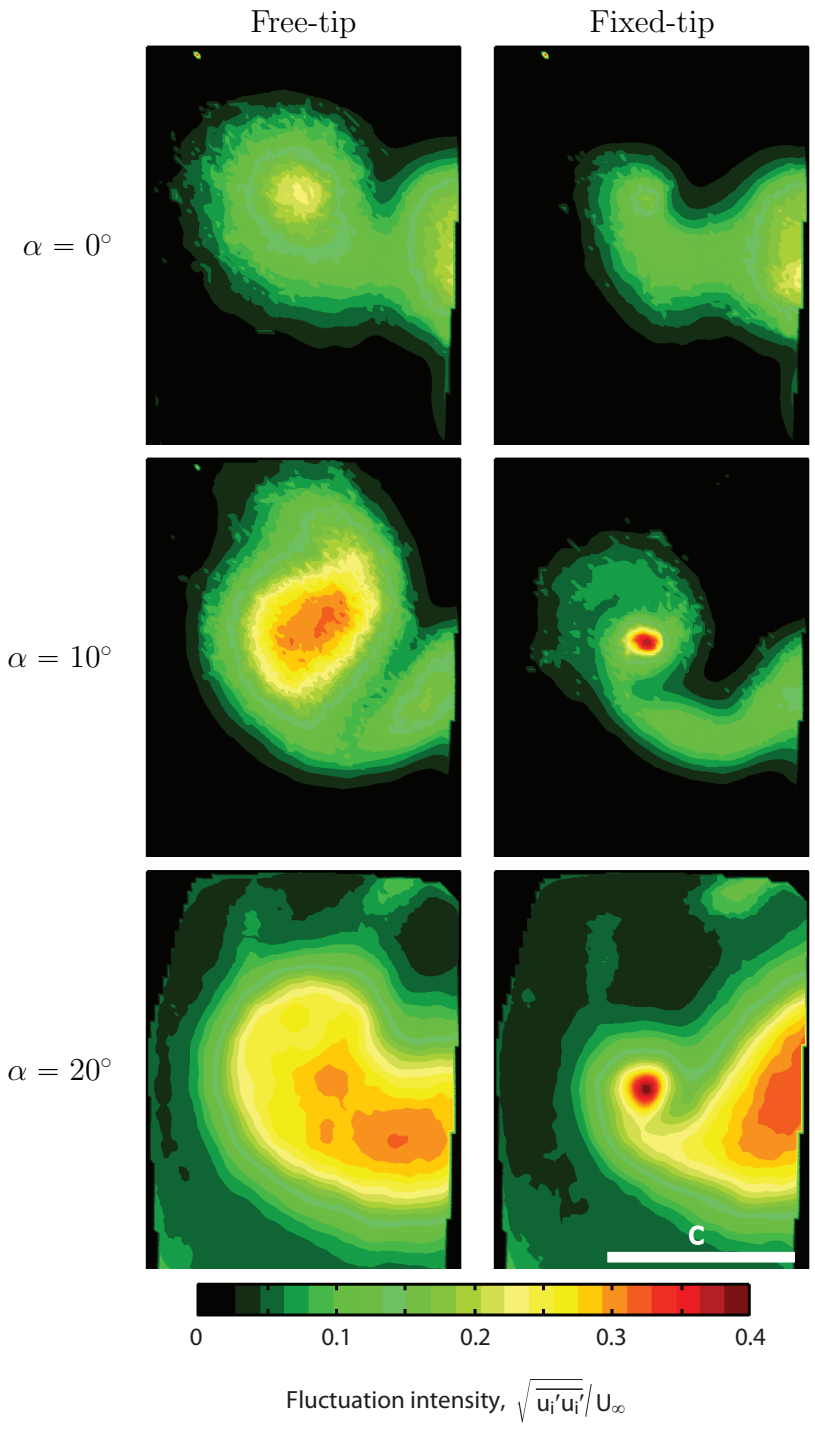

Figure 5.9: The velocity fluctuation energy contours for the free- and fixed-tip wings are compared for angles of attack $\alpha = 0^\circ$, 10°, and 20°, at $U_\infty = 12$m/s. The view is behind the left half of the wing, located a distance $1.4c$ downstream of the trailing edge. The scale bar indicates one chord length.

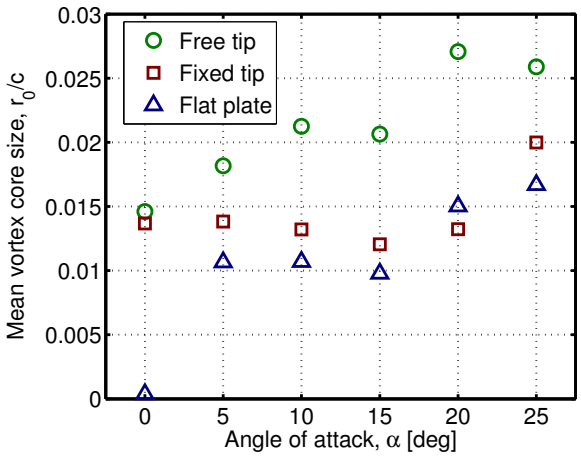

Figure 5.10: Comparison of tip vortex core sizes calculated from meander-corrected measurements of the membrane wings and a flat plate. Calculated from PIV measurements $1.4c$ downstream from the trailing edge.

meander [45]. Following Bhagwat and Ramasamy [116], we recalculated the velocity fields and vortex properites, correcting for vortex meander using a global least-squares fit of the data to the classic Lamb-Oseen vortex model,

$$u_\theta\left(|\mathbf{x}-\mathbf{x}_0|\right) = \frac{\Gamma_0}{2\pi\,|\mathbf{x}-\mathbf{x}_0|}\left(1-\exp\left(-\left(\frac{|\mathbf{x}-\mathbf{x}_0|}{r_0}\right)^2\right)\right). \tag{5.6}$$

Here, the vortex is defined by its strength Γ_0, its core size r_0, and its location $\mathbf{x}_0$, and these parameters are determined from the global least-squares fit of Eqn. 5.6 to each instantaneous PIV snapshot. Fig. 5.10 shows the ensemble average core size of tip vortices, r_0, from each of the membrane wing models and from the flat plate, measured from the meander-corrected velocity fields. The fixed-tip wing and the flat plate exhibit very similar vortex core sizes for all angles of attack, whereas the free-tip wing's vortex size is significantly larger than either of the other two wings. Additionally, the free-tip wing's tip vortex exhibits larger root-mean-square meander amplitudes, σ, than the tip vortices from either the fixed-tip wing or the flat plate (Fig. 5.11).

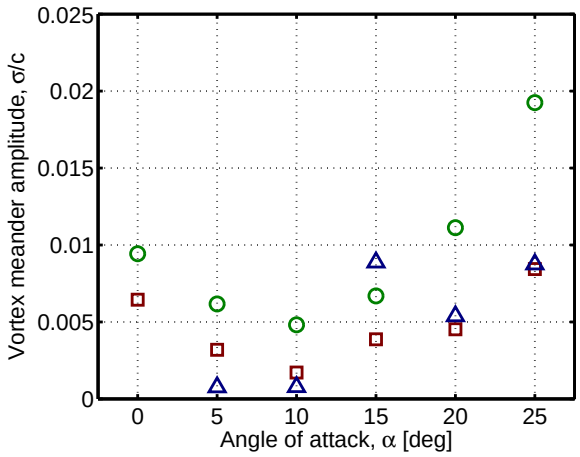

Figure 5.11: Comparison of tip vortex core meander amplitude calculated from meander-corrected measurements of the membrane wings and a flat plate. Calculated from PIV measurements $1.4c$ downstream from the trailing edge.

Fig. 5.12 compares the velocity fluctuation intensity calculated before and after applying the vortex meander correction to the velocity fields. The top row is the original $\alpha = 20^\circ$ plots of the velocity fluctuation intensity from Fig. 5.9, and the second row is the meander-corrected velocity fluctuation intensity. The velocity fluctuations in the free-tip wing wake remain nearly unchanged by the vortex meander correction in contrast to the fixed-tip wing, which exhibits a significant decrease in the velocity fluctuation intensity in the tip vortex core. Hence, the apparent velocity unsteadiness in the tip vortex behind the fixed-tip wing is largely due to the tip vortex meander, whereas the velocity unsteadiness behind the free-tip wing is uncorrelated with the tip vortex and therefore represents a highly turbulent wake. The 25% freestream velocity fluctuation intensity levels present in the tip vortex wake behind the free-tip wing are similar to freestream turblence levels that Sytsma and Ukeiley [118] found to reduce lift coefficients on $\mathcal{AR} = 2$ flat plates.

5.3.4 Streamwise wake structure

In the previous chapter, the fixed-tip wing was found to exhibit significantly larger lift unsteadiness than the free-tip wing under otherwise identical flow conditions

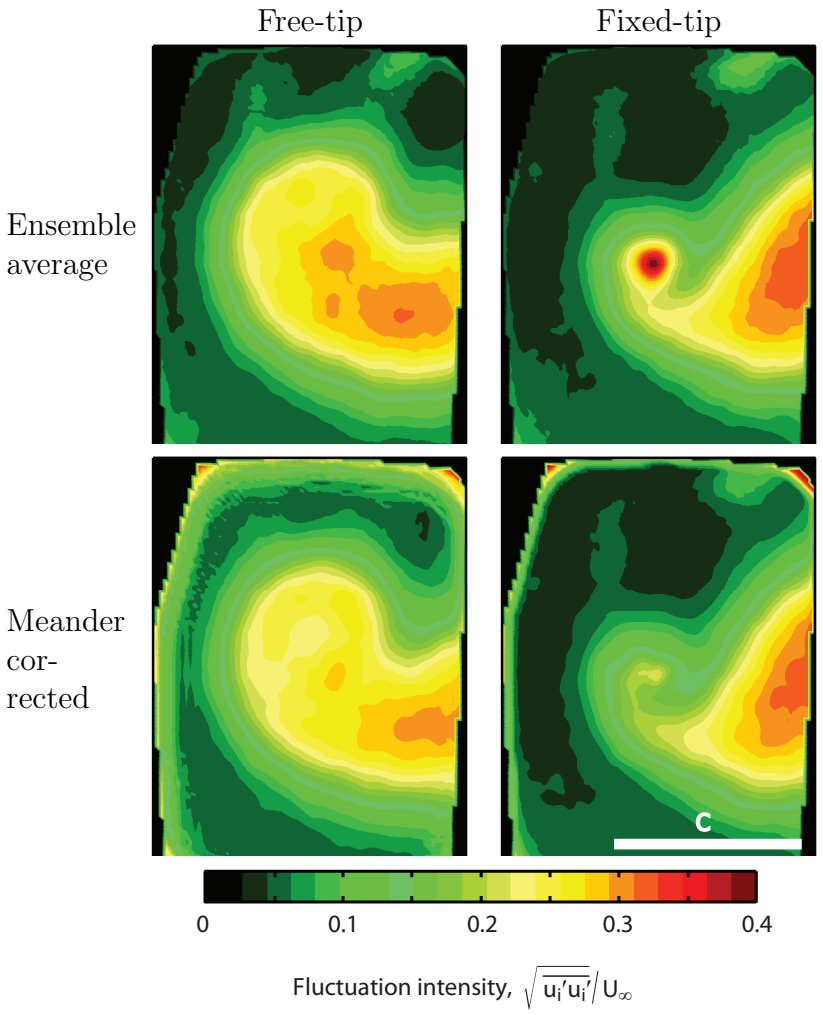

Figure 5.12: A comparision of the velocity fluctuation before and after vortex meander correction. Free- and fixed-tip wings are compared for angles of attack $\alpha = 20^\circ$ at $U_\infty = 12$m/s. The view is behind the left half of the wing, located a distance $1.4c$ downstream of the trailing edge. The scale bar indicates one chord length.

($U_\infty = 12\,\mathrm{m/s}$ and $\alpha = 10^\circ$) and to exhibit very similar overall lift coefficients [113]. Streamwise PIV measurements behind the mid-half-span location showed that the unsteadiness in the wake behind the fixed-tip wing was confined to a narrow region immediately behind the wing's trailing edge (Fig. 4.13). Proper orthogonal decomposition analysis revealed that the unsteadiness was dominated by alternating sign vortex shedding from the trailing edge. Surprisingly, the free-tip wing that exhibited much smaller force unsteadiness produced substantially more flow unsteadiness in a much larger wake than the fixed-tip wing. Fig. 5.13 shows the spatial relationship between the Trefftz plane PIV measurements and the streamwise measurements from chapter 4. The left column of Fig. 5.13 shows the streamwise sections of the wakes relative to the time-averaged mid-half-span membrane camber profiles and the location of the Trefftz plane measurement. The right side of Fig. 5.13 shows the velocity fluctuation intensities measured in the Trefftz plane and the spanwise location of the streamwise PIV measurements. In all quadrants, the velocity fluctuation intensities are plotted for the same flow conditions. The first row in Fig. 5.13 shows the free-tip wing and its wake with large fluctuation intensities in the regions behind the trailing edge and above the wing. The second row in Fig. 5.13 shows the fixed-tip wing and its wake with the velocity unsteadiness in a narrow wake behind the trailing edge. Fig. 5.13 demonstrates that the large region of velocity unsteadiness in the streamwise measurement that looms above and behind the free-tip wing is the large and highly unsteady tip vortex produced from the freely-fluttering membrane wing tip. The streamwise region behind the mid-half-span location on the fixed-tip wing remains unaffected because the tip vortex lacks unsteady flow features.

5.4 Concluding Remarks

We presented detailed force, kinematic, and PIV wake measurements from wind tunnel experiments on low aspect ratio compliant membrane wings with different wing

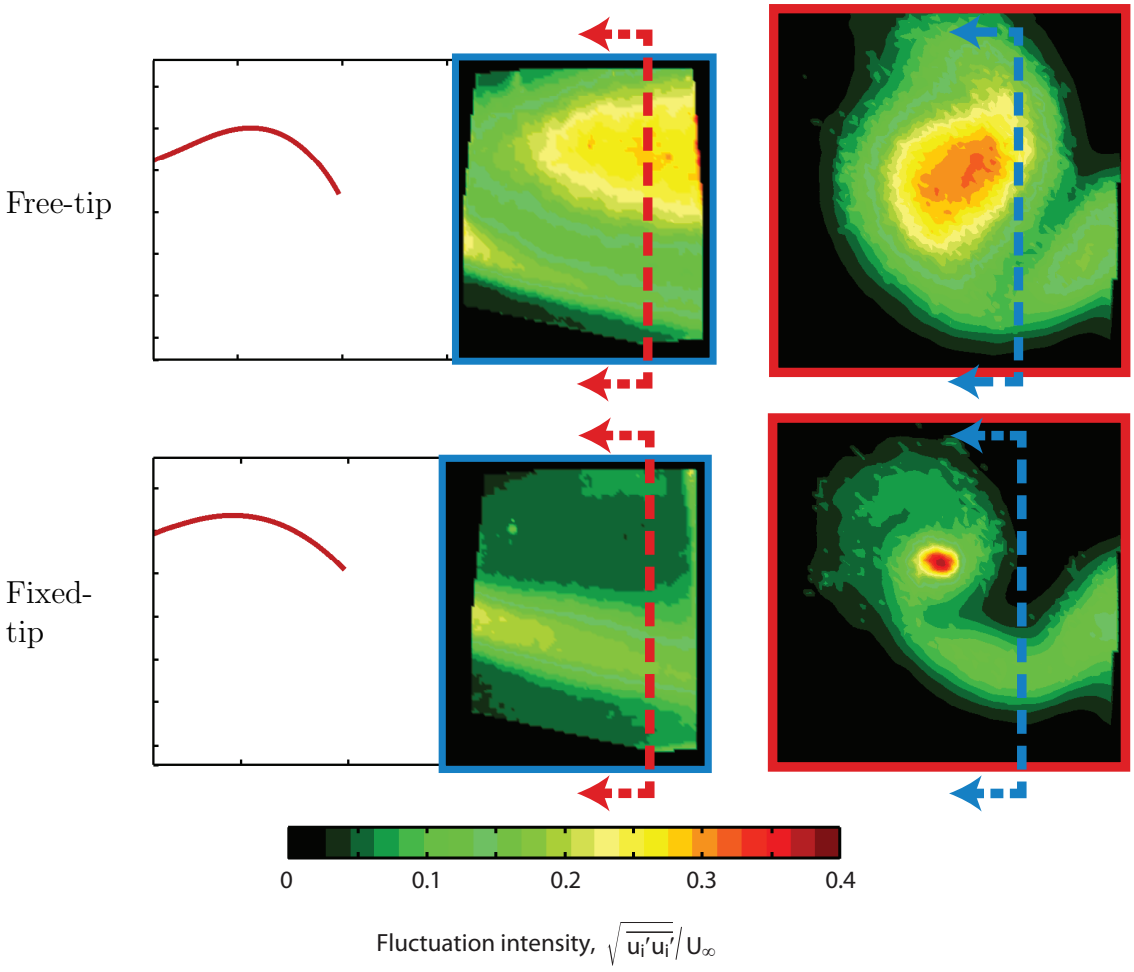

Figure 5.13: Streamwise and Trefftz plane views of the velocity fluctuation intensity in the wake behind the free- and fixed-tip wings at $\alpha = 10^\circ$ and $U_\infty = 12\,\mathrm{m/s}$. The mean membrane shapes measured at mid-half-span are plotted to scale, relative to the streamwise wake structures. The dashed section lines indicate the locations where the orthogonal view is located. The streamwise plane PIV and mid-half-span membrane kinematics data are originally from [113].

tip boundary support, as well as a rectangular flat plate with identical planform. At moderate angles of attack, the lift behavior of the flat plate agrees with the leading edge suction analogy originally formulated for delta wings, and the lift behavior of the membrane wings is consistent with previous experiments and simulations. At post-stall angles of attack, we found that the membrane wing with free wing tips exhibits monotonically decreasing lift with further increase in angle of attack, while the membrane wing with fully restrained wing tips was able to sustain increasing lift beyond the initial point of stall. We presented measurements of the membrane wing camber and dynamics at two spanwise locations. At the mid-wing measurement location on both membrane wings, the changes in wing camber reflect the changes in lift coefficient. However, the membrane wing with free wing tips showed increasing wing tip deflections with increasing angle of attack, even at post-stall conditions when the overall lift on the wing was decreasing. We found both membranes to exhibit standing and traveling mode vibrations, and both membranes show increased levels of broadband vibrations near the trailing edges, suggesting that both wings experience separated flow at the trailing edge. We also found that the free-tip wing experiences high overall levels of broadband membrane vibration, especially near the wing tip. Overall, the free-membrane wing tip exhibits exaggerated camber and greater amounts of noise vibration than the mid-span location.

The Trefftz plane PIV measurements reveal the tip vortex structures of the membrane wings exhibit drastically different behavior depending on the wing tip boundary condition. The tip vortex behind a free membrane wing tip shows larger core size, greater vortex meander, lower peak vorticity, and much higher unsteadiness compared to the tip vortex from a fixed-membrane wing tip. Correcting for vortex meander had negligible effect on the velocity unsteadiness in the wake of the free-tip membrane wing, suggesting that the exaggerated camber and highly dynamic motion of the free wing tip cause high levels of turbulence in the wake. The diffuse and unsteady tip

vortex structure, and the monotonic decline in lift coefficient with angle of attack beyond the initial stall suggests that the free-tip membrane wing is unable to benefit from vortex lift. In contrast, we found that the well-behaved fixed-tip membrane wing produced strong tip vortices with little unsteadiness, which allows the fixed-tip wing to generate higher lift at higher angles of attack than the free-tip wing. The PIV measurements demonstrate that the previously observed wake unsteadiness in the streamwise plane at mid-half-span is due to the extensive influence of the the tip vortex emanating from the free-membrane wing tip.

Low aspect ratio wings offer a key advantage in low Reynolds number flight applications with their ability to operate at large angles of attack while maintaining lift, facilitated by the influence of the tip vortices, which generate suction lift and suppress separation [2, 37, 38, 118]. Membrane wings offer the advantages of passive wing compliance, which allows wings to self-camber and to generate high values of lift as well as to interact dynamically with the shear layer [27, 30–32, 36, 113]. Yet, here it seems that aspect ratio and compliance are two features that may compete against one another: the compliance of the free-tip wing results in a highly cambered (Fig. 5.5) and highly dynamic wing tip (Fig. 5.6) that disrupts the size and structure of the tip vortex (Figs. 5.8, 5.10, and 5.12), which leads to a decrease in the lift performance (Fig. 5.4) at higher angles of attack. The reduction of lift performance with added compliance is contrary to the general notion that compliance should enhance lift [27, 30, 32, 36, 113]. Instead, because the compliance of the free tip wing is added at the critical location where the tip vortex forms, the potential benefit of vortex lift is lost. This study shows how the wing's compliance is an important factor in determining the wing's aerodynamic performance.

These results have implications for the design of low aspect ratio membrane wing MAVs. While the extra compliance of a free wing tip membrane may provide additional lift capability at low angles of attack, when operating at high angles of attack,

a free-tip membrane wing is more prone to the dangers of stall—especially in gusty conditions where a sudden change in wind direction could lead to loss of lift. Conversely, the unsteadiness of the free wing tip disrupts the coherence of the tip vortex and the organization of the wake, which may suppress the development of highly unsteady wing vibrations. It is interesting to note that bat wings exhibit wing tip support from the elongated, swept third digit. Because bats flap their wings, the angle of attack of the outer wing can reach $\alpha = 50^\circ$ [119]; hence, having a "fixed wing tip" may allow more favorable tip vortex formation and allow bats to benefit from vortex lift. However, it is unclear how the free trailing edge geometry of the bat wing may or may not be susceptible to highly unsteady force resonances.

This work was supported by the Air Force Office of Scientific Research.

CHAPTER 6. Conclusions

As technological advances have recently made the manufacture of small autonomous fliers tractable and thus created interest in Micro Air Vehicle applications, so have they created the necessity for understanding the principles of the low Reynolds number flight regime in which these MAVs operate. The natural world has "designed" its own low Reynolds number fliers through millions of years of evolution; thus, inspiration can be derived from the study of animal flight. Bats, which are the only flying mammals, employ a unique approach to low Reynolds number flight, with wings composed of a highly articulated wing skeleton supporting a compliant membrane skin. However, there are many challenges associated with bat flight experiments. In this thesis, we addressed two problems inspired by bat flight. We developed experimental techniques for accurate wind tunnel measurements of aerodynamic force production and energy expenditure in free-flying bats. Also, we performed theoretical, numerical, and experimental studies on rectangular membrane wings, in particular to investigate the effects of wing compliance and the importance of the membrane support geometry.

Previous wind tunnel investigations have utilized Trefftz plane PIV experiments to study bat flight, but they have struggled to obtain quantitative agreement between the measured strength of the vortex structures and the strengths expected due to animal weight support [11, 12, 15]. We determined that the origin of the measurement error

was insufficient dynamic range available in typical PIV measurement systems and developed a dual-plane PIV technique that increases the dynamic range of Trefftz plane measurements and allows accurate measurements of the vortex wakes behind free-fliers. We demonstrated the technique by accurately measuring the lift of free-flying bats in a wind tunnel. Furthermore, we used the dual-plane PIV measurements and the Helmholtz-Hodge decomposition to perform the first direct PIV measurement of the aerodynamic power of free-flying animals. Advances in PIV equipment will lead to further improvements in the resolution and accuracy of Trefftz plane measurements, and the emergence of high-speed tomographic systems will allow all three components of the vorticity vector to be resolved. At this time, the Taylor hypothesis remains a major assumption required in the calculation of extensive properties from Trefftz plane wake measurements; however, a recent study shows that wake vortex structures may exhibit significant deformation as they advect [17]. Because the mathematical formulas relate the instantaneous vortex configuration to the appropriate quantity (e.g., impulse or energy) [4], quantities derived from a time-series of measurements will be in error when the wake is distorting. More work is needed to fully understand this source of error when the Taylor hypothesis is a poor approximation.

Membrane wings are an attractive option for MAV design because they are lightweight and offer the potential for passive control; however, because their shape and aerodynamic response are strongly coupled, designing a wing is challenging. We developed a theoretical model that makes a priori predictions of membrane wing aerodynamic performance without the need for expensive computer simulations. However, because our theory relies on two dimensional potential flow theory and assumes a single degree of freedom deformation, it is unable to account for some of the interesting phenomena observed in our membrane wing experiments, such as resonant coupling of the membrane with the flow, and the dependance of the aerodynamic forces and wing tip vortex on the membrane support at the wing tip. These phenomena could play an

important role in the success of membrane wing designs, so it is necessary to improve upon the current membrane wing theory. We still need a better understanding of the mechanism that determines the formation of unsteady flow structures and membrane dynamics. PIV measurements and CFD studies will help elucidate the nature of the unsteady membrane wing interactions with the flow; however, each approach offers its own set of challenges. Emerging kilohertz PIV systems provide the temporal resolution to resolve the development and advection of flow structures over the wing [32, 36]; however, measuring the flow near the membrane surface is challenging because of the dynamic motion of the surface. High-fidelity CFD calculations provide the ability to examine the flow near the membrane; however, these coupled fluid-structure calculations currently remain prohibitively expensive for more than a few test cases. Experimental studies have already begun on membrane wings with free trailing edges [31, 36], which is a better approximation to bat wings, and a simple theoretical model for free-trailing-edge wings must address the inherent spanwise variations.

APPENDIX A. Comment on Vortex Impulse Measurement

With the advent of high-speed PIV lasers, it is now common in wind tunnel animal flight studies to measure the wake by periodically sampling at a fixed station downstream of the animal and to "stack" subsequent measurements, spaced by the freestream speed and the measurement period, to obtain a pseudo-volumetric reconstruction of the wake [e.g., 6–17]. These studies apply the fluid-dynamic principle that the hydrodynamic impulse in the wake is generated from the force production of the flier; therefore, one can infer information about the aerodynamic forces by studying the wake structure.

A potential problem with this method is that different parts of the wake in the volumetric reconstruction are measured at different instances in time from a flow that is possibly unsteady and evolving in time, but the mathematical formulas from vortex dynamics relate the hydrodynamic impulse to the instantaneous configuration of the vorticity (see Eqn. A3). The general approach in the literature is to assert that the strength of the vortex structures in the wake is small relative to the freestream velocity and therefore to assume that the wake structures advect passively through the measurement region.

In a recent paper, Bomphrey, Henningsson, Michaelis, and Hollis [17] (BHMH)

presented tomographic particle image velocimetry (PIV) measurements of the near wake of a tethered locust in a wind tunnel. They measured three components of velocity in the transverse plane, and the measurements were performed at sufficiently high frequency such that the thick slices of velocity vectors overlapped between consecutive measurements. With this volumetric data, they reconstructed a phase-averaged volumetric representation of the wake generated during a complete wingbeat cycle. BHMH visualized the wake by plotting the iso-surfaces of the Q-criterion and determined that the wake structure was undergoing deformation from observation of the imperfect vertical alignment of iso-surfaces between successive measurement samples. This misalignment of the vortex filaments suggests that the wake structures were descending as they advected downstream. The deformation of the wake structures during the measurement can lead to errors in the impulse calculations, which in turn lead to errors in both the lift and the thrust estimates derived from these measurements.

A.1 Simple Wake Distortion Model

We seek a model for estimating the magnitude of wake deformation behind a flier. The vertical descent of the wake observed by BHMH is similar to the steady descent of counter-rotating trailing vortices under their mutual induced velocity [71]; therefore, we construct a simple wake distortion model as a counter-rotating vortex pair whose strength and separation are given by simple aerodynamic models based on steady fixed-wing flight. Lift, L, of an elliptically loaded wing can be estimated as

$$L = \frac{\pi}{4}\rho U \Gamma b, \tag{A1}$$

where ρ is air density, Γ is circulation, b is wingspan, and U is flight speed. Because lift must balance weight, $W = mg = L$, the strength of the wake vortices will scale

inversely with flight speed: $\Gamma \propto W \cdot U^{-1}$. Following the analysis of Betz [5], who considered the evolution of vortex groups by applying the principles of conservation of impulse and conservation of moment of impulse, the spacing between the centroids of the tip vortices is $\Delta\overline{y} = \pi \cdot b/4$. The combination of these results yields the induced advection speed of one tip vortex due to the other, v_{wake}, which represents the rate of wake distortion and is estimated as

$$\frac{v_{\text{wake}}}{U} = \frac{8W}{\pi^3 \rho U^2 b^2} \ . \tag{A2}$$

This ratio of vertical descent velocity to the freestream velocity represents a vertical shear distortion of the wake. The vortex wake observed at some fixed distance behind a steady flier will appear to remain in a steady location, when in fact the wake is descending at a steady rate given by Eqn. A2. Thus, a pseudo-volumetric wake reconstruction based on stacking a time series of wake observations will yield a completely horizontal vortex system, when the actual vortex configuration is at an angle $\theta = \arctan\left(v_{\text{wake}}/U\right)$ from the horizontal.

We can estimate this mode of wake distortion for some sample fliers. Typical values of body weight $W = 177.0\,\text{mN}$ and wingspan $b = 28.5\,\text{cm}$ for the Seba's short-tailed bats (*Carollia perspicillata*) studied in Chapter 3 give induced velocities that are a small percentage of the forward flight speed above $4\,\text{m/s}$, $v_{\text{wake}}/U < 0.8\%$ (Fig. A1) and decrease as U^{-2}. This corresponds to a self-induced wake distortion angle $\theta < 0.5^\circ$. The same analysis for desert locust wakes [17] gives $v_{\text{wake}}/U \approx 0.8\%$ at a flight speed of $3.3\,\text{m/s}$ (i.e., $\theta \approx 0.5^\circ$).

For an animal flapping with a frequency f_{wb}, we can estimate the total wake displacement over a complete wingbeat cycle, Δy, as $v_{\text{wake}}/f_{\text{wb}}$. The typical wingbeat frequency for Seba's short-tailed bats is $f_{\text{wb}} \approx 9\,\text{Hz}$, and thus the estimated wake distortion is $\Delta y \approx 7\,\text{mm}$—2.5% of the wingspan. It thus seems reasonable to assume

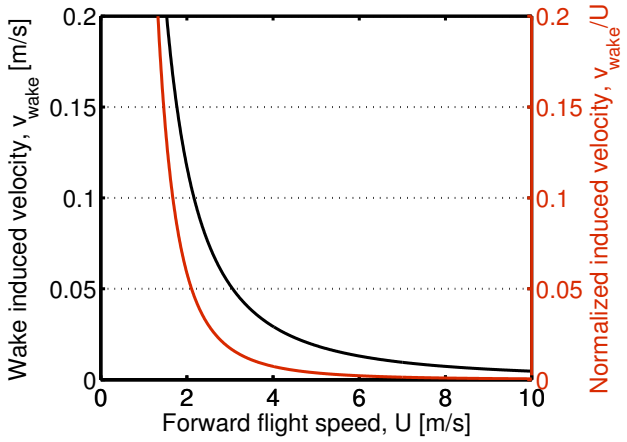

Figure A1: Predicted induced wake velocities for parameters typical of *Carollia perspicillata* ($W = 177.0\,\text{mN}$, $b = 28.5\,\text{cm}$). The black line gives dimensional values; the red line is normalized by flight speed. For flight velocities greater than 4 m/s, the induced velocities are less than 1% of the flight speed, enabling pseudo-volumetric reconstruction of three-dimensional wake structure from a stacked time series of planar realizations.

that the wake distortion is small compared to its overall structure and that this distortion is not a major source of error in the Chapter 3 analysis.

It is important to note that at slower flight speeds, the wake velocities induced by the vortex structures quickly increase as the wing circulation increases to maintain weight-support (Eqn. A1). Furthermore, the wakes behind flapping animals are significantly more complicated [6–17] than the simple two tip-vortex wake used in our model, because of both the flapping kinematics and the complex wing planforms. Our simple wake distortion model considers the relative magnitude of the wake's self-induced motion that originates from the momentum imparted into the wake by an idealized flier generating lift. The complex wakes behind real fliers result from more complicated lift distributions as well as from the production of thrust to counteract drag, and it is the temporal and spatial distribution of the production of these forces that result in the multi-vortex wake systems observed in the wake studies.

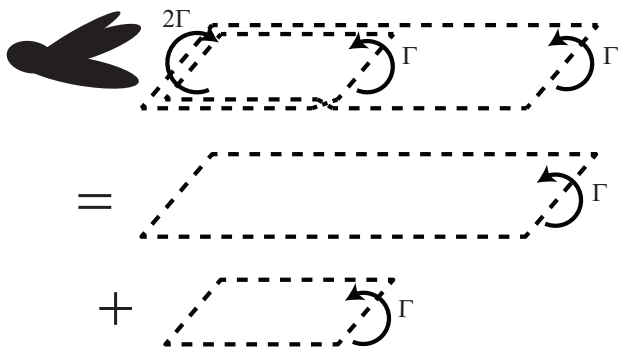

Figure A2: The wake of a flapping flier contains a complex network of vortex structures, in part because of time-varying force generation throughout the flapping cycle. In general, this complex vortex structure can be simplified as the superposition of simple vortex rings, amenable to simple analysis.

A.2 Example Wake Impulse Calculation

In general, the wake structure topology behind a flapping flier is more complex than a simple vortex ring [17]; however, more complex wakes generated by circulation that changes with time can be constructed using a superposition of nested vortex loops [4]. Fig. A2 depicts how a complex wake vortex system can be constructed from a single vortex line contour or as the sum of multiple vortex loops. The superposition of simple vortex loops can be repeated to fully reconstruct a complex vortex topology. Therefore, it is sufficient to consider a single vortex ring to study the effect of wake deformation on the estimation of vortex impulse.

BHMH use a thought experiment—a hypothetical isolated vortex loop—to explain the origin of wake deformation error. However, they present their argument graphically and without supporting mathematical arguments. Here, we present a simple argument based on the vortex configurations proposed by BHMH. We demonstrate that the error in the impulse caused by the mode of wake deformation described by BHMH is restricted solely to the thrust direction, while the lift estimate remains unchanged.

To explain the effect of wake deformation, BHMH introduce a simple wake that

deforms (see Figure 7 in Bomphrey et al. [17]). The example wake is a single vortex ring that advects downstream at the freestream velocity and whose self-induced downwash causes it to descend vertically. BHMH illustrate the wake structure as it would be reconstructed by periodically sampling the wake with tomographic PIV (BHMH Figure 7c), by instantaneously sampling the entire wake (BHMH Figure 7d), by periodically sampling the wake with planar stereo PIV (BHMH Figure 7e), and by correcting the tomographic PIV measurement by vertically aligning the vortex structures from adjacent measurements (BHMH Figure 7f).

To rigorously quantify the error in the impulse derived from an experimentally sampled wake, we consider the model problem of an isolated vortex loop in an unbounded fluid and calculate the impulse of the system in its exact configuration and in its hypothetically observed configuration. Without loss of generality, we first consider a flat rectangular vortex loop—analogous to BHMH Figure 7d—which has a span b, a streamwise extent a, and a circulation strength Γ. Fig. A3 shows the vortex configuration with a conveniently located coordinate basis $\mathbf{e}_i$. Here, the sense of circulation is chosen such that the vertical impulse of the fluid is negative, as would be the case in a wake of a weight-supporting flier. As with the scenario proposed by BHMH, our hypothetical vortex loop advects downward, inducing an apparent vertical shear θ as it is sampled along its extent (Fig. A4). The distorted vortex system still has a length a but now has a vertical extent c. A new coordinate basis $\mathbf{e'}_i$, rotated by θ about the span, is introduced for convenience. In this alternate basis, the sheared configuration appears identical to the original configuration, except that the length of the vortex ring is now $a' = \sqrt{a^2 + c^2}$.

We now consider the impulse generated by both the original and the distorted vortices. The impulse $\mathbf{I}$ of an isolated vortex system contained in the volume $\mathcal{V}$ is given by Saffman [4],

$$\mathbf{I} = \frac{1}{2}\rho \int_{\mathcal{V}} \mathbf{x} \times \omega \, \mathrm{d}V. \tag{A3}$$

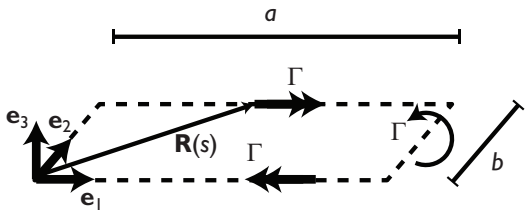

Figure A3: A hypothetical wake vortex with a purely vertical impulse. The vortex loop has strength Γ and is parameterized by the curve $\mathbf{R}(s)$. The vortex loop lies in the $(\mathbf{e}_1, \mathbf{e}_2)$ plane and has a horizontal extent a and a span b.

Here, ω is the vorticity and ρ is the fluid density. When the distribution of vorticity is singular, as is the case for an ideal line vortex, the vorticity takes the form $\omega = \Gamma\delta(\mathbf{x}-\mathbf{R}(s))\mathbf{t}$, where the strength of the vortex is Γ, the contour of the vortex ring is parameterized by s and is defined by $\mathbf{R}(s)$, and the unit tangent along that contour is $\mathbf{t}$. The equation for the impulse (equation A3) reduces to a contour integral,

$$\mathbf{I} = \frac{1}{2}\rho\Gamma \oint \mathbf{R}(s) \times \mathbf{t}\, \mathrm{d}s. \tag{A4}$$

For the rectangular vortex loop depicted in Fig. A3, the impulse is easily calculated by summing the contributions from each segment of the contour:

$$\begin{aligned}
\mathbf{I} = &\frac{1}{2}\rho\Gamma \int_0^a x_1\mathbf{e}_1 \times \mathbf{e}_1\, \mathrm{d}x_1 \\
&+ \frac{1}{2}\rho\Gamma \int_0^b (a\mathbf{e}_1 + x_2\mathbf{e}_2) \times -\mathbf{e}_2\, \mathrm{d}x_2 \\
&+ \frac{1}{2}\rho\Gamma \int_0^a (x_1\mathbf{e}_1 + b\mathbf{e}_2) \times \mathbf{e}_1\, \mathrm{d}x_1 \\
&+ \frac{1}{2}\rho\Gamma \int_0^b x_2\mathbf{e}_2 \times \mathbf{e}_2\, \mathrm{d}x_2.
\end{aligned} \tag{A5}$$

The first and last integrals in Eqn. A5 contribute zero impulse, while the second and third integrals in Eqn. A5 each contribute equally for a total impulse of $-\rho\Gamma ab\,\mathbf{e}_3$. This result is exactly the area enclosed by the vortex loop times the vortex strength,

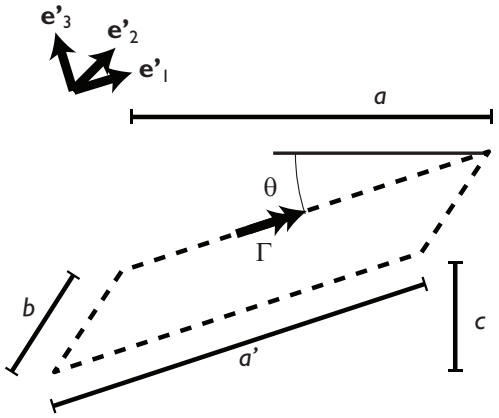

Figure A4: The vortex as it would be reconstructed in a "stacked" sequence of PIV measurements. The vortex loop still has a horizontal extent a and a span b, but because of the downward self-advection of the vortices there is a shear angle θ, and the vortex loop how has a height c in $\mathbf{e}_3$. We introduce a new basis $\mathbf{e}'_i$ such that the vortex loop lies in the $(\mathbf{e}'_1, \mathbf{e}'_2)$ plane. In this new basis the vortex loop appears identical to the vortex in Fig. A3, except with an extent of a'.

and it points in the direction of the area-normal given by the right-hand-rule of the circulation. Saffman gives an equivalent formula for the impulse of a line vortex based on integrating the surface bound by a vortex loop [4]:

$$\mathbf{I} = \rho\Gamma \int \mathrm{d}\mathbf{S}. \tag{A6}$$

We repeat this approach to calculate the impulse of the deformed vortex shown in Fig. A4, yielding

$$\mathbf{I} = -\rho\Gamma a' b\, \mathbf{e}'_3, \tag{A7}$$

$$= \rho\Gamma b(c\, \mathbf{e}_1 - a\, \mathbf{e}_3). \tag{A8}$$

Note that the vertical impulse of the two vortex loops is identical. However, a horizontal impulse, which was zero for a flat vortex loop, has been introduced because of the vertical shear deformation of the vortex structure. The magnitude of this error is given by $|\mathbf{I}_1| = |\mathbf{I}_3|(c/a) = |\mathbf{I}_3| \tan\theta$.

The results of this analysis have important implications for force calculations from wake measurements. Only the horizontal extent of the wake is relevant for calculating the vertical impulse, whereas only the vertical extent of the wake is relevant for calculating the horizontal impulse. The downwash behind a flier distorts the wake by causing the wake to descend vertically; however, it does not affect the horizontal extent of the wake, and BHMH mistakenly argue that the distortion of the wake by vertical shear leads to an error in the estimation of vertical impulse. They remain correct in stating that the apparent inclination of the wake does lead to an error in the horizontal impulse estimation.

Using their alignment technique, BHMH calculate that the angle of the primary vortex structures in the wake changes from 32° to 20°, and they conclude that the lift and thrust forces are 111% and 65% of their true values. These estimates appear to be derived from $\cos(20)/\cos(32) = 1.11$ and $\sin(20)/\sin(32) = 0.65$. Based on our analysis, we propose that the lift force remains unchanged, while the thrust force should be corrected by a factor of $\tan(20)/\tan(32) = 0.58$.

Another comment is warranted regarding the differences between tomographic and "standard" stereo planar PIV. Both techniques are capable of capturing the horizontal extent of the wake and the total vortex strength, and both measurements will thus predict the *same* vertical impulse (to within measurement uncertainty); consequently, traditional and tomographic PIV are equally capable of measuring the lift generated by the flier. The difference, however, between tomographic and traditional PIV techniques is the ability to determine the horizontal component of impulse. BHMH utilize the overlapping volumetric measurements to align vortex structures in adjacent measurement volumes. The resulting wake provides a superior approximation of the actual instantaneous wake configuration; therefore, it will produce a more accurate assessment of the horizontal component of impulse. This is an improvement over traditional PIV, which is unable to discern the orientation of the vortex filament.

A.3 Final Remarks

We have developed a simple model for estimating the magnitude of wake distortion of a flier based on the strength and spacing of a trailing vortex pair behind an elliptically loaded wing. Using typical flight parameters for Seba's short-tailed bats and desert locusts, the predicted wake distortion velocities are less than 1%. We also examined a model wake vortex problem outlined in BHMH to calculate the wake impulse error caused by the vertical shear distortion mode observed by BHMH. We determined that this type of wake distortion leads to errors in observed thrust but does not affect the lift estimate.

Tomographic PIV permits the direct measurement of the orientation of vortex filaments; therefore, wake distortion can be detected within a pseudo-volumetric reconstruction. However, by assuming that successive tomo-volumes can be spaced by the freestream velocity, the ability to fully correct for wake distortion is lost because the details of the streamwise wake velocity are neglected. Correcting the wake distortion between successive tomo-volumes requires that the vortex lines are aligned *and* that corresponding material points are coincident.

How significantly the errors from wake distortion affect aerodynamic force estimates from Trefftz plane PIV measurements remains unclear. To better quantify the wake distortion and its error, an experiment utilizing simultaneous PIV measurements at two different downstream stations behind the flier could be performed. This would allow for the direct comparison of the wake structure and inferred aerodynamic force history at each of the measurement stations.

APPENDIX B. Helmholtz-Hodge Decomposition

B.1 Background

The Helmholtz-Hodge decomposition is a result from classical mathematics, originally due to Helmholtz [86] and Hodge [120]. Helmholtz established that the motion of an unbounded fluid can be decomposed into dilation, rotation, and expansion [86]. Bhatia et al. [121] give a survey of the Helmholtz-Hodge decomposition and its applications. We summarize the key points here.

The Helmholtz-Hodge decomposition expresses a velocity field as the sum of an irrotational, a solenoidal, and a harmonic field. The decomposition's uniqueness guarantees that the flow is uniquely defined by its divergence and curl, up to a harmonic additive that is determined by boundary conditions.

Let $\mathbf{u}$ be the fluid velocity field, which we can express as an irrotational part $\mathbf{u}_\mathrm{e}$, a solenoidal part $\mathbf{u}_\mathrm{v}$, and a harmonic part $\mathbf{v}$:

$$\mathbf{u} = \mathbf{u}_\mathrm{e} + \mathbf{u}_\mathrm{v} + \mathbf{v} \tag{B1}$$

$$\nabla \times \mathbf{u}_\mathrm{e} = 0$$

$$\nabla \cdot \mathbf{u}_\mathrm{v} = 0$$

$$\nabla \times \mathbf{v} = \nabla \cdot \mathbf{v} = 0.$$

The divergence, Δ, and the vorticity, ω, can then be simply written as

$$\Delta = \nabla \cdot \mathbf{u} = \nabla \cdot \mathbf{u}_{\mathrm{e}}$$
$$\boldsymbol{\omega} = \nabla \times \mathbf{u} = \nabla \times \mathbf{u}_{\mathrm{v}}. \tag{B2}$$

Because $\mathbf{u}_{\mathrm{e}}$ is irrotational and $\mathbf{u}_{\mathrm{v}}$ is solenoidal, it is convenient to write them in terms of a scalar and vector potential, respectively:

$$\mathbf{u}_{\mathrm{e}} = \nabla \phi_{\mathrm{e}}, \tag{B3}$$
$$\mathbf{u}_{\mathrm{v}} = \nabla \times \mathbf{B}_{\mathrm{v}}. \tag{B4}$$

B.2 Application to Low Speed Wind Tunnel Measurements

In the case of an incompressible fluid, $\Delta = 0$, which is a valid assumption for low Mach number aerodynamic flows, the velocity due to dilation is zero, $\mathbf{u}_{\mathrm{e}} = 0$. Therefore, after dropping the dilational velocity field and substituting the vector potential definition for the rotational flow (Eqn. B4), the velocity field decomposition (Eqn. B1) becomes

$$\mathbf{u} = \nabla \times \mathbf{B}_{\mathrm{v}} + \mathbf{v}. \tag{B5}$$

We can derive a relationship between the vorticity and the vector potential by taking the curl of the incompressible Helmholtz-Hodge decomposition (Eqn. B5). The harmonic field, $\mathbf{v}$ is irrotational and thus disappears. Applying the vector identity

$$\nabla \times \nabla \times \mathbf{B}_{\mathrm{v}} = \nabla \left(\nabla \cdot \mathbf{B}_{\mathrm{v}} \right) - \nabla^2 \mathbf{B}_{\mathrm{v}}, \tag{B6}$$

and letting $\mathbf{B}_{\mathrm{v}}$ be divergence free, we arrive at a Poisson equation for the vector potential:

$$-\boldsymbol{\omega} = \nabla^2 \mathbf{B}_{\mathrm{v}}. \tag{B7}$$

B.3 Evaluation

The vorticity field is compact and is computed from the measured PIV data. For PIV data assembled by stacking successive Trefftz plane measurements, the out-of-plane vorticity components can be estimated by invoking Taylor's hypothesis. Using this data, we can integrate the Poisson equation (Eqn. B7) to find the vector potential, $\mathbf{B}_{\mathrm{v}}$, and thereby evaluate the velocity field throughout the wind tunnel test section. The boundary conditions enforce the fact that the test section has impermeable walls and can be satisfied with the method of images by mirroring the velocity field about the vertical and horizontal walls with infinite periodicity (Fig. B1). In the x-direction, we assume an infinitely long periodic train of wake structures. Because the wake structure behind a self-propelled object is essentially a vortex doublet with velocity decaying as $|\mathbf{x}|^{-2}$, the details of the slowly deforming wake downstream, or the truncation of the structures at the animal several body lengths upstream, have minimal effect on a single wingbeat domain. The image vorticity outside the wind tunnel domain will contribute a velocity field that is both irrotational and solenoidal inside the wind tunnel domain, thus defining $\mathbf{v}$ from Eqn. B5.

Because of the periodic boundary conditions in all directions, we can solve Eqn. B7 efficiently using a simple Fast Fourier Transform-based spectral method, and the velocity *anywhere in the wind tunnel* (Fig. B2) can thus be evaluated as

$$\mathbf{u} = \nabla \times \mathbf{B}_{\mathrm{v}}. \tag{B8}$$

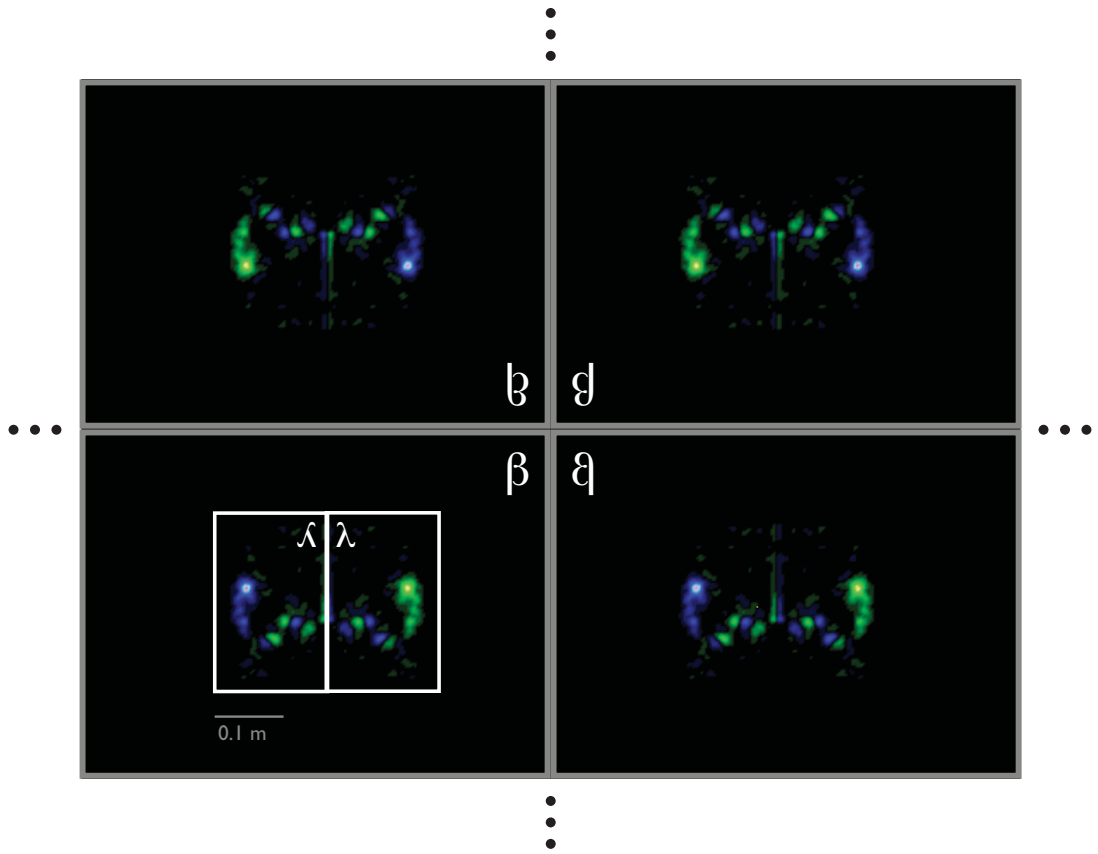

Figure B1: We show a slice of the computational domain used to solve the Poisson equation (Eqn. B7) for the vector potential, $\mathbf{B}_{\mathrm{v}}$. The PIV-measured vorticity field is the source term. The original half-span measurement region (denoted by λ) was reflected about the meridional plane of the bat. The boundary conditions for the wind tunnel walls are satisfied using the method of images by flipping and mirroring the wind tunnel test section domain (denoted by β) and applying infinte periodicity (denoted by the ellipses).

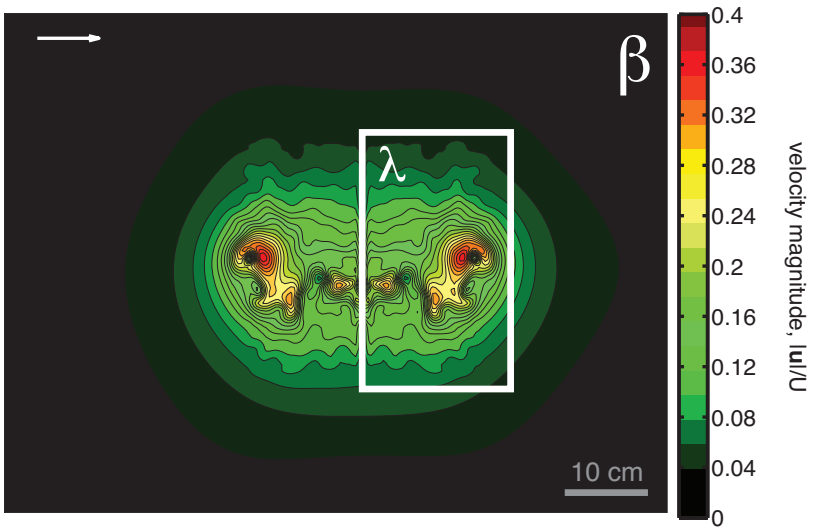

Figure B2: The velocity field throughout the wind tunnel test section (denoted by β) is evaluated using Eqn. B8. The white box denotes the original PIV measurement region (denoted by λ).

APPENDIX C. Defining Thin Wing Sections for Membrane Wing Aerodynamics Analysis in XFOIL

XFOIL requires that the membrane is defined as a two-dimensional cross section, given by a sequence of nodes representing a continuous surface. This aerodynamic model of the membrane has a thickness which, in practice, is larger than the typical membrane used in experiments ($h_{exp} \approx 0.1\%$ chord). For the analysis, a thickness of 1% chord was used. This thickness was chosen because it represents an aerodynamically thin cross section while also being sufficiently thick to minimize the numerical complications in XFOIL that accompany excessively thin geometries. The model also required aerodynamic leading and trailing edge geometry; the leading edge was rounded, and the trailing edge formed a cusp.

The membrane cross section was defined by its mean-line and thickness. The mean-line, $z(x)$, was represented by $N = 50$ grid points such that the chord-normal deflection and pressure load at x_{i} is z_{i} and p_{i}. The boundary conditions at the end of the membrane are $z_1 = z_{\mathrm{N}} = 0$. The thickness profile was constructed to produce a rounded leading edge, a sharp trailing edge, and a constant thickness between. The equations for defining the membrane thickness are

$$h(x) = \begin{cases} h_0 \cdot \left(1 - \left(\frac{x-4h_0}{4h_0}\right)^2\right)^{\frac{1}{4}}, & 0 \leqslant x < 4h_0, \\ h_0, & 4h_0 \leqslant x \leqslant (1-8h_0), \\ h_0 \cdot \left(1 - \left(\frac{x-(1-8h_0)}{8h_0}\right)\right)^{\frac{5}{2}}, & (1-8h_0) < x \leqslant 1. \end{cases} \tag{C1}$$

The aerodynamic model is then defined by a sequence of $2N-1$ nodes (X_j, Z_j), which start at the trailing edge, define around the leading edge, then terminate back at the trailing edge. These nodes are defined as

$$\begin{aligned} X_j &= \begin{cases} x_{N-j+1} + \frac{t(x_{N-j+1})}{2} \cdot n_x(x_{N-j+1}), & j = 1, 2, ...N, \\ x_{j-N+1} - \frac{t(x_{j-N+1})}{2} \cdot n_x(x_{j-N+1}), & j = N+1, N+2, ...2N-1. \end{cases} \\ Z_j &= \begin{cases} z_{N-j+1} + \frac{t(z_{N-j+1})}{2} \cdot n_z(x_{N-j+1}), & j = 1, 2, ...N, \\ z_{j-N+1} - \frac{t(z_{j-N+1})}{2} \cdot n_z(x_{j-N+1}), & j = N+1, N+2, ...2N-1. \end{cases} \end{aligned} \tag{C2}$$

where (n_x, n_z) is the unit normal to the membrane surface, given by,

$$n_x(x) = \frac{-z'(x)}{\sqrt{1 + (z'(x))^2}}, \qquad n_z(x) = \frac{1}{\sqrt{1 + (z'(x))^2}}. \tag{C3}$$

Here, the prime $'$ denotes differentiation with respect to x.

When membrane geometries exhibit large cambers, or when solutions at large angles of attack are sought, XFOIL may fail to find a solution to the viscous flow problem (especially in the Reynolds number regime of $Re \approx 10^5$–10^6). To aid in successful flow calculation, the flow was initially calculated over a flat plate at zero angle of incidence. The membrane and angle of attack were then interpolated between the flat configuration and the desired configuration using the interpolation scheme given in Eqn. C4. Here, $f \in [0, 1]$, with $f = 0$ corresponding to a flat membrane at zero

angle of incidence and $f = 1$ corresponding to the desired membrane configuration at angle of attack α. This scheme ensures that local membrane orientations change monotonically with f from the flat configuration to the desired configuration:

$$\begin{aligned} \alpha_f &= f \cdot \alpha \\ z_f(x) &= \frac{\tan\left(f \cdot \arctan\left(z'(0)\right)\right)}{z'(0)} \cdot z(x) \end{aligned} \tag{C4}$$

By starting with a configuration with a known solution and then gradually interpolating the problem into the desired configuration, each step is near a known solution, with the previous step's solution providing a good initial guess to XFOIL's Newton solution method [105].

To simplify the viscous calculations, transition to turbulence was forced at the leading edge. Because real membranes have sharp leading edges, flow usually separates at the leading edge, leading to transition; therefore, we believe this transition model is appropriate for the analysis.

APPENDIX D. Digitizing Two-dimensional Wing Profiles

Measuring the dynamics of a fluttering membrane wing requires a measurement technique with high temporal and spatial resolution. Several techniques have been employed to track the wing kinematics of engineering models and biological fliers, including marker tracking and digital image correlation [e.g., 9, 11, 24, 30, 34, 36, 85, 122, 123]. These techniques require multiple high-speed cameras and computational resources (Fig. D1). High-resolution surface reconstructions from marker tracking are laborsome and require large amounts of computational resources and time, which makes digitizing large data sets implausible.

When the kinematics are predominately two-dimensional, the experimental requirements are significantly simplified, and single-camera setups are sufficient. For two-dimensional membrane wings, the membrane shape is specified by a camber as a function of chord position. The membrane shape can easily be tracked by digitizing a line drawn along the chord. The spatial resolution of the measurement will scale with the camera resolution and depend on the accuracy of the algorithm. The temporal resolution will be limited only by the frame rate of the camera and available illumination. This idea of tracking the chord line has been employed in previous membrane wing studies where the line on the membrane is generated by a laser [32, 33] or is

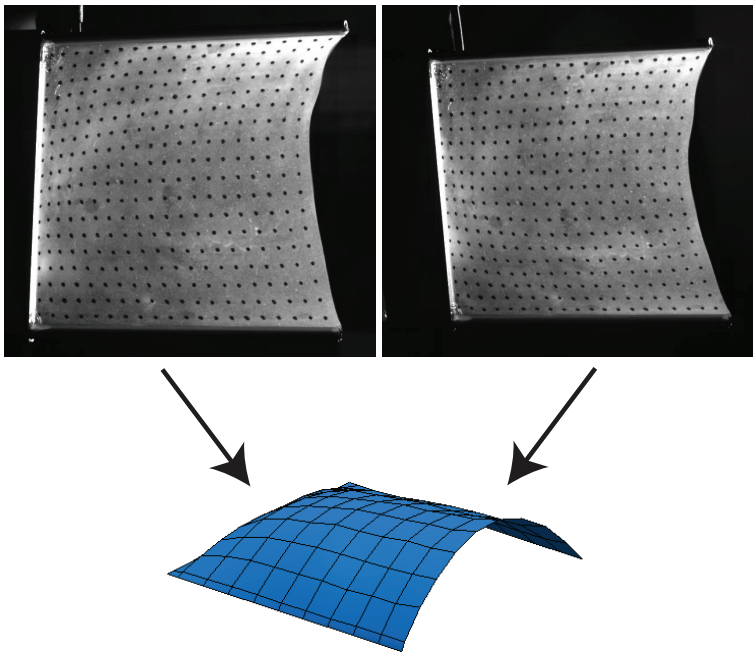

Figure D1: Calibrated stereo cameras can be used to track features in three-dimensional space. High resolution surface reconstructions are laborsome and require large amounts of computational resources and time.

painted on the membrane [35].

D.1 Experimental Configuration

The experimental configuration for measuring the two-dimensional surface profile of a membrane wing is illustrated in Fig. D2. A laser line approximately 1 mm thick is projected onto the membrane wing, generated by sheet-forming optics similar to those used in PIV experiments. A 500 mW, 650 nm wavelength diode laser provides sufficient illumination for fast camera frame rates (1500 Hz). A high-speed camera is positioned slightly above the measurement surface to avoid occlusion from the membrane flutter but to keep the camera axis as close to perpendicular as possible to the plane defined by the laser sheet. The camera lens aperture should be set to the highest possible f-number that still permits good laser line contrast at the target frame rate. The goal of the camera setup is to image only the laser line, with the rest

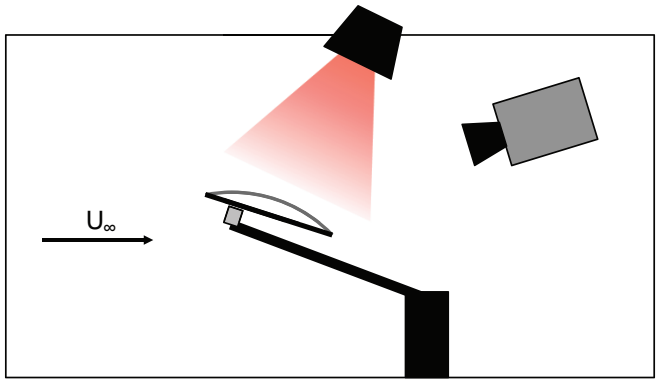

Figure D2: Experimental configuration for measuring the two-dimensional surface profile of a membrane wing.

of the image completely dark.

D.2 Calibration

The laser sheet defines the measurement plane and any information captured by the image sensor is assumed to lie in this plane. Two-dimensional direct linear transformation (DLT) parameters—which define a mapping between pixel locations on the image sensor to lab-space locations in the laser sheet plane [106]—are calculated with a calibration target placed in the laser sheet plane (Fig. D3).

D.3 Digitization

After the camera is calibrated, the wing kinematics are recorded in a high-speed video. The digitization process is illustrated in Fig. D4. To facilitate the automatic digitization of the membrane shapes, the leading and trailing edges of the membrane wing must be manually clicked once for each video as a preprocessing step. The manually clicked points are used to identify the target region in the video data for image processing, which is defined as a $c \times c$ square region *in the calibrated lab frame* centered on the wing (Fig. D4a). Here, c is the chord of the membrane wing and is calculated from the clicked leading and trailing edges.

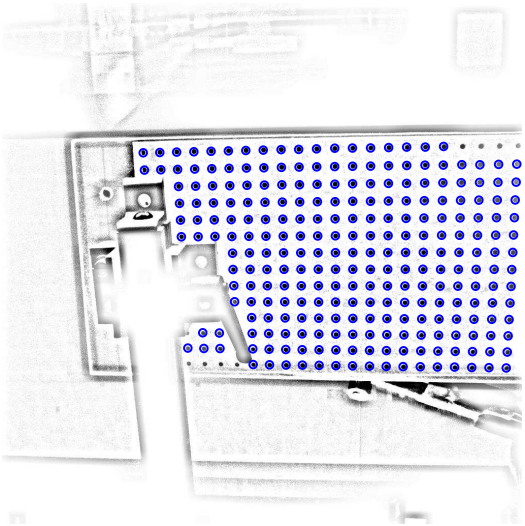

Figure D3: The camera is calibrated from an image of a calibration target aligned with the laser sheet. An automatic grid-detection code identifies all the target markers from four manually clicked seed points.

The automatic digitizer uses the DLT parameters to dewarp the target region into a wing-centric coordinate frame (Fig. D4b). Each column of pixels (e.g., the dashed green box in Fig. D4b) is extracted as a pixel intensity profile, p, versus chord-normal height, z. Fig. D4c shows the pixel intensity profile from the column highlighted in Fig. D4b. The task now is to identify the location of the laser line from the pixel intensity profile. Assuming that the profile of the laser line is symmetric and taking the membrane height from the center of the laser line, the digitizer effectively calculates the cross-correlation coefficients of $p(z)$ with $p(-z)$, i.e., the convolution $p * p$ (Fig. D4d). The location of the maximum convolution coefficient corresponds to the location of center of the laser line and, therefore, the camber of the membrane. Three-point Gaussian curve fitting is used to identify the convolution peak with subpixel accuracy. Finally, the coordinates of the digitized points are transformed into the calibrated lab coordinate frame.

To facilitate fast digitizing times, the image dewarping, convolution, peak finding, and coordinate transformation algorithms were implemented for highly parallelized

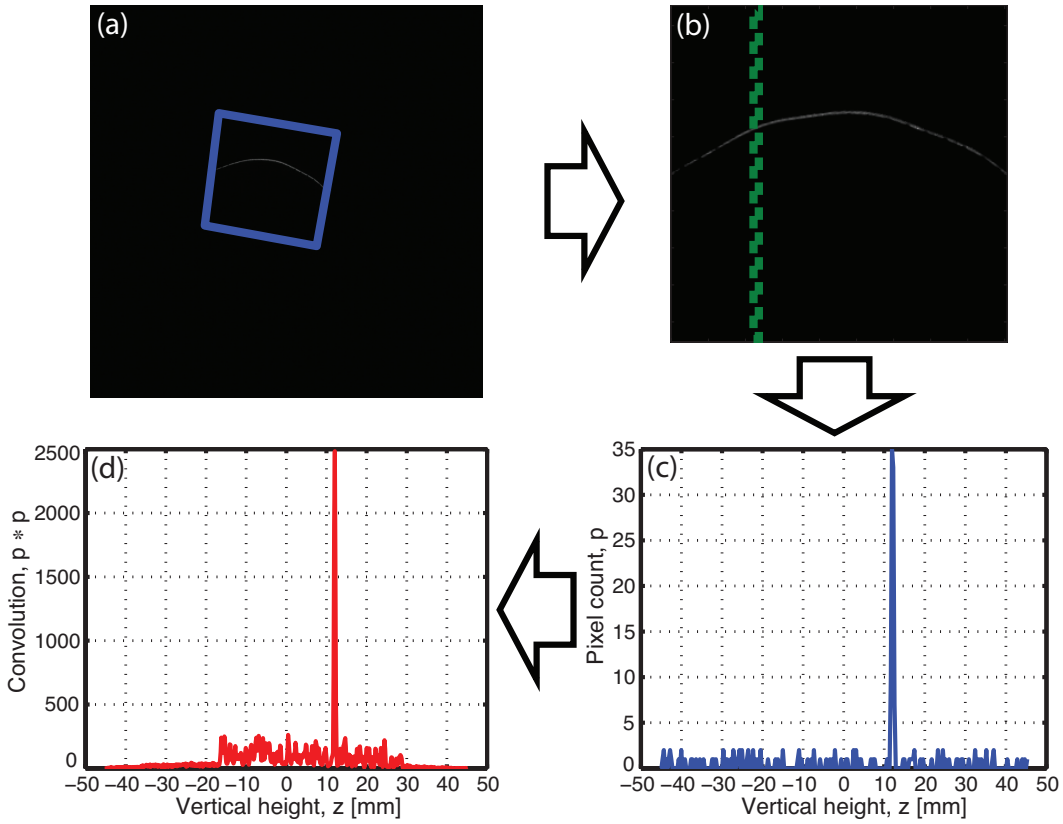

Figure D4: A pictoral representation of the digitizing process is shown. Starting in the upper left and proceeding in a clockwise direction, the steps are (a) identifying the target region in the image (denoted by the blue box), (b) dewarping the target region into a wing-centric coordinate frame where each column of pixels (denoted by the green box) represent the intensity as a function of chord-normal displacement, (c) extracting the pixel intensity map p at each chord-wise location, and (d) calculating the convolution of the pixel intensity map with itself, $p * p$, to identify the location of the laser line.

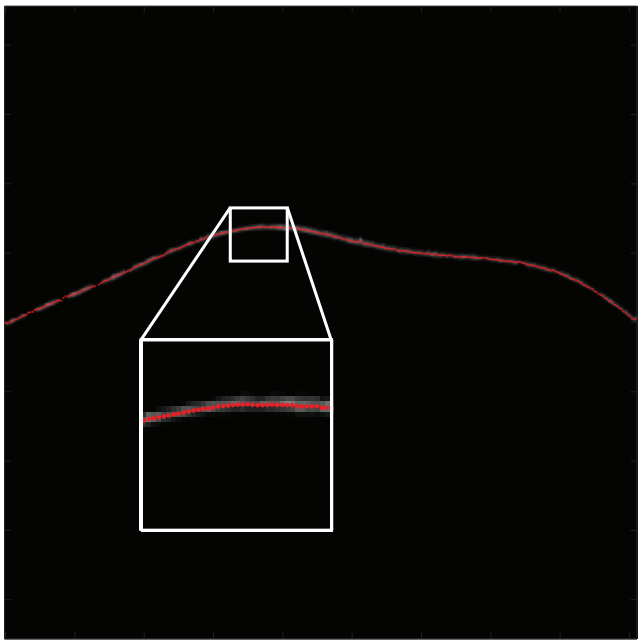

Figure D5: A wing camber value is calculated at each pixel along the chord.

calculation on a GPU using MATLAB's Parallel Processing Toolbox. A video with 3000 frames and approximately 300 pixels along the chord can be digitized in about 2 minutes. The result is a time sequence of membrane shapes. Fig. D5 shows a de-warped source image with the digitized membrane shape overlayed and demonstrates the density of the information that is extracted from a membrane measurement.

References

[1] W Shyy, M Berg, and D Ljungqvist. Flapping and flexible wings for biological and micro air vehicles. *Progress in Aerospace Sciences*, 35(5):455–505, 1999.

[2] T J. Mueller and J D. DeLaurier. Aerodynamics of small vehicles. *Annual Review of Fluid Mechanics*, 35:89–111, 2003.

[3] S M Swartz, M S Groves, H D Kim, and W R Walsh. Mechanical properties of bat wing membrane skin. *Journal of Zoology*, 239:357–378, 1996.

[4] P G Saffman. *Vortex Dynamics*. Cambridge University Press, 1992.

[5] A Betz. Behavior of vortex systems. *NACA-TM-713*, 1933.

[6] X Tian, J Iriarte-Diaz, K Middleton, R Galvao, E Israeli, A Roemer, A Sullivan, A Song, S M Swartz, and K S Breuer. Direct measurements of the kinematics and dynamics of bat flight. *Bioinspiration & Biomimetics*, 1: S10–S18, 2006.

[7] A Hedenström, L C Johansson, M Wolf, R von Busse, Y Winter, and G R Spedding. Bat flight generates complex aerodynamic tracks. *Science*, 316: 894–897, 2007.

[8] A Hedenström, F T Muijres, R von Busse, L C Johansson, Y Winter, and G R Spedding. High-speed stereo DPIV measurement of wakes of two bat species flying freely in a wind tunnel. *Experiments in Fluids*, 46:923–932, 2009.

[9] T Y Hubel, N I Hristov, S M Swartz, and K S Breuer. Time-resolved wake structure and kinematics of bat flight. *Experiments in Fluids*, 46:933–943, 2009.

[10] L C Johansson and A Hedenström. The vortex wake of blackcaps (*Sylvia atricapilla* L.) measured using high-speed digital particle image velocimetry (DPIV). *The Journal of Experimental Biology*, 212:3365–76, 2009.

[11] T Y Hubel, D K Riskin, S M Swartz, and K S Breuer. Wake structure and wing kinematics: the flight of the lesser dog-faced fruit bat, *Cynopterus brachyotis*. *The Journal of Experimental Biology*, 213:3427–3440, 2010.

[12] P Henningsson, F T Muijres, and A Hedenström. Time-resolved vortex wake of a common swift flying over a range of flight speeds. *Journal of the Royal Society Interface*, 8:807–816, 2010.

[13] P Henningsson and A Hedenström. Aerodynamics of gliding flight in common swifts. *The Journal of Experimental Biology*, 214:382–393, 2011.

[14] F T Muijres, M S Bowlin, L C Johansson, and A Hedenström. Vortex wake, downwash distribution, aerodynamic performance and wingbeat kinematics in slow-flying pied flycatchers. *Journal of the Royal Society Interface*, 9:292–303, 2011.

[15] T Y Hubel, N I Hristov, S M Swartz, and K S Breuer. Changes in kinematics and aerodynamics over a range of speeds in *Tadarida brasiliensis*, the Brazilian free-tailed bat. *Journal of the Royal Society Interface*, 9:1120–1130, 2012.

[16] L C Johansson, S Engel, E Baird, M Dacke, F T Muijres, and A Hedenström. Elytra boost lift, but reduce aerodynamic efficiency in flying beetles. *Journal of the Royal Society Interface*, 9(75):2745–2748, 2012.

[17] R J Bomphrey, P Henningsson, D Michaelis, and D Hollis. Tomographic particle image velocimetry of desert locust wakes: instantaneous volumes combine to reveal hidden vortex elements and rapid wake deformation. *Journal of The Royal Society Interface*, 9(77):3378–3386, 2012.

[18] C J Pennycuick. *Bird flight performance : A practical calculation manual*. Oxford University Press, 1989.

[19] J M V Rayner. A new approach to animal flight mechanics. *The Journal of Experimental Biology*, 80:17–54, 1979.

[20] G R Spedding, J M V Rayner, and C J Pennycuick. Momentum and energy in the wake of a pigeon (*Columba livia*) in slow flight. *The Journal of Experimental Biology*, 111:81–102, 1984.

[21] W Shyy, H Aono, S K Chimakurthi, P Trizila, C-K Kang, C E S Cesnik, and H Liu. Recent progress in flapping wing aerodynamics and aeroelasticity. *Progress in Aerospace Sciences*, 46(7):284–327, 2010.

[22] A C Carruthers, A L R Thomas, and G K Taylor. Automatic aeroelastic devices in the wings of a steppe eagle *Aquila nipalensis*. *Journal of Experimental Biology*, 210:4136–4149, 2007.

[23] S M Swartz and K M Middleton. Biomechanics of the bat limb skeleton: scaling, material properties and mechanics. *Cells, tissues, organs*, 187(1): 59–84, 2008.

[24] D K Riskin, D J Willis, J Iriarte-Díaz, T L Hedrick, M Kostandov, J Chen, D H Laidlaw, K S Breuer, and S M Swartz. Quantifying the complexity of bat wing kinematics. *Journal of Theoretical Biology*, 254(3):604–15, 2008.

[25] R Smith and W Shyy. Computation of aerodynamic coefficients for a flexible membrane airfoil in turbulent flow: a comparison with classical theory. *Physics of Fluids*, 8(12):3346–3353, 1996.

[26] B Stanford, P Ifju, R Albertani, and W Shyy. Fixed membrane wings for micro air vehicles: Experimental characterization, numerical modeling, and tailoring. *Progress in Aerospace Sciences*, 44(4):258–294, 2008.

[27] R E Gordnier. High fidelity computational simulation of a membrane wing airfoil. *Journal of Fluids and Structures*, 25(5):897–917, 2009.

[28] M Molki and K S Breuer. Oscillatory motions of a prestrained compliant membrane caused by fluidmembrane interaction. *Journal of Fluids and Structures*, 26(3):339–358, 2010.

[29] R E Gordnier and P J Attar. Aeroelastic simulations of an aspect ratio two flexible membrane wing. In *50th AIAA Aerospace Sciences Meeting*, Nashville, Tennessee, 2012.

[30] A Song, X Tian, E Israeli, R Galvao, K Bishop, S Swartz, and K Breuer. Aeromechanics of membrane wings with implications for animal flight. *AIAA Journal*, 46:2096–2106, 2008.

[31] H Hu, M Tamai, and J T Murphy. Flexible-membrane airfoils at low Reynolds numbers. *Journal of Aircraft*, 45(5):1767–1778, 2008.

[32] P Rojratsirikul, Z Wang, and I Gursul. Unsteady fluidstructure interactions of

membrane airfoils at low Reynolds numbers. *Experiments in Fluids*, 46(5): 859–872, 2009.

[33] P Rojratsirikul, Z Wang, and I Gursul. Effect of pre-strain and excess length on unsteady fluidstructure interactions of membrane airfoils. *Journal of Fluids and Structures*, 26(3):359–376, 2010.

[34] L Tregidgo, Z Wang, and I Gursul. Fluid-structure interactions for a low aspect-ratio membrane wing at low Reynolds numbers. In *41st AIAA Fluid Dynamics Conference and Exhibit*, Honolulu, Hawaii, 2011.

[35] S Arbós-Torrent, B Ganapathisubramani, and R Palacios. Leading- and trailing-edge effects on the aeromechanics of membrane aerofoils. *Journal of Fluids and Structures*, 38:107–126, 2013.

[36] A Timpe, Z Zhang, J Hubner, and L Ukeiley. Passive flow control by membrane wings for aerodynamic benefit. *Experiments in Fluids*, 54(3): 1471–1494, 2013.

[37] G E Torres and T J Mueller. Low aspect ratio aerodynamics at low reynolds numbers. *AIAA Journal*, 42(5):865–873, 2004.

[38] S M Kaplan, A Altman, and M Ol. Wake vorticity measurements for low aspect ratio wings at low Reynolds number. *Journal of Aircraft*, 44:241–251, 2007.

[39] E C Polhamus. A Concept of the Vortex Lift of Sharp-Edge Delta Wings Based on a Leading-Edge-Suction Analogy. Technical report, NASA, 1966.

[40] E V Laitone. Wind tunnel tests of wings at Reynolds numbers below 70,000. *Experiments in Fluids*, 23:405–409, 1997.

[41] S P Sane. The aerodynamics of insect flight. *Journal of Experimental Biology*, 206:4191–4208, 2003.

[42] U M Norberg. *Vertebrate Flight: Mechanics, Physiology, Morphology, Ecology and Evolution*. Springer-Verlag, Berlin, 1990.

[43] G R Spedding, A Hedenström, and M Rosén. Quantitative studies of the wakes of freely flying birds in a low-turbulence wind tunnel. *Experiments in Fluids*, 34:291–303, 2003.

[44] G R Spedding, M Rosén, and A Hedenström. A family of vortex wakes generated by a thrush nightingale in free flight in a wind tunnel over its entire natural range of flight speeds. *Journal of Experimental Biology*, 206: 2313–2344, 2003.

[45] W J Devenport and M C Rife. The structure and development of a wing-tip vortex. *Journal of Fluid Mechanics*, 312:67–106, 1996.

[46] P Gerontakos and T Lee. Near-field tip vortex behind a swept wing model. *Experiments in Fluids*, 40:141–155, 2005.

[47] C Karakus, H Akilli, and B Sahin. Formation, structure, and development of near-field wing tip vortices. *Proceedings of the Institution of Mechanical Engineers, Part G: Journal of Aerospace Engineering*, 222:13–22, 2008.

[48] D W Moore and P G Saffman. Axial flow in laminar trailing vortices. *Proceedings of the Royal Society A: Mathematical, Physical and Engineering Sciences*, 333:491–508, 1973.

[49] C D Donaldson, R S Snedeker, and R D Sullivan. Calculation of aircraft wake velocity profiles and comparison with experimental measurements. *Journal of Aircraft*, 11:547–555, 1974.

[50] P K Kundu and I M Cohen. *Fluid Mechanics*. Elsevier, New York, 3rd edition, 2004.

[51] T Gerz, F Holzapfel, and D Darracq. Commercial aircraft wake vortices. *Progress in Aerospace Sciences*, 38:181–208, 2002.

[52] W Shyy, Y Lian, J Tang, D Viieru, and H Liu. *Aerodynamics of Low Reynolds Number Flyers*. Cambridge University Press, 2008.

[53] R J Adrian. Dynamic ranges of velocity and spatial resolution of particle image velocimetry. *Measurement Science and Technology*, 8:1393–1398, 1997.

[54] M Raffel, C E Willert, S T Wereley, and J Kompenhans. *Particle Image Velocimetry*. Springer-Verlag, Berlin, 2001.

[55] C E Willert, M Raffel, J Kompenhans, B Stasicki, and C Kahler. Recent applications of particle image velocimetry in aerodynamic research. *Flow Measurement and Instrumentation*, 7:247–256, 1996.

[56] I Grant. Particle image velocimetry: a review. *Proceedings of the Institution of Mechanical Engineerings, Part C: Journal of Mechanical Engineering Science*, 211:55–76, 1997.

[57] M Gharib, M Raffel, O Ronneberger, and J Kompenhans. Feasibility study of three-dimensional PIV by correlating images of particles within parallel light sheet planes. *Experiments in Fluids*, 19:69–77, 1995.

[58] C C Landreth and R J Adrian. Electrooptical image shifting for particle image velocimetry. *Applied Optics*, 27:4216–4220, 1988.

[59] J Westerweel. Fundamentals of digital particle image velocimetry. *Measurement Science and Technology*, 8:1379–1392, 1997.

[60] N J Lawson and J Wu. Three-dimensional particle image velocimetry: error analysis of stereoscopic techniques. *Measurement Science and Technology*, 8: 894–900, 1997.

[61] C W H Doorne and J Westerweel. Measurement of laminar, transitional and turbulent pipe flow using stereoscopic-PIV. *Experiments in Fluids*, 42: 259–279, 2006.

[62] D Küchemann. A simple method for calculating the span and chordwise loading on straight and swept wings of any given aspect ratio at subsonic speeds, 1952.

[63] D Birch, T Lee, F Mokhtarian, and F Kafyeke. Structure and induced drag of a tip vortex. *Journal of Aircraft*, 41:1138–1145, 2004.

[64] J Westerweel. *Digital particle image velocimetry: theory and application*. PhD thesis, TU Delft, 1993.

[65] S Engel, M S Bowlin, and A Hendenström. The role of wind-tunnel studies in integrative research on migration biology. *Integrative and Comparative Biology*, 50(3):323–335, 2010.

[66] A Houston. The flight speed of parent birds feeding young. *Journal of Avian Biology*, 37(6):545–554, 2006.

[67] U Grodzinski, O Spiegel, C Korine, and M W Holderied. Context-dependent flight speed: evidence for energetically optimal flight speed in the bat *Pipistrellus kuhlii*? *Journal of Animal Ecology*, 78(3):540–548, 2009.

[68] A Hedenström. Aerodynamics, evolution and ecology of avian flight. *Trends in Ecology & Evolution*, 17(9):415–422, 2002.

[69] U M L Norberg and R A Norberg. Scaling of wingbeat frequency with body mass in bats and limits to maximum bat size. *Journal of Experimental Biology*, 215(5):711–722, 2012.

[70] F T Muijres, G R Spedding, Y Winter, and A Hedenström. Actuator disk model and span efficiency of flapping flight in bats based on time-resolved PIV measurements. *Experiments in Fluids*, 51(2):511–525, 2011.

[71] R M Waldman and K S Breuer. Accurate measurement of streamwise vortices using dual-plane PIV. *Experiments in Fluids*, 53(5):1487–1500, 2012.

[72] G R Spedding. The wake of a jackdaw (*Corvus monedula*) in slow flight. *The Journal of Experimental Biology*, 125:287–307, 1986.

[73] A Hedenström, M Rosén, and G R Spedding. Vortex wakes generated by robins *Erithacus rubecula* during free flight in a wind tunnel. *Journal of The Royal Society Interface*, 3(7):263–276, 2006.

[74] P Henningsson, F T Muijres, and A Hedenström. Time-resolved vortex wake of a common swift flying over a range of flight speeds. *Journal of The Royal Society Interface*, 8(59):807–816, 2011.

[75] L G Halsey. The challenge of measuring energy expenditure: Current field and laboratory methods. *Comparative Biochemistry and Physiology, Part A*, 158 (3):247–251, 2011.

[76] J J Videler. *Avian Flight*. Oxford University Press, Oxford, 2005.

[77] S P Thomas. Metabolism during flight in two species of bats, *Phyllostomus hastatus* and *Pteropus gouldii*. *The Journal of Experimental Biology*, 63(1): 273–293, 1975.

[78] U M Norberg, T H Kunz, J F Steffensen, Y Winter, and O von Helversen. The cost of hovering and forward flight in a nectar-feeding bat, *Glossophaga soricina*, estimated from aerodynamic theory. *The Journal of Experimental Biology*, 182:207–227, 1993.

[79] C C Voigt and Y Winter. Energetic cost of hovering flight in nectar-feeding bats (Phyllostomidae: Glossophaginae) and its scaling in moths, birds and bats. *Journal of Comparative Physiology A*, 169(1):38–48, 1999.

[80] S Ward, U Möller, J M V Rayner, D M Jackson, D Bilo, W Nachtigall, and J R Speakman. Metabolic power, mechanical power and efficiency during wind tunnel flight by the European starling *Sturnus vulgaris*. *The Journal of Experimental Biology*, 204:3311–3322, 2001.

[81] R von Busse, S M Swartz, and C C Voigt. Flight metabolism in relation to speed in Chiroptera: Testing the U-shape paradigm in the short-tailed fruit bat *Carollia perspicillata*. *Journal of Experimental Biology*, 11(216): 2073–2080, 2013.

[82] A Eckstein and P Vlachos. Assessment of advanced windowing techniques for digital particle image velocimetry (DPIV). *Measurement Science and Technology*, 20(7):075402, 2009.

[83] A J Bergou, S Swartz, K Breuer, and G Taubin. 3D reconstruction of bat flight kinematics from sparse multiple views. In *2011 IEEE International Conference on Computer Vision Workshops (ICCV Workshops)*, Barcelona, Spain, 2011.

[84] L C Johansson, M Wolf, R von Busse, Y Winter, G R Spedding, and A Hedenström. The near and far wake of Pallas' long tongued bat

(*Glossophaga soricina*). *The Journal of Experimental Biology*, 211(18): 2909–2918, 2008.

[85] M Wolf, L C Johansson, R von Busse, Y Winter, and A Hedenström. Kinematics of flight and the relationship to the vortex wake of a Pallas' long tongued bat (*Glossophaga soricina*). *Journal of Experimental Biology*, 213 (12):2142–2153, 2010.

[86] H Helmholtz. Über Integrale der hydrodynamischen Gleichungen, welche den Wirbelbewegungen entsprechen. *Journal für die reine und angewandte Mathematik (Crelles Journal)*, 55:25–55, 1858.

[87] C Hambly, E Harper, and J Speakman. Cost of flight in the zebra finch (*Taenopygia guttata*): a novel approach based on elimination of ^{13}C labelled bicarbonate. *J Comp Physiol B*, 172(6):529–539, 2002.

[88] G R Spedding and C J Pennycuick. Uncertainty calculations for theoretical flight power curves. *Journal of Theoretical Biology*, 208(2):127–139, 2001.

[89] C J Pennycuick. Fifteen testable predictions about bird flight. *Oikos*, 30: 165–176, 1978.

[90] A Hedenström and T Alerstam. Skylark optimal flight speeds for flying nowhere and somewhere. *Behavioral Ecology*, 7(2):121–126, 1996.

[91] C J Pennycuick, S Åkesson, and A Hedenström. Air speeds of migrating birds observed by ornithodolite and compared with predictions from flight theory. *Journal of The Royal Society Interface*, 10(86), 2013.

[92] V A Tucker. Metabolism during flight in the laughing gull, *Larus atricilla*. *The American Journal of Physiology*, 222(2):237–245, 1972.

[93] M H Bernstein, S P Thomas, and K Schmidt-Nielsen. Power input during flight of the fish crow, *Corvus ossifragus*. *The Journal of Experimental Biology*, 58:401–410, 1973.

[94] R Dudley and Y Winter. Hovering flight mechanics of neotropical flower bats (Phyllostomidae: Glossophaginae) in normodense and hypodense gas mixtures. *The Journal of Experimental Biology*, 205(23):3669–3677, 2002.

[95] J M V Rayner. Vertebrate flapping flight mechanics and aerodynamics, and the evolution of flight in bats. *Biona Report*, 5:27–74, 1986.

[96] B Thwaites. The aerodynamics theory of sails. I. Two-dimensional sails. *Proceedings of Royal Society A*, 261:402–422, 1961.

[97] J N Nielsen. Theory of flexible aerodynamic surfaces. *Trans. ASME: J. Appl. Mech*, 30:435–442, 1963.

[98] J Etienne, J Loheac, and P Saramito. A Lagrange-multiplier approach for the numerical simulation of an inextensible membrane or thread immersed in a fluid. *SIAM Journal on Scientific Computing*, pages 1–14, 2010.

[99] O Le Maître, S Huberson, and E S De Cursi. Unsteady model of sail and flow interaction. *Journal of Fluids and Structures*, 13:37–59, 1999.

[100] R M Waldman, A J Song, D K Riskin, S M Swartz, and K S Breuer. Aerodynamic behavior of compliant membranes as related to bat flight. In *38th AIAA Fluid Dynamics Conference and Exhibit*, Seattle, Washington, 2008.

[101] B Stanford and P Ifju. The validity range of low fidelity structural membrane models. *Experimental Mechanics*, 48(6):697–711, 2008.

[102] A F Bower. *Applied Mechanics of Solids*. CRC Press, 1st edition, 2010.

[103] P Rojratsirikul, M S Genc, Z Wang, and I Gursul. Flow-induced vibrations of low aspect ratio rectangular membrane wings. *Journal of Fluids and Structures*, 27(8):1296–1309, 2011.

[104] R E Gordnier. High fidelity computational simulation of a membrane wing airfoil. In *46th AIAA Aerospace Sciences Meeting and Exhibit*, Reno, Nevada, 2008.

[105] M Drela. XFOIL: An Analysis and Design System for Low Reynolds Number Airfoils. In T. J. Mueller, editor, *Low Reynolds Number Aerodynamics. Lecture Notes in Engineering, Vol 54.* Springer Verlag, 1989.

[106] R Hartley and A Zisserman. *Multiple View Geometry in Computer Vision*, volume 2. Cambridge University Press, 2000.

[107] L Sirovich. Turbulence and the dynamics of coherent structures. i-coherent structures. ii-symmetries and transformations. iii-dynamics and scaling. *Quarterly of applied mathematics*, 45:561–571, 1987.

[108] G Berkooz, P Holmes, and J L Lumley. The proper orthogonal decomposition in the analysis of turbulent flows. *Annual Review of Fluid Mechanics*, 25: 539–575, 1993.

[109] S L Brunton and C W Rowley. Modeling the unsteady aerodynamic forces on small-scale wings. In *47th AIAA Aerospace Sciences Meeting*, Orlando, Florida, 2009.

[110] Y Kim, D Rockwell, and A Liakopoulos. Vortex buffeting of aircraft tail: interpretation via proper orthogonal decomposition. *AIAA Journal*, 43(3): 550–559, 2005.

[111] L Graftieaux, M Michard, and N Grosjean. Combining PIV, POD and vortex identification algorithms for the study of unsteady turbulent swirling flows. *Measurement Science and Technology*, 12(9):1422–1429, 2001.

[112] P Seide. Large deflections of rectangular membranes under uniform pressure. *International Journal of Non-Linear Mechanics*, 12, 1977.

[113] R M Waldman and K S Breuer. Shape, lift, and vibrations of highly compliant membrane wings. In *43rd AIAA Fluid Dynamics Conference*, San Diego, California, 2013.

[114] O M Curet, A Carrere, R M Waldman, and K S Breuer. Aerodynamic Characterization of Wing Membrane with Adaptive Compliance. In *54th AIAA/ASME/ASCE/AHS/ASC Structures, Structural Dynamics, and Materials Conference*, Reston, Virginia, 2013.

[115] J E Lamar. Prediction of vortex flow characteristics of wings at subsonic and supersonic speeds. *Journal of Aircraft*, 13(7):490–494, 1976.

[116] M J Bhagwat and M Ramasamy. Effect of tip vortex aperiodicity on measurement uncertainty. *Experiments in Fluids*, 53(5):1191–1202, 2012.

[117] P Welch. The use of fast Fourier transform for the estimation of power spectra: a method based on time averaging over short, modified periodograms. *Audio and Electroacoustics, IEEE Transactions on*, AU-15(2):70–73, 1967.

[118] M J Sytsma and L S Ukeiley. Evaluating the flow fields around low aspect ratio flat plates in wind tunnel turbulence. In *31st AIAA Applied Aerodynamics Conference*, San Diego, California, 2013.

[119] R von Busse, A Hedenström, Y Winter, and L C Johansson. Kinematics and

wing shape across flight speed in the bat, *Leptonycteris yerbabuenae*. *Biology Open*, 1(12):1226–1238, 2012.

[120] W V D Hodge. *The Theory and Applications of Harmonic Integrals*. Cambridge University Press, Cambridge, 1952.

[121] H Bhatia, G Norgard, V Pascucci, and P-T Bremer. The Helmholtz-Hodge decomposition—a survey. *IEEE Transactions on Visualization and Computer Graphics*, 19(8):1386–1404, 2013.

[122] R Albertani, B Stanford, J P Hubner, and P G Ifju. Aerodynamic coefficients and deformation measurements on flexible micro air vehicle wings. *Experimental Mechanics*, 47(5):625–635, 2007.

[123] R von Busse, A Hedenström, Y Winter, and L C Johansson. Kinematics and wing shape across flight speed in the bat, *Leptonycteris yerbabuenae*. *Biology Open*, 1(12):1226–1238, 2012.